LIGHT MATTER INTERACTION IN PLEXCITONIC CRYSTALS AND MOIRÉ CAVITIES

A DISSERTATION SUBMITTED TO
THE GRADUATE SCHOOL OF ENGINEERING AND SCIENCE
OF BILKENT UNIVERSITY
IN PARTIAL FULFILLMENT OF THE REQUIREMENTS FOR
THE DEGREE OF
DOCTOR OF PHILOSOPHY
IN
PHYSICS

By
Ertuğrul Karademir
January, 2015

LIGHT MATTER INTERACTION IN PLEXCITONIC CRYSTALS AND MOIRÉ CAVITIES
By Ertuğrul Karademir
January, 2015

We certify that we have read this thesis and that in our opinion it is fully adequate, in scope and in quality, as a dissertation for the degree of Doctor of Philosophy.

Prof. Dr. Atilla Aydınlı(Advisor)

Prof. Dr. Ayhan Altıntaş

Prof. Dr. Raşit Turan

Assoc. Prof. Ceyhun Bulutay

Asst. Prof. Coşkun Kocabaş

Approved for the Graduate School of Engineering and Science:

Prof. Dr. Levent Onural
Director of the Graduate School

ABSTRACT

LIGHT MATTER INTERACTION IN PLEXCITONIC CRYSTALS AND MOIRÉ CAVITIES

Ertuğrul Karademir
Ph.D. in Physics
Advisor: Prof. Dr. Atilla Aydınlı
January, 2015

Surface plasmon polaritons (SPPs) are quanta of electromagnetic excitations at the interface between metal and dielectric media. SPPs with an evanescent tail in the perpendicular direction, thus their properties are sensitive to variations in the optical properties of the dielectrics film. If SPPs are created near excitonic media, coupling between excitons and SPs can be achieved. In this thesis, interaction dynamics of SPP-exciton coupling is investigated. In weak coupling case, properties of SPPs and excitons are perturbed as the enhancement of the optical absorption in excitonic matrices. In the strong coupling, coupled pairs (plexcitons) causes Rabi splitting in SPP dispersion curves. By patterning the metal−dielectric interface with sine profile grating, it is possible to form a band gap on the dispersion curve, width of which can be tuned by the groove depth and SPP-Exciton coupling can be engineered. Using this, a new type of crystal, plexcitonic crystal, is proposed and demonstrated that exhibit directional dependent coupling on square and triangular lattices. Superposing an additional grating on the initial one but with a slight difference in pitch, results in Moiré cavities, in which, slow plasmon modes can be confined. We show that we can directly image these modes using dark field microscopy. Further, the slow cavity mode in contact with an excitonic source, where SPPs are coupled with near field coupling, results in amplified light signal. Various Moiré cavities are shown to exhibit plasmonic lasing when slow plasmon modes in Ag coated cavities are excited inside a suitable gain medium.

Keywords: Surface Plasmon Polaritons, Excitons, Light Matter Interaction, Plexcitonic Crystals, Moiré Cavities, Plasmonic Lasers.

ÖZET

PLEKSİTONİK KRİSTALLER VE MOIRÉ KOVUKLARINDA IŞIK MADDE ETKİLEŞİMİ

Ertuğrul Karademir
Fizik, Doktora
Tez Danışmanı: Prof. Dr. Atilla Aydınlı
Ocak, 2015

Yüzey plasmon polaritonları (YPPler) metal ve dielektrik arayüzünde uyarılan elektromanyetik dalgaların nicemleridir. Arayüzde ilerleyen YPPlerin dik yönlerde haleleri bulunur, bu yüzden dielektrik ortamdaki optik özellik değişimlerine karşı hassastırlar. Eğer YPPler eksitonik bir ortamın yanında oluşturulurlarsa eksitonik kipler ve yüzey plasmonları (YPler) arasında çiftlenme oluşabilir. Bu tezde YPP-Eksiton çiftlenmesinin etkileşim dinamiği zayıf ve kuvvetli bölgelerde incelendi. Zayıf durumda, YPP ve eksitonların optik özellikleri sadece perturbe olurlar. Bu durum eksiton matrislerinin optik soğurmasını artırabilir. Fakat, kuvvetli çiftlenme durumunda, çiftlenmiş eşler (pleksitonlar) dispersiyon eğrisinde Rabi ayrılmasına sebep olurlar. Metal-dielektrik yüzeyi sinüs profilli bir desen ile desenlenerek, dispersiyon eğrisinde yasaklı bir bölge yani bant aralığı oluşturmak mümkündür. Bant aralığının genişliği desenin çizgi derinliği ile ayarlanabilir, böylece YPP-Eksiton etkileşiminin mühendisliği yapılabilir. Bu etkileşim YPP kiplerinin yeniden dağılımı çerçevesinde incelenir. Bu prensipten yola çıkarak, yön bağımlı YPP-Eksiton etkileşimine sahip yeni bir kristal, pleksitonik kristal öne sürülmüş, kare ve üçgen örgülerde gösterilmiştir. Önceki sinüs kırınım ağının üstüne periyodu çok az değiştirilmiş başka bir kırınım ağı eklendiğinde Moiré kovukları elde edilir. Bu kovuklarda yavaş ilerleyen YPP kipleri hapsolmuştur. Bu kipler karanlık alan mikroskopisi ile gözlemlenmiştir. Ayrıca Ag kaplı çeşitli Moiré kovuklarının yakınına uygun bir eksitonik kaynak yüklenerek metal yüzeyde ışık sinyalinin yükseltgenmiş ve yeni bir plazmonik lazer oluşturulmuştur.

Anahtar sözcükler: Yüzey Plazmon Polaritonları, Eksitonlar, Işık Madde Etkileşimi, Pleksitonik Kristaller, Moiré Kovukları, Plazmonik Lazerler.

Acknowledgement

This five line acknowledgement paragraph may not be enough to express my deepest gratitude for my academic mentor and colleague, Prof. Atilla Aydınlı, for his guidance, moral and academic input, and intellectual conversations on topics regarding mainly my research and many other aspects of life during both my Ph.D. and M.Sc. years.

I would like to express my gratitude also to Prof. Coşkun Kocabaş for his patience, collaboration, intellectual input, and also his coffee beans that helped me get through many late nights.

I would like to thank Prof. Sinan Balcı for his invaluable mentoring and collaboration at every stage of my Ph.D. research.

I would like to express my gratitude to Prof. Raşit Turan and Prof. Ceyhun Bulutay for their invaluable guidance via Thesis Committee Meetings.

I am also grateful to Prof. Ayhan Altıntaş, Prof. Raşit Turan, Prof. Ceyhun Bulutay, and Prof. Coşkun Kocabaş for their time and consideration on assessing the scientific quality of this thesis.

I would like to thank Simge Ateş for her assistance during early stages of my Ph.D. I hope to collaborate with her in the future.

I am thankful for their collaboration and technical equipment support to Prof. Mykhailo Ya. Valakh and Dr. Volodymyr Dzhagan of V.E. Lashkaryov Institute of Semiconductor Physics, National Academy of Sciences of Ukraine, and Prof. F. Ömer İlday, Dr. Hamit Kalaycıoğlu, Seydi Yavaş, and Önder Akçaalan of UFOLAB Bilkent.

I would like to thank Ergün Kahraman and Murat Güre for their efforts to maintain an excellent working environment at Advanced Research Laboratories in Bilkent. I would also like to thank Ergün Kahraman for his support in building many custom types of equipments for use in my experiments.

I would like to express my deepest gratitude to faculty members of Department of Physics of Bilkent University, namely Prof. Cemal Yalabık, Prof. Bilal Tanatar, Prof. Ceyhun Bulutay, Prof. Tuğrul Hakioğlu,, Prof. Atilla Erçelebi, Prof. Ekmel Özbay, Prof. Oğuz Gülseren, Prof. Coşkun Kocabaş Prof. Özgür Oktel, Prof.

Giovanni Volpe, Prof. Balazs Hetényi for their efforts to my education and for their exemplary stand on academic morals.

I would like to thank my friends Ayşe Yeşil, Fatma Nur Ünal, Yağmur Aksu, Başak Renklioğlu, Erçağ Pinçe, Melike Gümüş, Seval Sarıtaş, Abdullah Muti, Abdullah Kahraman, Emre Ozan Polat, Osman Balcı, Habib Gültekin, Ege Özgün, Mehmet Günay, Ihor Pavlov, Andrey Rybak, Mite Mihailkov, and Umut Bostancı for their support.

This work have been possible with support of The Scientific and Technological Research Council of Turkey (TÜBİTAK) through projects 110T790, 110T589, and 112T091; and a financial assistance via the program 2224-A (Support for Participation in International Events) was given for dissemination of the results at Complex Nanophotonics Science Camp in London, UK. Main part of fabrication, characterization, and experiments has been done using facilities of Advanced Research Laboratories (ARL, İAL) of Department of Physics in Bilkent University. At many points, facilities of The Center for Solar Energy Research and Applications (GÜNAM) at Middle East Technical University (METU, ODTÜ) and Institute of Material Science and Nanotechnology (UNAM) at Bilkent University have been used.

Finally, I would like to express my gratitude to my family, my father İbrahim Karademir, my mother Hamide Karademir, and my brothers Osman and Orhan Karademir for their endless support and their patience during my hardest times.

In dedication to my mother, Hamide Karademir.

Contents

List of Figures

List of Tables

Chapter 1

Introduction and Theoretical Background

Upon following the advancements of nanofabrication technologies, there have been increasing amount of interest in the light matter interaction at the nanoscale. Although surface plasmons (SPs) have been initially proposed as a new loss mechanism in electron energy loss experiments [1], they captured the focus of researchers once it was understood that they can also be excited with photons [2], forming surface plasmon polaritons (SPPs). The field of nano optics, however, requires confinement of light beyond the diffraction limit. SPPs, already propagating at metal-dielectric interface, offer further confinement in lateral directions beyond the diffraction limit of light [3]. At this level of locality, electric field component of light interacts with the surrounding dielectric several more times compared to non-localized light [4] which leads to surface-enhanced Raman spectroscopy [5] with capability of probing single molecules and nano particles [6] and other applications [7–10].

While many texts start discussing SPPs with the Lycurgus cup [11], the physics of surface plasmons came into the spotlight with the work of Ritchie [1]. As following demonstrations involved mainly electron loss spectroscopy [12][15], optical loss experiments quickly ensued [2, 12–16] connecting the field to its contemporary state. The field of nanoplasmonics, as it is known today, started with the demonstration of extraordinary transmission through a silver film with periodic nano-holes as observed by Ebbesen et al. [17]. A second wave of excitement have stirred the community after first demonstrations of plasmonic lasers [18, 19] following the theoretical framework laid down by Bergman and Stockman [20]. In the last two decades, plasmonics has been an active area of study with interesting physics, and new problems emerging almost every day.

In this thesis, interaction of surface plasmons with the surrounding medium is investigated through SPP-Exciton interaction. Coupling between SPPs and excitons can be investigated in two regimes of energy transfer. If the coupling is weak [25], state functions of SPPs or excitons is not altered, but perturbed. In the strong coupling regime [21], however, two particles form new quasi particles called plexcitons [22]. It is possible to tune the interaction strength of SPP-Exciton coupling from weak coupling to strong coupling regime by altering material properties of metals [21, 23] (Chapter 3). Furthermore, plasmonic band gap formed by patterning the metal surface with periodic corrugation can alter the SPP mode distribution and allow us to manipulate SPP-Exciton interaction by varying the pattern [24] (Chapter 4). Further, a new platform for investigation of SPP-Exciton coupling, plexcitonic crystals, is proposed and demonstrated which exhibit directional control of SPP-Exciton interaction [25] (Chapter 5). By special nano-pattering, SPP confinement in the propagation direction with Moiré cavities is demonstrated [26] (Chapter 6). The slow plasmon mode in the Moiré cavity can form the feedback structure of plasmon laser and can be used as an amplifier (Chapter 7).

In order to discuss the materials in following chapters, this chapter starts with a brief summary of the electrodynamics of light incident on materials, then, optical response of metals are discussed. Finally, detailed analysis of the physics of surface plasmon polaritons is made in the framework of light incident on metal surfaces. Specific theoretical background will be given on a chapter by chapter basis in order to present a coherent text consisting of self-sufficient individual parts.

1.1 Electrodynamics of Light Incident on Matter

In order to understand the optical properties of surface plasmon polaritons, it is important to lay down the electrodynamics of light that is incident upon material. As will be shown, when light propagates through material, it interacts with the medium by moving charges around. Light propagating inside a medium has a lower speed than the light propagating in vacuum. In fact, refractive index of a material, n, is the ratio of these speeds. There have been many attempts to explain this phenomena; Huygen's description [27] might be counted as a successful one, which, for the first time, treats light as a wave. However, dealing with refraction and other optical properties of light in medium at the atomic level, one has to take into account the electromagnetic nature of light. In this section, light-matter interaction will be explained within the classical electrodynamics framework. A more rigorous explanation can be given using quantum electrodynamics and field quantization framework, which would also lead to many other phenomena, such as single photon interactions, coherence, squeezed states etc. [28]. However, for almost all of the purposes of this thesis, classical picture is simpler and more comprehensible.

Response of matter to incident light can be studied through the well known Maxwell equations as framed, in vacuum, by James Clerk Maxwell [29], which are [30],

$$\nabla \times \mathbf{E} = -\frac{\partial \mathbf{B}}{\partial t} \tag{1.1a}$$

$$\nabla \times \mathbf{H} = \frac{\partial \mathbf{D}}{\partial t} + \mathbf{J} \tag{1.1b}$$

$$\nabla \cdot \mathbf{D} = \rho \tag{1.1c}$$

$$\nabla \cdot \mathbf{B} = 0 \tag{1.1d}$$

and,

$$\nabla \cdot \mathbf{J} = -\frac{\partial \rho}{\partial t} \tag{1.2}$$

Throughout this thesis, bold variables denote vectors. $\mathbf{E}$ and $\mathbf{H}$ are electric and magnetic fields respectively and $\mathbf{D}$ and $\mathbf{B}$ are dispecament field and magnetic flux density. $\mathbf{J}$ is the current density and ρ is the charge density (, and t is time just to be clear.)

In the discussion of what happens to a material when an electromagnetic field is incident upon, two more relations enter the picture,

$$\mathbf{B} = \mu_0 \mathbf{H} \tag{1.3a}$$

$$\mathbf{D} = \epsilon_0 \mathbf{E}, \tag{1.3b}$$

where μ_0 denotes magnetic permeability, and ϵ_0 denotes electric permittivity, both of which can also be expressed as tensors to account for the anisotropy of matters. Application of an external electric field does basically two things to the material, it perturbs the electrons at their orbits, and it aligns permanent polarizations within. Displacement field then, represents the total charges displaced within that material as

$$\mathbf{D} = \epsilon_0 \mathbf{E} + \mathbf{P} \tag{1.4}$$

where $\mathbf{P}$ is the polarization per unit volume.

Dipole moment, p, of an atom is defined in terms of the local electric field [31],

$$p = 4\pi\epsilon_0 \alpha E_{local}, \tag{1.5}$$

where α is the polarizability of the atom. Then the polarization of the crystal follows,

$$P = \sum_j N_j p_j \tag{1.6}$$

Here, N_j is the concentration and j goes over the atomic sites on the lattice. Polarizability is related to the dielectric constant via the susceptibility [Eq.(1.7) [31], then, for materials that can be polarized linearly and isotropically as a function of the applied electric field, $\mathbf{P}$ reads,

$$\mathbf{P} = \chi_e \epsilon_0 \mathbf{E}. \tag{1.7}$$

Here χ_e measures how susceptible that material is to the externally applied field. For non-linear materials, polarization has higher order components of electric field. Although χ_e can be a tensor, for the kinds of materials that will be discussed in this thesis, it is a scalar. Hence combination of Eq.(1.4) and Eq.(1.7), and comparison to Eq.(1.3b) gives,

$$\epsilon = (1 + \chi_e)\epsilon_0 \tag{1.8}$$

where the quantity $(1 + \chi_e) \equiv \epsilon_r$ is the relative dielectric constant, ϵ/ϵ_0. With similar motivations and algebra, relative permeability, $\mu_r \equiv \mu/\mu_0 = (1 + \chi_m)$, is defined. All of the materials that are used in this work are non-magnetic materials, so most of the times μ_r is unity and generally ignored. Square root of relative dielectric constant is defined as the refractive index, n, which is commonly used and can directly be measured using an ellipsometer.

Many of the dielectric properties of a material can be explained classically with above relations. However, plasmons in contact with an excitonic medium need more rigorous models. Even then, a semi-classical model works for many applications [32].

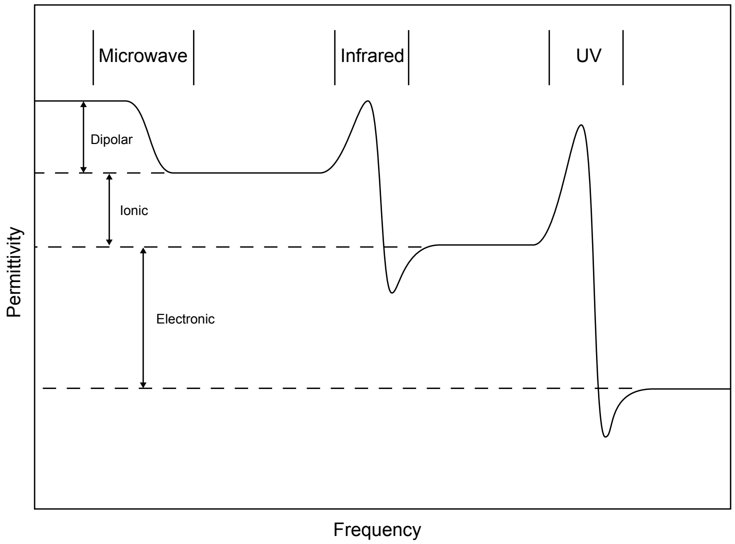

Figure 1.1: Frequency dependent contributions to permittivity. Adapted from Ref.[38]

The response of matter to incident light is manifested in the frequency dependent polarizibility [31], which for an uncharged lattice, consists of three main contributions (Fig.1.1). Electronic polarizability is observed at high frequencies due to the slow response of the nuclei to the external field, compared to the fast response of the surrounding valence electrons. Electronic polarization has resonance in UV part of the EM spectrum. At lower frequencies, in the infrared part of the spectrum, ionic contributions come into play. These are related to the movements of the lattice ions, which are heavy and thus respond to infrared frequencies. Infrared frequencies are also related to the lattice vibrations and heating of the crystal. At lower still frequencies, in the microwave region, contributions from the permanent dipoles become important [31]. Thus the response of the matter to incident electromagnetic wave is expressed through the dielectric function.

Surface plasmon polaritons are excited at frequencies below the vicinity of UV transition. This transition is labelled as plasma frequency and, for metals, it is calculated with Drude-Lorentz model which is to be discussed next.

1.2 Optical Response of Metals

Optical properties of metals, and hence, plasmons involve the electronic dipole transition mentioned above, the theoretical framework of which was presented by Paul Drude and is generally called Drude-Lorentz model [33].

In Drude-Lorentz oscillator model, electrons responding to external electric field are imagined as bound objects and modeled as a damped harmonic oscillator [33]. The equation of motion for single electron is given as [34],

$$m_0 \frac{d^2x}{dt^2} + m_0 \gamma \frac{dx}{dt} + m_0 \omega_0^2 x = -eE, \tag{1.9}$$

where m_0 is the mass of the electron, γ is the damping term of the oscillator, ω_0 is the resonance frequency of the oscillator, e is the electric charge, and E is the electric field, hence $-eE$ is the driving force. Assuming the electric field has harmonic time dependence,

$$E(t) = E_0 e^{-i\omega t - \phi}, \tag{1.10}$$

then Eq.(1.9) gives,

$$-m_0\omega^2 X_0 e^{-i\omega t} - i m_0\gamma\omega X_0 e^{-i\omega t} + m_0\omega_0^2 X_0 e^{-i\omega t} = -eE_0 e^{-i\omega t}, \tag{1.11}$$

where X_0 is the displacement amplitude of the electron from the nucleus. Here, the nucleus is assumed to be stationary, or $m_N \gg m_0$. Displacement amplitude can be singled out as,

$$X_0 = \frac{-eE_0/m_0}{\omega_0^2 - \omega^2 - i\gamma\omega}. \tag{1.12}$$

Displacement of the electron gives the time variable dipole moment of single electron, $p(t)$. In the macroscopic picture, where there are N numbers of nuclei present in the lattice per unit volume, the resonant polarization reads,

$$P_r = \frac{Ne^2}{m_0}\frac{1}{(\omega_0^2 - \omega^2 - i\gamma\omega)}E. \tag{1.13}$$

Combining Eq.(1.4), Eq.(1.8), and Eq. (1.13), relative permittivity is obtained as,

$$\epsilon_r(\omega) = 1 + \chi_e + \frac{Ne^2}{\epsilon_0 m_0}\frac{1}{(\omega_0^2 - \omega^2 - i\gamma\omega)}. \tag{1.14}$$

Above expression is complex. Real and imaginary parts are,

$$\epsilon_1(\omega) = 1 + \chi_e + \frac{Ne^2}{\epsilon_0 m_0}\frac{\omega_0^2 - \omega^2}{(\omega_0^2 - \omega^2)^2 - (\gamma\omega)^2}, \tag{1.15}$$

and

$$\epsilon_2(\omega) = \frac{Ne^2}{\epsilon 0 m_0}\frac{\gamma\omega}{(\omega_0^2 - \omega^2)^2 - (\gamma\omega)^2} \tag{1.16}$$

respectively [33]. ϵ_1 and ϵ_2 are used for real and imaginary parts of the relative permittivity. Here $\frac{1}{\gamma} = \tau$ is the mean free time for an electron to scatter from another ion or electron. τ is typically on the order of few femtoseconds [35]. Low frequency limit of the Eq.(1.14) gives,

$$\epsilon_r(0) = 1 + \chi_e + \frac{Ne^2}{\epsilon_0 m_0 \omega_0^2} \tag{1.17}$$

and high frequency limit gives,

$$\epsilon_r(\infty) = 1 + \chi_e. \tag{1.18}$$

Table 1.1: Free electron properties and Drude plasma frequencies of certain noble and other metals calculated via Drude model. Adapted from Ref.[31]

Metal	Valance Shell Electrons	N (10^{28} m^{-3})	$\nu_p = \omega_p/2\pi$(THz)	λ (nm)
Ag	1	5.86	2170	138
Au	1	5.90	2180	138
Cu	1	8.47	2610	115
Al	3	18.1	3820	79
Be	2	24.7	4460	67

By considering only the resonant polarization contribution, Eq.(1.17) can be written as [36],

$$\epsilon(\omega) = 1 - \frac{\omega_p^2}{\omega^2}, \tag{1.19}$$

where ω_p is defined as the plasma frequency of the metal, and is given as,

$$\omega_p^2 = \frac{4\pi N e^2}{m_0}. \tag{1.20}$$

Here, the plasma frequency is identified as the resonance frequency of the plasmons, akin to a plasma which is a medium that consists of equal amounts of positive and negative charges while only one of the types is mobile [37]. At frequencies exceeding the plasma frequency, the metal becomes transparent which is also known as ultraviolet transparency of metals [37, 38]. In Table 1.1 plasma frequencies of some metals calculated with Drude model are presented.

Although Drude model can predict plasma frequency of some metals (alkali metals, for example) with good accuracy, it cannot account for the plasma frequency of some other metals. For instance, according to Drude model, Ag and Au are expected to display almost identical behaviour. Ag has the electronic configuration of [Kr]4d^{10}5s^{1} and Au has the electronic configuration of [Xe]4f^{14}5d^{10}6s^{1}. However due to complex band structures of metals, transitions between bands are possible. These transitions are due to highly crowded *d* bands which have 10 electrons. Ag has an interband transition energy of 4 eV [39] which corresponds to 310 nm wavelength or 970 THz frequency, and it is much lower than the plasma frequency calculated with Drude model (2170 THz). On the other hand, the first *d*-band transition of Au is around 2.8 eV [40] or 440 nm wavelength or 677 THz which is lower still. Hence, even if Au and Ag have identical optical properties calculated with Drude model, in reality, interband transitions dominate the wavelength of plasma resonance and bring down the plasma frequency. Since Au has a lower plasma resonance than Ag, it has the golden yellow hue, as shorter than 440 nm wavelengths are not reflected.

1.3 Surface Plasmon Polaritons

The discussion in the previous section considered bulk or volume plasmons. In this section, we will discuss surface plasmons as it is difficult to access bulk plasmons by optical means. Following the Maxwells equations, Eq.(1.1), it can be shown that a thin metal film on a dielectric can support propagation of surface charge density waves with a range of frequencies from $\omega = 0$ to $\omega = \omega_p/\sqrt{2}$ support propagating surface electron waves, depending on the propagation vector, $\mathbf{k}$. In order to derive the dispersion relation of surface plasmons, consider the problem presented in Fig. 1.2. Two semi infinite media are bound together at an interface. SPs live in this interface. Assuming that waves with vectors, $\mathbf{k}_1$ and $\mathbf{k}_2$ are TM

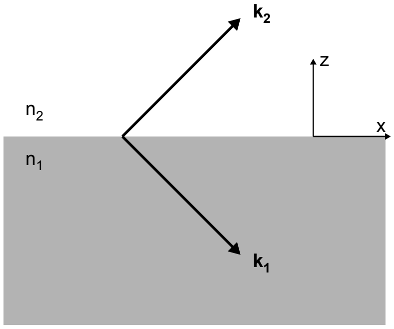

Figure 1.2: Schematic description of the problem of surface waves propagating between two semi infinite media.

waves, associated fields read [41],

$$
\begin{aligned}
z > 0 \qquad\qquad & \mathbf{H_2} = H_{y2} \exp i(k_{x2}x + k_{z2}z - \omega t)\hat{y} \\
& \mathbf{E_2} = (E_{x2}\hat{x} + E_{z2}\hat{z}) \exp i(k_{x2}x + k_{z2}z - \omega t) \\
z < 0 \qquad\qquad & \mathbf{H_1} = H_{y1} \exp i(k_{x1}x - k_{z1}z - \omega t)\hat{y} \\
& \mathbf{E_1} = (E_{x1}\hat{x} + E_{z1}\hat{z}) \exp i(k_{x1}x - k_{z1}z - \omega t)
\end{aligned}
\tag{1.21}
$$

where $\hat{x}, \hat{y}, \hat{z}$ are unit vectors in x, y, z directions respectively.

Continuity conditions at the boundary require,

$$E_{x1} = E_{x2} \qquad\qquad H_{x1} = H_{x2} \qquad\qquad \epsilon_1 E_{z1} = \epsilon_2 E_{z2} \tag{1.22}$$

Using Eq.(1.1) and continuity relations above, two sets of equations are obtained,

$$
\begin{aligned}
H_{y1} - H_{y2} &= 0 \\
\frac{k_{z1}}{\epsilon_1} H_{y1} + \frac{k_{z2}}{\epsilon_2} H_{y2} &= 0
\end{aligned}
\tag{1.23}
$$

and,

$$k_x^2 - k_{zi}^2 = \epsilon_i \frac{\omega^2}{c^2}, \tag{1.24}$$

since, $k_{x1} = k_{x2} = k_x$. Combining Eq.(1.23) and Eq.(1.24), the dispersion relation is obtained as,

$$k_x = \frac{\omega}{c} \left(\frac{\epsilon_1 \epsilon_2}{\epsilon_1 + \epsilon_2} \right)^{\frac{1}{2}}. \tag{1.25}$$

For real values of k_x, SPP modes become confined to metal-dielectric interface, and k_z in both media becomes imaginary. Hence fields in Eq.(1.21) becomes exponentially decaying functions along z. Evanescent tails of SPP mode excited with 600 nm light, propagating at Ag-Vacuum interface is shown in Fig. 1.3.

In order for k_x to be real, and hence exponential at Eq.(1.21) to be a plane wave function, $\Re(\epsilon_2) < 0$ and $|\Re(\epsilon_1)| > \epsilon_2$ conditions should be met [42]. Also in

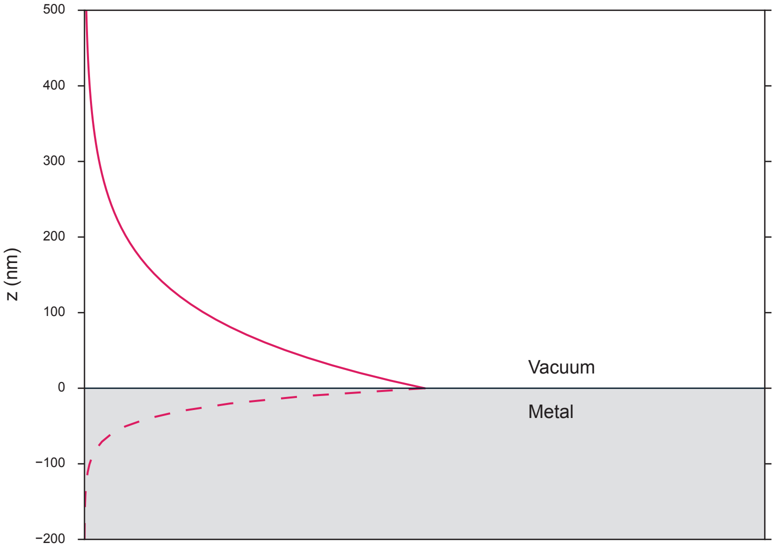

Figure 1.3: Evanescent tails of propagating SPP excited with 600 nm light. Penetration into the metal layer is significantly less than penetration into the vacuum.

the limit $\Re(\epsilon_2) \rightarrow \epsilon_1$ radial frequency at Eq.(1.25) approaches to,

$$\omega_{sp} = \left(\frac{\omega_p^2}{1 + \epsilon_2} \right)^{\frac{1}{2}} \tag{1.26}$$

for large values of k_x [42]. Note that for vacuum $\omega_{sp} = \omega_p/\sqrt{2}$, however due to d-band transitions, this resonance frequency also shifts. In Fig. 1.4 we plot the dispersion curve of plasmons, based on Eq. (1.25). The metal medium is Ag, whose optical properties are taken from Ref. [43]. In this case plasma frequency, $\omega_p/2\pi$, is 910 THz, whereas surface plasma frequency, $\omega_{sp}/2\pi$, is 880 THz. Between two resonances an anomalous dispersion region is observed [44].

Notice also that, in TE case, continuity at the boundary gives,

$$E_{y1} = E_{y2} \qquad H_{x1} = H_{x2} \qquad \frac{H_{z1}}{\mu_1} = \frac{H_{z2}}{\mu_2} \tag{1.27}$$

which leads to,

$$E_y(k_{x1} + k_{x2}) = 0. \tag{1.28}$$

Thus, in order to satisfy Eq.(1.28), either E_y should be zero or k_{x1} and k_{x2} should have opposite signs. In either case, a bound state is not supported. Hence surface plasmons are excited only with TM polarized light.

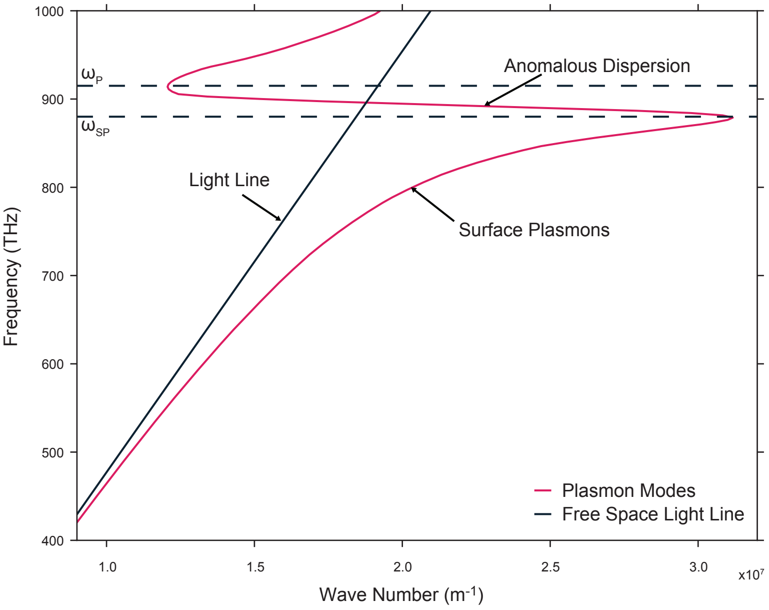

Figure 1.4: Dispersion curve of SPPs at the interface of Ag and vacuum.

As the SPPs propagate at the interface between two media, the evanescent tail of the mode reaches to some extent inside both media. In fact, SPPs interact with the matter via these evanescent tails. Penetration length of these tails are calculated via Eq.(1.24), since $z_i = 1/|k_{zi}|$,

$$\begin{aligned} z_2 &= \frac{\lambda}{2\pi}\left(\frac{\Re(\epsilon_1)+\epsilon_2}{\epsilon_2^2}\right)^{\frac{1}{2}}, \\ z_1 &= \frac{\lambda}{2\pi}\left(\frac{\Re(\epsilon_1)+\epsilon_2}{\epsilon_1^2}\right)^{\frac{1}{2}} \end{aligned} \tag{1.29}$$

are the lengths where the intensity of $\exp(-|k_{zi}||z_i|)$ becomes $1/e$ [42]. Considering Ag and vacuum, at 540 nm wavelength penetration into the vacuum is 370 nm, and is 23 nm in Ag.

Penetration depth of SPP modes in metal and vacuum for various excitation wavelengths is shown in Fig. 1.5. Penetration into the metal decreases as wavelength goes to infrared, which also reduces ohmic loss, at the same time penetration into dielectric increases. At infrared wavelengths, propagation length of SPPs also increases [3, 45].

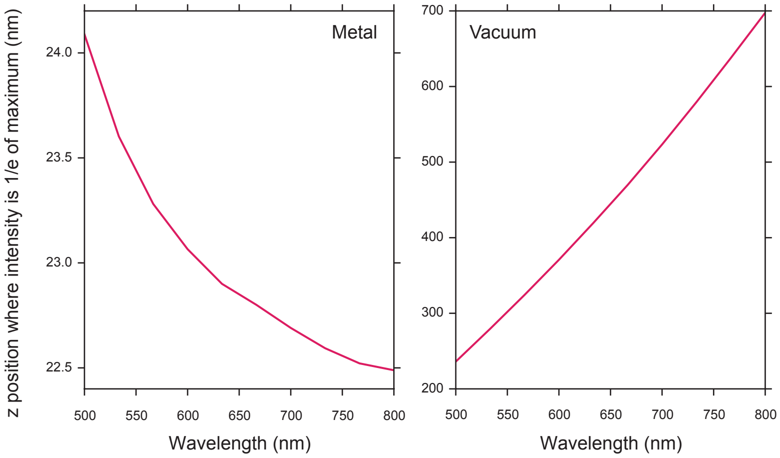

Figure 1.5: Penetration of SPP mode into metal and vacuum where the intensity reduces to $1/e$ of the maximum for various excitation wavelengths.

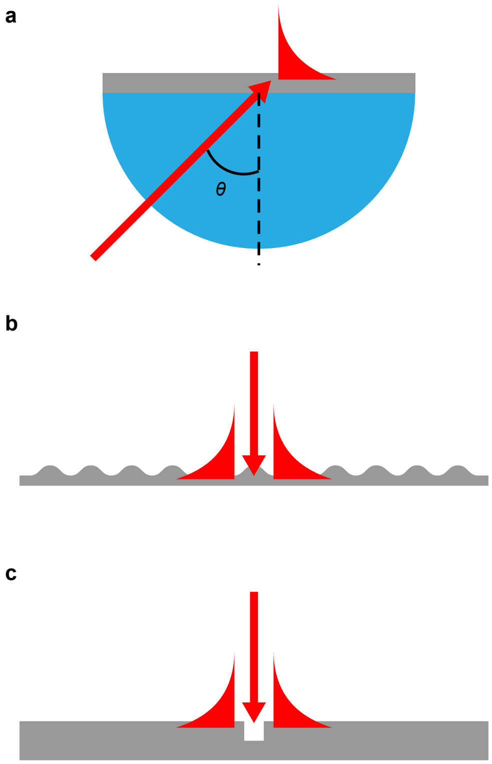

Figure 1.6: Three methods to compensate for the momentum mismatch between photons and SPPs. (a) is Kretschmann configuration [18]. (b) is grating coupler, and (c) is notch/slit coupler.

An important remark to make is that, the dispersion of SPPs, Eq.(1.25), gives wave vectors that are always greater than that of free space photons(, dispersion relations of which is $k_0 = \omega/c$). This leads to the momentum mismatch between photons and SPPs with the same energy. Thus, in order to couple the photon to the plasmon mode, momentum of the photon should be increased. There are several known ways to couple photons to SPP modes. In Fig.1.6, well known methods to compensate for the momentum are shown. Fig.1.6a is the Kretschmann configuration (also known as attenuated total reflection, ATR, method). In this method, the light is incident to the sample from the opposite surface through a high index medium such as glass. Light inside the glass has higher momentum compared to light in vacuum. Adjusting the incidence angle, resonant SPP mode can be excited. Fig.1.6b uses a grating coupler to couple incident light to the surface mode. In this case, integer multiples of spatial frequency of the grating is added to the momentum of free space light. Fig.1.6c uses a slit or notch on the surface. The slit has virtually infinite spatial frequencies, because of Fourier transform of the square function.

In this thesis, SPPs are excited via Kretschmann configuration, thus a detailed explanation should be given. In this configuration, momentum matching relation is given as,

$$k_{SPP} = k_0 n_p \sin(\theta), \tag{1.30}$$

where θ is the incidence angle, and $\sin(\theta)$ gives the horizontal component of k_0, momentum of free space light, and n_p is the refractive index of the prism. Hence $k_0 n_p$ is the momentum of light inside the prism.

In Fig.1.7, effect of the prism on free space light is shown. For this case prism is chosen to be of BK7 glass. Inside the prism, light has more momentum. Also, varying the incidence angle, one can shift the dashed light line between solid dark line and free space light line. Note that, light line of BK7 prism is exactly equal to the free space light line when the incidence angle is equal to the critical angle, θ_c, of the prism [46]. By scanning both the incidence angle and the frequency of the light, one can construct the dispersion curve of SPPs for any SPP structure.

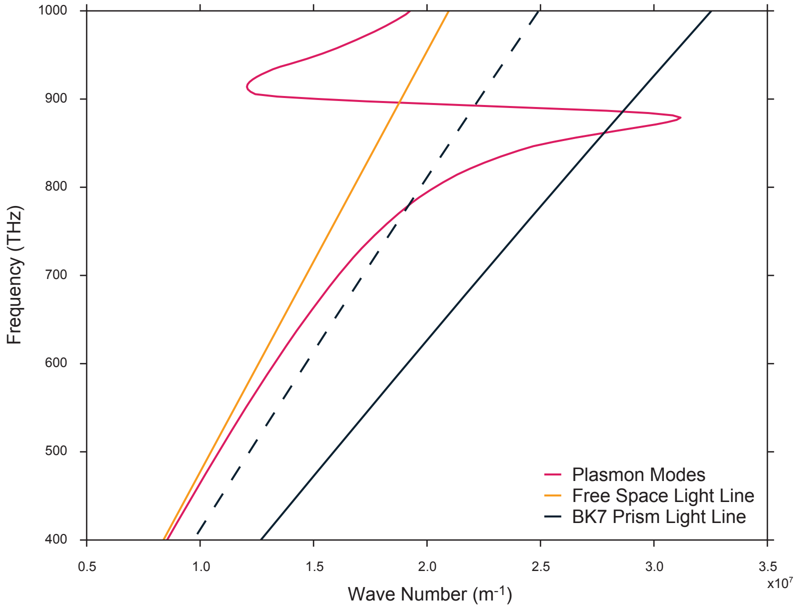

Figure 1.7: As the light passes through the prism, it gains momentum and light line of the light has less slope compared to light line of free space light.

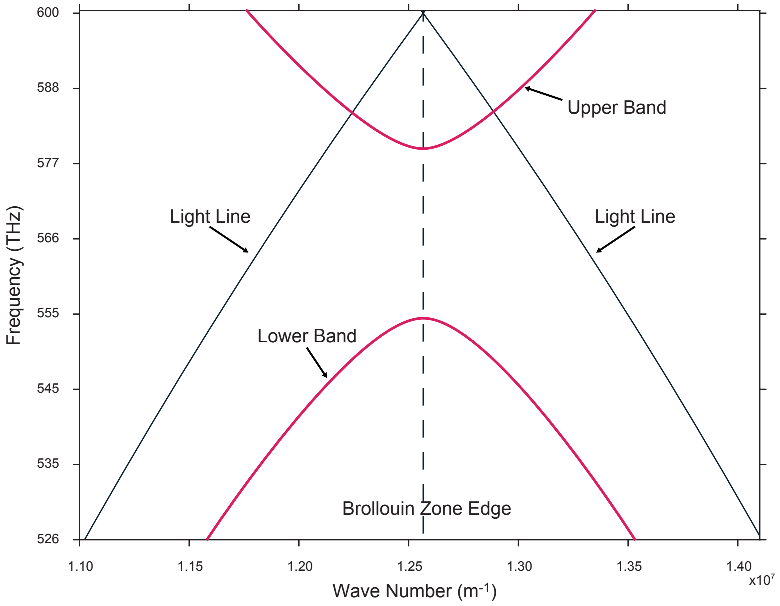

Figure 1.8: Band structure of the SPPs on 250 nm sine grating at the vicinity of its Brillouin zone edge. Brillouin zone edge is at $k = K \equiv \pi/\Lambda$, where Λ is the period of the grating. At the Brillouin zone edge, we see that backwards propagating SPPs with negative group velocities due to reflected SPPs from grating grooves.

A final remark on surface plasmons is that, if the surface is patterned with a grating just like Fig.1.6b, and the plasmons are excited with Kretschmann configuration, the degeneracy of forward and backward propagating plasmons breaks [47]. Consequently, two bands of plasmon modes emerge (Fig.1.8) as upper and lower bands where SPP dispersion curve intersects with the Brillouin zone edge of the grating. In Fig.1.8, band structure of 250 nm sine grating with 15 nm groove depth is presented. At the Brillouin zone edge, SPPs on lower and upper band edges have zero group velocities. Separation between bands increase with increasing groove depth [48]. Plasmonic band gap structures will be discussed in detail in Chapter 4.

Chapter 2

Sample Preperation and Measurement

In this chapter several experimental methodologies that are employed throughout this work will be presented in detail. Chapter starts with explanation of sample preparation and continues with the description of laser interference lithography method for patterning surfaces with grating profiles. Discussion of photometry technique for obtaining reflection maps of SPP structures follows. Then, a brief explanation of ellipsometry for obtaining optical constants of films is given. Finally, surface plasmon emission spectroscopy (SPES) as a method of light extraction from plasmonic structures is explained. This chapter lays the basis for various experiment methodologies used in the following chapters. However, in each chapter detailed explanations of specific methods are given.

2.1 Sample Preparation and Characterization

Sample preparation procedure is quite straight forward; it might be modified for different substrates.

For most of the experiments soda-lime glass are used as substrates. Soda-lime is an extremely cheap solution for a transparent substrate in the visible range of the spectrum. However, compared to its proper counterpart, BK7, its optical properties differ from batch to batch. So it is recommended to finish an experiment without changing the batch. Normally, a decent quality microscope slide pack will show a uniform optical property for all of its contents, but there are even cheaper solutions that may not even provide that. A better option is *Marienfeld* microscope slides, which are used for majority experiments presented in this thesis. They provide enough quality consistency across each package. For a final remark, both microscope slides (2 mm thick) and cover glasses (0.3 mm thick) for substrates have been tested. Cover glasses provide better uniformity of coated film thickness, however they lack the physical strength, hence generally one must use one cover glass sample for each part of the characterization (or a large sample may be broken into pieces). On the other hand, slides provide better physical strength across different kinds of usage; so one sample is generally enough for all kinds of characterizations (also slide samples can be sliced into smaller parts).

In order to achieve better consistency across samples, each substrate must be thoroughly cleaned. Conventionally, substrates come at their cleanest forms from manufacturers, but microscope slides generally doesn't count as clean room substrates hence manufacturers don't guarantee microfabrication-ready cleanliness, rather a sterile slide for biological use. Hence slides may bear many residues that are not suitable for microfabrication.

Very first step is to cut the slides into proper sample sizes. For typical interference lithography, a 1 cm × 1 cm sample is more than enough, but in order to achieve a consistent film thickness for at least 1 cm^2 sample area, a larger sample size is recommended.

In the first step of cleaning, each substrate is first bathed in acetone then in isopropanol pool inside an ultrasonic chamber for at least 2 min to get rid of glass residues or large particles that got stuck on the surface. Then, each sample is blow dried without rinsing in DI water. In the next step all samples are immersed in a piranha solution (H_2SO_4:H_2O_2, 3:1) for at least 5 min, after which they are rinsed under running DI water and bathed in DI water for another 5 min. Piranha cleaning is great for two reasons, it gets rid of hard organic (that even acetone can't dissolve) and some inorganic residues, and it makes the substrate surface hydrophilic which eases polymer application, later on. After DI bath, each sample is blow dried and then heated on a hot plate which is set at 110°C for 2 min to get rid of micro droplets of water. Surface roughness tests before and after the piranha application resulted in identical variation in surface defects, which are ±4 nm.

Dried samples are now ready for polymer coating. Several kinds of polymers are applied before pattern formation. Each polymer has its advantages and disadvantages. In order to achieve a uniform application of surface pattern, it is recommended to get rid of back reflection of light from the back side of the substrate. So an antireflection coating (ARC) is needed. AZ Chemicals BARLi II 200 ARC coating is used in order to prevent back reflection, which is applied with spin coating. At 4800 rpm and for 20 sec, the polymer is coated with 190 nm thickness. At this thickness it provides 95% prevention of reflection at 325 nm. Another method for preventing back reflection is to use a cover glass mounted with glycerin on the underside of the substrate. If the pattern is needed to be etched on the substrate, ARC coating will be an obstacle, hence the second option should be considered.

Second layer of polymer is photoresist (PR) layer. Mostly two types of photoresist are used; first one is Micro Chemicals S1800-4. This PR is a high resolution i-line PR with a very thin coated thickness. At 2000 rpm for 20 sec, S1800-4 is coated 90 nm. One can achieve a 140 nm thickness with 1000 rpm for 30 sec without compromising thickness uniformity; however after hard bake, this thickness reduces to 90 nm. So, S1800-4 is not suitable when a thick PR layer is needed (for instance if the patterning is done for lift-off purposes). The second type of PR that is used is AZ Chemicals 5214E, which is a widely used i-line PR across the cleanrooms worldwide. When spin coated with 5000 rpm for 20 sec, 5214E yields 1400 nm thickness.

Thickness of each layer, including the substrate becomes quite important during the exposure. Although the ARC layer is introduced in order to prevent back reflection from the substrate layer, an additional thick PR layer means the risk of coupled guided modes during exposure. These modes appear as fringes of various periods and shapes on the overall surface pattern. They appear randomly depending on the edge non-uniformity, shape of the substrate, non-uniformity of the PR and/or ARC thickness, or the slight slope given to the sample while mounting sample to the exposure table. Longer the exposure time, more visible the fringes become. These fringes may reduce the sample efficiency dramatically.

One way to reduce the occurrence of the fringes is to use thin PRs with thin substrates. However this may not be suitable if the sample is intended for repeated use. In this work, in order to reduce the fringes, statistics is used. In one exposure setting not more than 12 samples are exposed, 4 of which could easily be sacrificed. In a typical day, one could fabricate 8 almost identical samples, which was the exact number of samples that could be loaded on the holder of the thermal evaporator.

After polymer coating, samples are ready for exposure. It is not recommended to leave the samples for several days until exposure. Sooner the exposure is done, better. It is observed that one could wait for one day without losing sample yield, but after two days, yield is halved. Between polymer coating and exposure, samples are wrapped with an aluminum foil for protection from ambient light.

Exposure step has been explained in Sec.2.2 section in detail. After the exposure, sample is developed in a standard developer solution (AZ 400K:DI with 1:4 ratio.) for 10 sec. In order to control pattern depth, developing time is kept constant while exposure time is adjusted to fit the develop time, because exposure time gives better control. Immediately after development, a stop step is applied by immersing the sample in DI water for 20 sec. Sample is blow dried and visually inspected for quality. A grating structure diffracts light; hence if the depth of the grating is deep enough it can easily be seen under white light through steep angle. A trained eye can even guess the depth of the grating during visual inspection with ±10 nm error.

Either at this stage or after metal coating, each sample is characterized with an atomic force microscope (AFM) to confirm both pattern depth and pattern profile. It is a good practice to do AFM characterization after metal evaporation in order to get the most correct results.

Patterned samples are generally directly used as scaffolds for metal evaporation; however one may also copy the pattern with nano imprint lithography in order to get better identical samples.

Once the pattern is etched on the PR surface, a thin metal layer is evaporated to convert the sample to a plasmonic one. Metal evaporation is done in a *Leybold* Box Coater unit which houses a thermal evaporation bench. Main metal of choice is Ag which is a noble metal but never the less oxidises. Hence high vacuum conditions must be reached inside the chamber before evaporation. High vacuum conditions also provide a long mean free path, which affects metal film uniformity. Besides Ag, Au and Ti films are also coated.

After Ag evaporation, the sample is "plasmon-ready". However, in some cases a dielectric buffer layer should be laid down to prevent quenching of nearby quantum emitters. For this purpose a thin film of SiO_2 of 25 nm inside the same box coater chamber under Ar atmosphere could be sputtered on to the sample surface.

Once the plasmonic samples are ready, the final surface profile can be characterized with AFM and their pattern formation can be characterized with scanning electron microscope (SEM). Also some other layer of polymer with quantum emitters can be loaded with spin coating.

2.2 Laser Interference Lithography

There are two well known ways to obtain grating structures: ruling and holography. Ruling is basically done by scribing the substrate with a diamond cutter in a highly controlled manner. It has many peculiar tips and tricks with advantages and disadvantages like any other method, but,it is cumbersome, time consuming and expensive. The modern version of ruling can be considered e-beam writing of grating patterns. Interference lithography makes use of two or more d light beams interfering to form a periodic pattern on a special light sensitive surface prepared in advance. (Surface preparation is discussed in the last section of this chapter).

Laser interference lithography (also known as holographic lithography) is a recording of the interference pattern formed by two light sources [49]. In holography, basically, two coherent waves illuminate a light sensitive recording medium, one directly and the other reflected from an object. Traditionally, this technique is used for etching three dimensional image of an object on a surface, however, if the object is eliminated, two interfering beams form a diffraction grating [49]. On the holographic plane, both intensity and the phase information are recorded. In the case of the diffraction grating, hologram is a fringed image consisting of dark and bright lines [50].

Intensity distribution of the diffraction grating image is described by the interference relation,

$$I_r = I_1 + I_2 + 2\sqrt{I_1 I_2} \times \cos\phi, \tag{2.1}$$

where ϕ is the phase difference between the two beams, I_1 and I_2, and phase difference is due to the angle between two interfering beams. I_r is the intensity profile of the resulting fringe pattern [50]. Grating image forms as long as the light source is coherent. Continuous wave lasers provide the best solution compared to pulsed lasers with short coherence length, since coherence length is dependent on the bandwidth of the laser [50].

Two methods of laser interference lithography are in use in the industry and research: the Lloyds mirror setup and dual beam interference setup. Dual beam setup offers high resolution patterns whereas Lloyds mirror setup is used for exposure of large area of the sample at once [50]. In this thesis, the Lloyds mirror setup is used in the sample fabrication pipeline.

The Lloyds mirror setup (Fig.2.1a) consists of a single laser, focused with a converging fused silica lens to a pinhole. Focused beam is expanded approximately in 20 cm diameter in about 2 m distance, on which spot, a Lloyds mirror is centered (Fig.2.1c). In this setup, ideally, half of the light is directly incident on the substrate and the other half is reflected from a large mirror. Typically the mirror stands normal to the sample plane; hence the reflected half of the beam gains a 90° phase difference with respect to the reference beam. Focusing the laser beam produces an Airy disk profile at the focal point. Here, pinhole is a spatial filter that filters through the Gaussian center of the focused light.

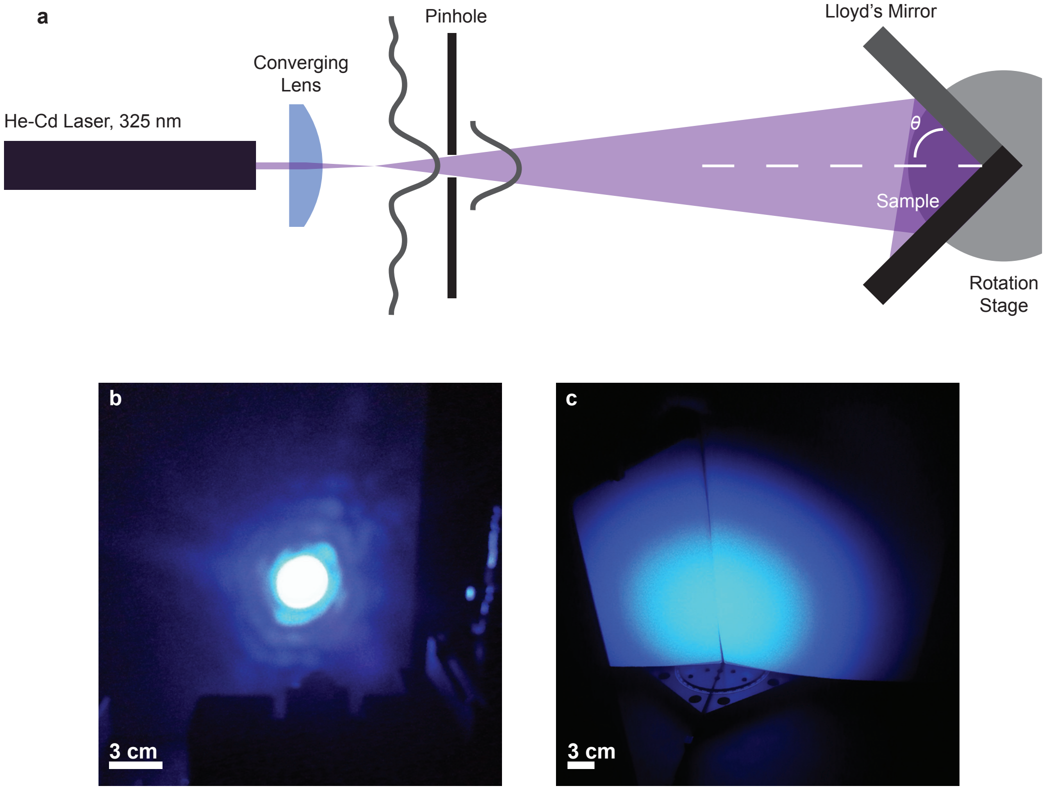

Figure 2.1: Lloyd's mirror setup. (a)Schematic representation of the setup. (b)Beam shape at the distance 10 cm from the pinhole. (c)Beam shape at the distance 2 m from the pinhole.

In Lloyds mirror setup, period of the grating image can be precisely controlled with the angle between the laser beam axis and the mirror, θ. The periodicity of the grating image is then calculated with,

$$\Lambda = \frac{\lambda}{2 \sin \theta}, \tag{2.2}$$

where λ is the wavelength of the laser. We note that, determining factor of Λ is θ, which is the argument of the sine function in the denominator; thus, Λ is not linearly dependent on θ. At large angles, Λ changes slowly with θ, whereas for small angles, Λ changes faster with θ. This makes controlling the grating pitch harder at small angles or for large grating periods. We also note that, since light leaving the pinhole is not collimated, grating period becomes chirped towards the edge of the beam shape; however chirping can largely be neglected when a 2 cm × 2 cm sample exposed at the center of a beam with 20 cm diameter.

Sine gratings are easily formed by single exposure. Moiré cavities need two consecutive exposures with slight shift in θ; two dimensional grating structures need two or Moiré cavities require four consecutive exposures one/two of which is done after azimuthal rotation of the sample (Fig.2.2c,d).

Laser interference lithography is the most flexible method to obtain grating patterns with almost infinite variations in pitch and profile, and with high repeatability. Special care must be given for setup alignment and sample preparation in order to achieve satisfactory results. However, even after the most careful work, defects can occur, examples of which can be seen in Fig.2.2b and Fig.2.2c where unintended bridges between grooves are noticeable.

2.3 Reflection Photometry

Photometry is the methodology of recording either transmittance or the reflectance (reflectometry) of a sample. Generally, photometry is performed for a spectrum of wavelengths. Together with Kretschmann configuration, reflectometry is used for recording of the reflection map of a plasmonic structure. Reflection map is constructed by scanning the reflection spectrum of a sample for

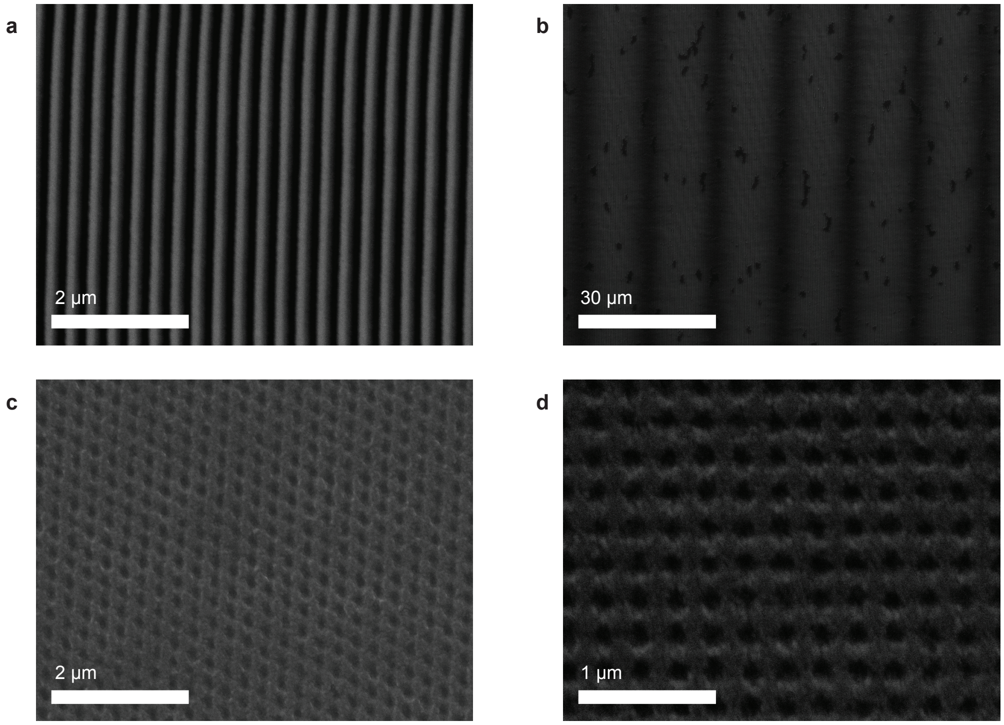

Figure 2.2: SEM Micrographs of various surface patterns. (a)Sine grating with 300 nm period. (b)Moiré cavity with 15 μm cavity size. (c)Triangular lattice of two 280 nm period sine gratings. (d) Square lattice of two 280 nm sine gratings.

each incidence angle. In order to convert the reflection map to a dispersion map, coordinate mapping is required. This conversion is discussed in Chapter 7.

Reflectometry measurements in this work are done with two setups: ellipsometer and white laser with acousto optical tunable filter (AOTF). A typical variable angle spectroscopic ellipsometer (VASE) has the capability of varying both the incidence angle and the wavelength of the incident light and generally offer recording of reflection or transmission. Most of the reflectometry measurements in this thesis are recorded with *J.A. Woollam Co. V-VASE* ellipsometer with capability to scan a wavelength range of 200 nm to 1100 nm with 0.1 nm resolution and angular span of 15° to 90° with 0.05° resolution.

The white laser setup is custom built using *Koheras SuperK Extreme* supercontinuum (white) fiber laser outcoupled to *NKT Photonics SELECT* AOTF, as light source. *OWiS P30* step motor is used for controlling rotary stage that the sample is mounted on, and *Newport 818-SL* Si photodetector is used for intensity recording. This setup offers the same angular resolution as the VASE alternative; however it lacks the spectral resolution. AOTF has the capability of discretizing white light to 4 nm bandwidth. Hence, fine plasmonic features like cavity states get lost or convoluted with other plasmonic features. Nevertheless, this setup proved itself useful for dark field microscopy experiments.

A Fourier Transform Infrared (FTIR) Spectrometer, which has a superior spectral resolution compared to both of the above methods, can also be used in the near infrared. Together with a high resolution motorized reflection stage this setup might give the best results. However, collimation of the current system needs to be addressed.

In Fig.2.3 reflection map recordings of all three methods are compared. VASE method (Fig.2.3a) offers the optimal angular and spectral resolution. Each reflection map is taken with a 9 μm Moiré cavity. Hence the cavity modes should span equal bandwidths.

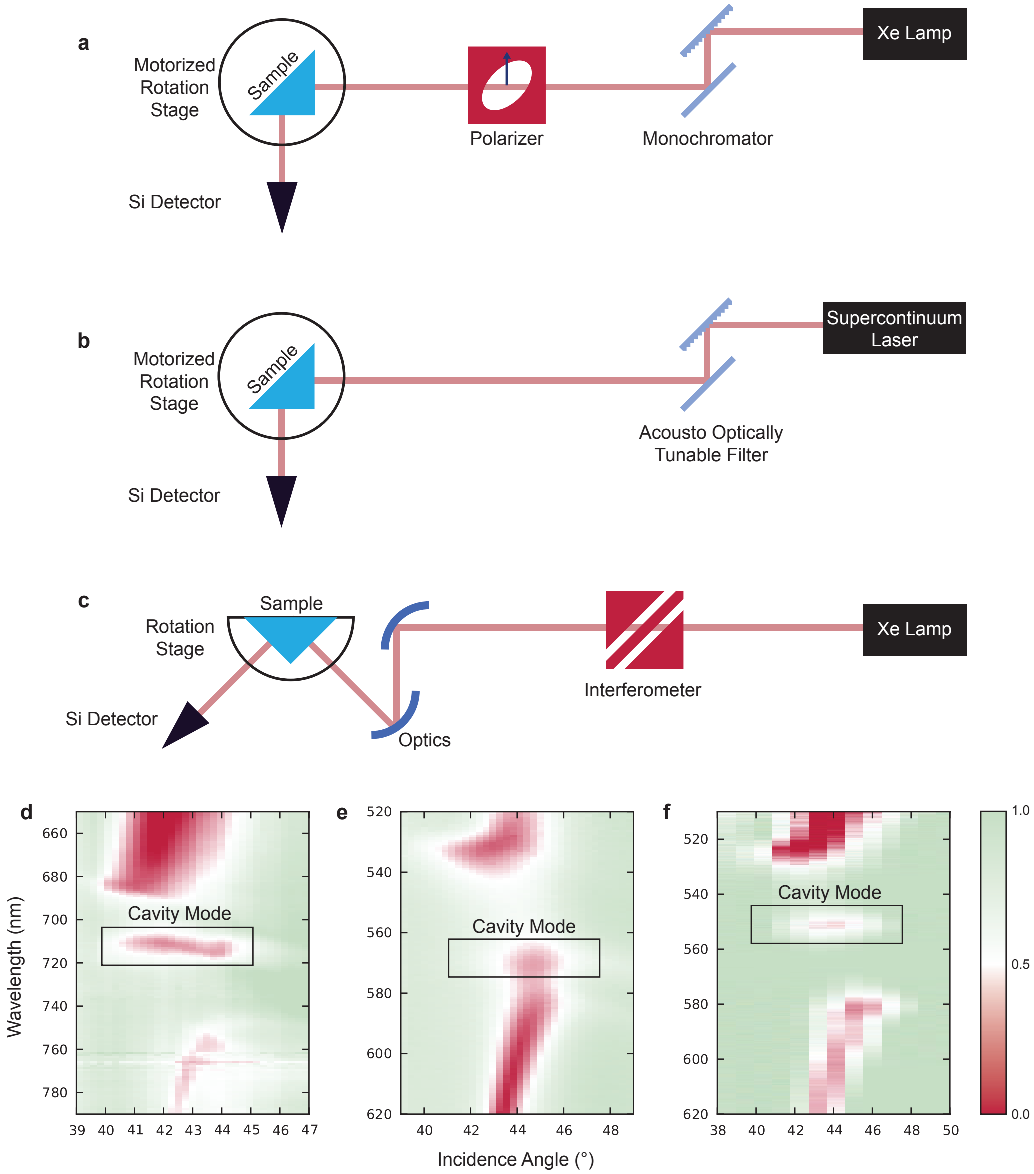

Figure 2.3: Comparison of reflection maps recorded with various setups. (a) Ellipsometer setup. (b) Custum reflectometer setup. (c) FTIR setup. Recording of a reflection map with (d) Ellipsometer with 9 μm Moiré cavity inside H_2O, (e) Custom reflectometer setup with 9 μm Moiré cavity in air, (f) FTIR Spectrometer and reflection module with another 9 μm Moiré cavity in air.

2.4 Ellipsometry

Ellipsometry is a powerful and reliable tool for determination of thickness and optical constants of thin films. All the ellipsometric measurements in this thesis are done with *J.A. Woollam Co. V-VASE*. In this section, a brief explanation of the physics of ellipsometry, and ellipsometry techniques that have been used for determining optical properties of different film types is given.

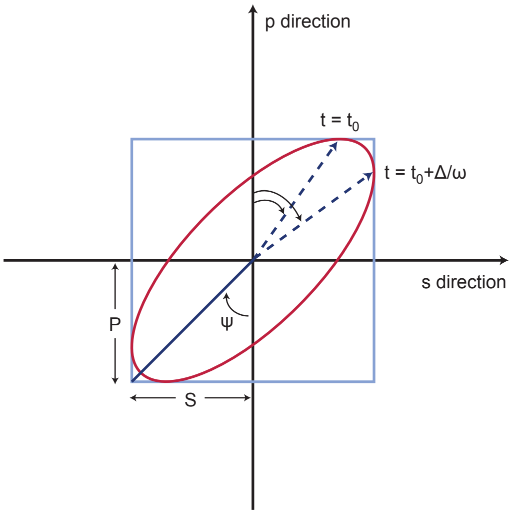

Figure 2.4: Polarization ellipse of light that propagates towards the reader.

Light is a transverse wave consisting of electric and magnetic components which are perpendicular to each other. The "ellipse", that ellipsometry measures is the polarization ellipse of the light. Polarization of light is the direction of its electric field component. The direction of polarization may change with time as the field oscillates with a frequency which determines the color perception of light. The trace of the maxima of the electric field at any time gives the polarization characteristics of the light. The most general shape of this trace is an ellipse (Fig.2.4). In the classical treatment of the electromagnetic wave function, the field is decomposed to plane waves, then perpendicular components of the electric field are taken [51],

$$\mathbf{E}(t) = \begin{bmatrix} E_s(t) \\ E_p(t) \end{bmatrix} = \Re\left(\begin{bmatrix} Se^{i\Delta} \\ P \end{bmatrix} \right) e^{i\omega(t-t_0)}. \tag{2.3}$$

Here, Δ is the relative phase of one component to the other. S and P directions are selected for convenience (Fig.2.4), where, in practice, P direction is the direction as the electric field component of light lies inside the incidence plane. If at time $t = t_0$, the amplitude p component of the beam is at its maximum, then at time $t = t_0 + \Delta/\omega$ the amplitude of s component becomes maximum. When Δ is positive (negative) the polarization is right (left) handed [51]. Another aspect of the S and P components are their amplitudes, which determine the relative amplitude phase, defined as $\tan\Psi = S/P$. The angle Ψ together with Δ determines the Jones vector [51],

$$\mathbf{J} = \begin{bmatrix} \sin\Psi e^{i\Delta} \\ \cos\Psi \end{bmatrix}. \tag{2.4}$$

If $\Delta = 0$ or π, polarization is linear; if $\Psi = \pi/4$, and $\Delta = \pi/2$ or $-\pi/2$, polarization is circular [51].

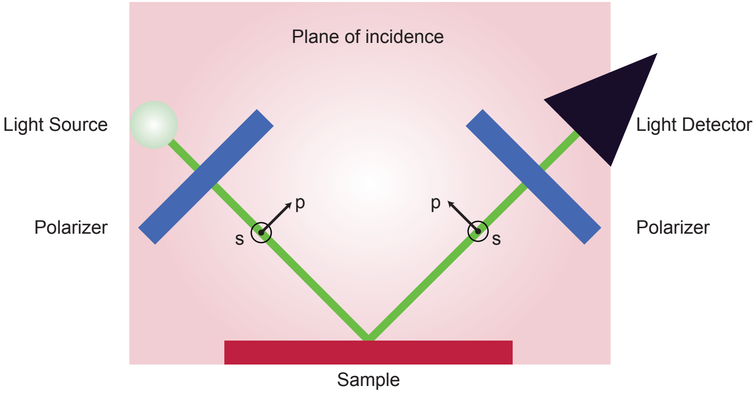

Figure 2.5: Schematic demonstration of basic ellipsometry setup.

Hence, ellipsometry is the technique of measuring and analyzing Ψ and Δ values for various configuration variations of light (polarization, wavelength) that are incident on various materials, in order to determine optical response of the material in question. Analysis is done by application of Fresnel equations to a layered material model and then fitting measured and simulated Ψ and Δ values with linear regression analysis.

Fresnel equations determine the Jones matrix which is composed of two Jones vectors [Eq.(2.4) for incident ($E^i_{p,s}$) and reflected ($E^r_{p,s}$) beams [52],

$$\mathbf{J} = \begin{pmatrix} E^r_p/E^i_p & E^r_s/E^i_p \\ E^r_p/E^i_s & E^r_s/E^i_s \end{pmatrix} = \begin{pmatrix} r_{pp} & r_{ps} \\ r_{sp} & r_{ss} \end{pmatrix} = \begin{pmatrix} \tan\Psi e^{i\Delta} & \tan\Psi_{ps} e^{i\Delta_{ps}} \\ \tan\Psi_{sp} e^{i\Delta_{sp}} & 1 \end{pmatrix},$$

where J is normalized to r_{ss} at the last step and X_{ps} and X_{sp} ($X = r$, Δ, or Ψ) terms are cross polarization terms which become crucial if the material is anisotropic [52]. Here, both $E^i_{p,s}$ and $E^r_{p,s}$ are complex waves. Fresnel equations of reflection from a single interface of two isotropic media (the cross polarization terms are zero) are [52],

$$r_{pp} = \frac{n_1 \cos\phi_0 - n_0 \cos\phi_1}{n_1 \cos\phi_0 - n_0 \cos\phi_1}$$

$$r_{ss} = \frac{n_0 \cos\phi_0 - n_1 \cos\phi_1}{n_0 \cos\phi_0 - n_1 \cos\phi_1}$$

where n_0 and n_1 are corresponding complex refractive indices of two media and ϕ_0 and ϕ_1 are angles between the propagation vector and the normal. Coefficients for multiple layers can be obtained with transfer matrix method [52].

In order to properly determine the optical properties of any material, care must be given to instrumentation and analysis. Determination of optical constants is done *ex situ*. Results of the computed and measured Ψ and Δ values are compared to each other via regression analysis through least squares method. The analysis is generally performed by a software package provided by the manufacturer of the ellipsometer. However the process is not fully automatic, and requires intervention at many stages.

Bulk of the work in this thesis is done on transparent glass substrates, and characterization of thin films on transparent substrates requires some tricks. Main problem with transparent substrates is the reflection from the bottom interface of the substrate. An easy alternative for the visible spectrum is to use an opaque substrate like Si for thin film characteristics and assume the same film growth characteristics on glass substrate. This is a useful approach when all that is needed is the optical characteristics of the film. However, the thickness after coating of the material may change from Si substrate to glass substrate due to the surface chemistry. Another trick for transparent substrate is to diffuse the back reflection by roughening the back surface. For this purpose, generally sticking a piece of scotch tape under the substrate does the trick.

Following the measurements of Ψ and Δ, modeling phase begins. There are few very commonly used dielectric models for modeling almost any kind of material. Special models should be implemented for anisotropic or exotic materials like graphene. The most general model for isotropic materials is the Lorentz oscillator model [52],

$$\epsilon(\lambda) = n^2(\lambda) = 1 + \sum_j \frac{A_j \lambda^2}{\lambda^2 - \lambda_{0j}^2 + i\eta_j \lambda}, \tag{2.5}$$

where η_j is the extinction coefficient and related to the width of the resonance peak of the oscillator and $n(\lambda)$ is complex. Commonly used approximation of Eq.(2.5) for dielectric materials without any optical resonance is the Cauchy expansion [52],

$$n(\lambda) = B_0 + \sum_j \frac{B_j}{\lambda_j^2} \tag{2.6}$$

Cauchy model fits well when the absorption of the material is almost zero. However, for a film containing a strong absorbent, like a j-Aggregate dye, original form of Eq.(2.5) should be used with a slight modification,

$$n^2(\lambda) = \epsilon_{\text{FILM}} + \sum_j \frac{A_j \lambda^2}{\lambda^2 - \lambda_{0j}^2 + i\eta_j \lambda}, \tag{2.7}$$

where ϵ_{FILM} is the refractive index of the host matrix without the absorbent.

Metals are traditionally modeled with Drude expression which is another approximation to Eq.(2.5) [52],

$$\epsilon(E) = 1 - \sum_j \frac{B_j}{E} \left(\frac{1}{E - i\Gamma_j} \right) \tag{2.8}$$

where E is the photon energy ($E = \hbar\omega_0$).

After determination of the optical constants of materials, they can be integrated into all calculations, be it transfer matrix method or FDTD to calculate plasmonic characteristics. Integration of experimental data into the simulations can be done with sampling refractive index, n, and loss, k, data. The software package that is mainly used in this thesis, *Lumerical FDTD Solutions*, allows for such an import of sampled data (and fits the data to a polynomial). However, there are alternative packages like *MEEP* from MIT that require manually fitted models. If all the materials in the simulation are dielectrics, function fits work well within the expected error limit. However, direct incorporation of ellipsometric data of strong absorbents, like j-Aggregates, to a standard FDTD package is difficult. A manual regression analysis between experimental and simulated data gives the correct parameters for the built in Lorentz absorber model. Such an analysis is done in Ref. [21] and in Chapter 3, and the resulting parameters are employed for later works in FDTD calculations.

For determination of refractive indices of prisms used in Kretschmann configuration, ellipsometry alone is of little use. One common way is to measure the critical angle of the prism for each wavelength of light and determine the refractive index using Snell's law. However, this method becomes extremely difficult to implement for high index ($n \geq 1.7$) prisms. Also, capturing dispersive behavior of the prism depends heavily on the angular resolution of the measurement. Instead, SPPs on plane metal surface can be used. In this method, reflection map of propagating SPPs on flat metal surface is recorded with Kretschmann setup. Then, using the dispersion relation of SPPs (see also Chapter 1),

$$k_{SPP} = \frac{\omega_0}{c}\left(\sqrt{\frac{\epsilon_{\text{METAL}}\epsilon_{\text{DIELECTRIC}}}{\epsilon_{\text{METAL}} + \epsilon_{\text{DIELECTRIC}}}}\right),$$

and $k_{SPP} = n_{\text{Prism}} k_0 \sin\theta$, refractive index of the prism for each wavelength can be extracted. Then these values may be fitted to Eq.(2.6) to obtain Cauchy coefficients.

2.5 Surface Plasmon Emission Spectroscopy

Direct measurement of SPP signals on the surface requires near field measurement methods like scanning near field optical microscopy (SNOM). However, SPP-exciton interaction can also be characterized in the far field through measurement of the emission of light decoupled from the SPPs.

We designed and constructed a setup to measure emission from SPPs which could be called surface plasmon emission spectroscopy (SPES) setup. In literature, similar setups have been used for extracting light from otherwise inefficient processes [53]. Also some setups couple two sides of the grating via surface plasmons [54–56]. In this work, SPES setup has been the central point of slow plasmon laser experiments. It might not be classified as a method, but the setup is based on and optimized for this conceptualization; hence it would not be an attempt in vain to describe the setup in detail.

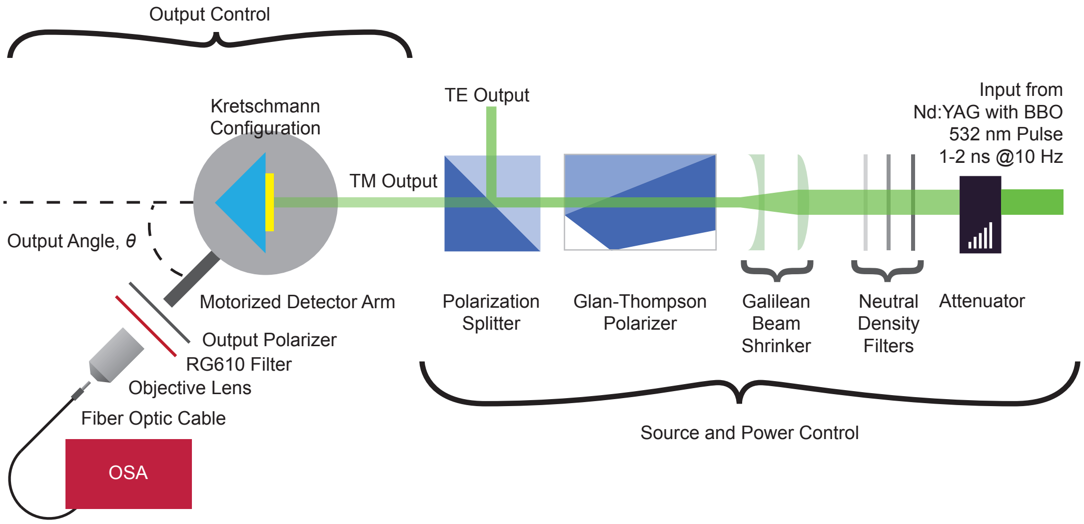

Figure 2.6: Surface plasmon emission spectroscopy setup.

SPES setup (Fig.2.6) consists of two main parts: one is the source and power control and the other is output control. Source and power control begins with a nanosecond duration pulsed Nd:YAG laser operating with 10 Hz repetition rate. Nd:YAG laser has emission at 1064 nm wavelength, but a β-Barium Borate (BBO) crystal at its output can double, triple, and quadruple the frequency of the output wavelength through second, third, and fourth harmonic generation and yield 532 nm, 355 nm, and 266 nm wavelengths respectively. *Spectra Physics Quanta Ray* series pump laser have been used which has all four output wavelengths. 532 nm output is filtered through using the optics at the output compartment of the laser.

Attenuator at the output of the laser gives a good control over high levels of power (>10 mW avg.) but its ability to control low powers is limited (<10 mW down to 0.2 mW avg.) (Fig.2.7c). Thin film (about 40 nm) of Ag breaks down for powers more than 25 mW avg. so the attenuator should be supported with additional optics.

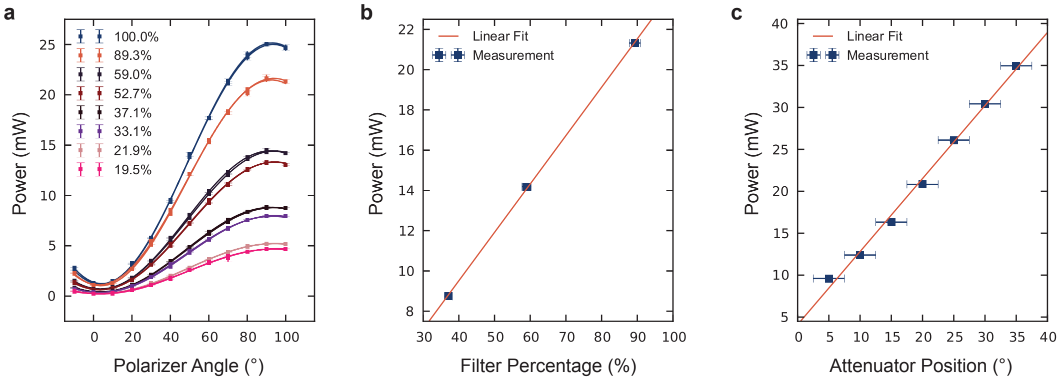

Figure 2.7: Averaged power output measurements of source and power control part of SPES setup. (a) Power output of Glan-Thompson Polarizer position with several ND combinations when attenuator is set at 25°. Curves are fitted $\cos^2\theta$ functions for both increase and decrease ($-10°$ to $100°$, $100°$ to $-10°$). (b) Based on these measurements power responses of ND filters. (c) Power response of the attenuator.

Neutral density (ND) filters give an additional attenuation control. Three ND filters that are $89.3\% \pm 2\%$, $59.0\% \pm 1\%$, and $37.1\% \pm 1\%$ have been used (Fig.2.7b). A more continuous control over the power output is obtained by using Glan-Thompson polarizer (GT) together with a polarization splitter. GT is used for rotating the polarization vector of the input light. Without any polarizer, Ng-YAG laser and the attenuator align the polarization as TM. NDs are polarization independent. GT then, changes the orientation of the TM component of the light (which is at its max. at the input.) TE component is filtered away with the polarization splitter. GT has $\cos^2\theta$ response. This response is clearly visible in Fig.2.7a where GT is tested for hysteresis. The power output is measured as GT is driven from -10° to 100° and back. For both directions resulting data points are fitted with $\cos^2\theta$. The results show that GT position returns the polarization at its original orientation for each $180.6^\circ \pm 1.5^\circ$. The small hysteresis on some measurements is within the error range, so one can safely assume that GT has no hysteresis. All plasmonic laser measurements are done by using this data and selecting suitable combinations of attenuator position, ND filters, and GT position to scan 0 mW to 27 mW power range more or less continuously. Recording of data is done by labelling of these combinations, all power data is converted to their mW values later on.

Chapter 3

Plasmon Exciton Coupling

Copyright Disclaimer:

Some parts of this chapter are published in *Physical Review B* as “Tuning surface plasmon-exciton coupling via thickness dependent plasmon damping” Sinan Balci, Coskun Kocabas, Simge Ates, **Ertugrul Karademir,** Omer Salihoglu, Atilla Aydinli, Phys. Rev. B. **86**, 235402 (2012) and reproduced here with permission of American Physical Society (APS). Systematic or multiple reproduction or distribution to multiple locations via electronic or other means is prohibited and is subject to penalties under law.

Some other parts of this chapter are published in *Optics Letters* as “Absorption enhancement of molecules in the weak plasmonexciton coupling regime” Sinan Balci, **Ertugrul Karademir,** Coskun Kocabas, Atilla Aydinli, Optics Letters **39**(17), 4994 (2014) and reproduced here with permission of The Optical Society (OSA). Systematic or multiple reproduction or distribution to multiple locations via electronic or other means is prohibited and is subject to penalties under law.

Controlling light-matter interaction plays a fundamental role in emerging optical phenomena, which have broad applications in optoelectronics, nonlinear optics, lasers, and spectroscopy. Cavity quantum electrodynamics (QED) provides quantum mechanical description for these fundamental interactions in confined geometries [57–61]. When an atom is placed in an optical cavity, the resonant modes of the cavity are coupled with electronic transitions of the atom. Trapped ions in high-Q cavities [57], Q-dots in photonic crystal cavities [58], and organic materials with excitonic transitions in optical cavities [59] can be understood within the framework of cavity QED. Excitonic materials placed in a plasmonic cavity provide a new platform to study cavity QED [3, 32, 61, 62]. Coupling between surface plasmons (SPs) on the metal surfaces [3] and excitons in optical materials results in a coupled quantum system [22, 32, 62–67].

Strength of coupling between two oscillators can be classified in strong and weak coupling regimes. The strength of coupling is characterized by comparing the rate of energy transfer between the matter and the cavity and the decay rates of the individual states. When the decay rate is significantly smaller than the rate of energy transfer, strong coupling regime is established [68]. Strong coupling [68] between excitons and SPs forms a coupled hybrid state, which arises when an exciton mode resonates with a plasmon mode [32]. Enhanced electromagnetic field of SPs and strong oscillator strength of excitons can provide the necessary conditions for strong coupling. In the weak plasmon-exciton coupling regime, the inherent nature of SPP and exciton modes are not modified and thereby increase the absorption or emission rates of the molecules [10, 69]. However, when the coupling is considered to be strong, SPP and exciton modes are modified by forming new coupled modes and hence an anticrossing behavior is observed in the dispersion curve [21, 62–66, 70–72]. Anticrossing is observed at the energy where both bare plasmon and bare exciton modes resonate at the same frequency. As it has been shown theoretically and experimentally, in the strong plasmon-exciton coupling regime, two newly formed energy states are separated by an energy value whose difference in energy is called the Rabi splitting energy. Rabi splitting energy is given by

$$\hbar\Omega_R = \sqrt{4V - (\gamma_p - \gamma_e)^2} \tag{3.1}$$

where V is the coupling parameter, γ_p and γ_e are the line-widths (i.e., damping) of the bare plasmons and bare excitons, respectively. The strength of this interaction determines both the absorption and emission properties of molecules placed near plasmonic structures, effectively governing the optical properties of such a hybrid system. Rabi splitting can be tuned in two ways; (i) by varying the excitonic properties of the matter like component (i.e. varying V or γ_e), or (ii) by controlling the properties of the plasmonic system (i.e. varying γ_p). Modification of excitonic properties has been demonstrated by varying the optical density of the excitonic system [63, 67] on flat metal surfaces, as well as reversible switching between the weak and strong coupling regimes via a photochemical process, which changes the strength of the dipole moment [70].

It has been shown that the thickness of the metal films (or the skin depth of the metal) affects the properties of the system under study and thereby control the amount of light absorbed or transmitted by the system [7, 73–75]. For example, a nano-hole array perforated thick metal film greatly boost the transmission of the incident light [3]. Conversely, when the thickness of the nanostructured metal film is decreased to around the skin depth of the metal (∼20 nm) opposite behavior has been observed, that is, transmission of the incident light is suppressed or, in other words, absorbance of the nanostructured film increases [74]. In earlier studies, it has been observed that when the metal film thickness is smaller than the penetration depth of the evanescent wave, absorbance of the metal film has been greatly increased [7, 75]. In another study it has been shown that broad band critical coupling of the incident light can be achieved by adjusting the thickness of the metal film . In a similar way, critical coupling has been investigated in coupled molecular and plasmonic cavity arrays [76]. Lately, tuning plasmon-exciton coupling and hence the Rabi splitting energy in the strong coupling regime by controlling the plasmon damping has been presented [21]. However, plasmon-exciton coupling below the skin depth of the metal has not been studied.

In this chapter, tuning of SP-exciton coupling by controlling the damping of the plasmonic component is demonstrated. It is possible to tune the Rabi splitting energies ranging from 0 meV to 150 meV by varying the plasmonic layer thickness, which defines the damping of the plasmonic mode. Absorption enhancement of the molecules in the weak plasmon-exciton coupling regime is investigated. Strength of the plasmon-exciton coupling has been controlled from the weak-coupling regime (exhibiting no anticrossing behavior) to the strong-coupling regime (exhibiting an anticrossing behavior) by plasmonic layer thickness. In addition, concentration of the dye molecules is very critical and determines the transition point from the weak-coupling regime to the strong-coupling regime. Analytical and transfer matrix study of the dispersion studies agree well with the experimental results. The ability to tune the SP-exciton coupling would make this system a promising candidate for a range of new applications [22,32,62–68,70,77].

3.1 Experimental

Fig.3.1a shows the schematic depiction of the Kretschmann configuration (KC) used for excitation of surface plasmons on the Ag film by polarized incident supercontinuum laser light modulated with an acousto-optic tunable filter. Intensity of the reflected laser light is measured by a silicon photodiode. Incidence angle is varied with a motorized rotation stage with 0.1° at each step. Plasmonic dispersion curve is generated by recording reflection spectrum of the incident light at each 0.1°. [78].

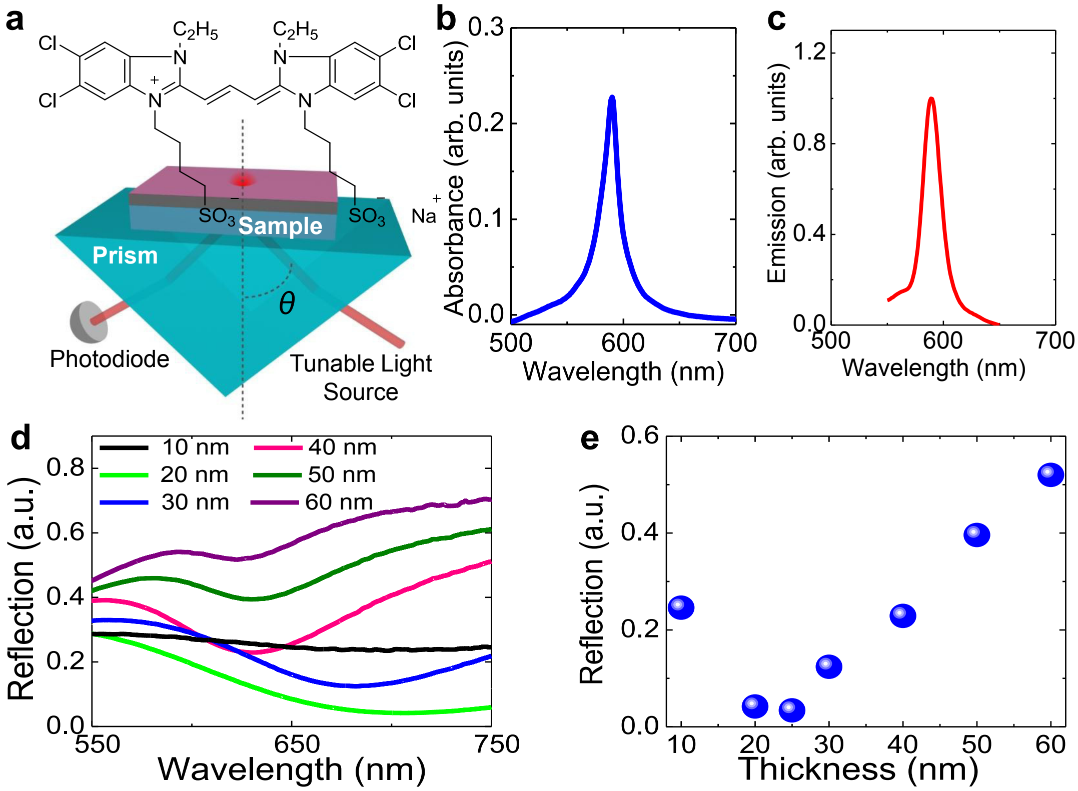

Figure 3.1: Experimental setup, and optical properties of TDBC dye and the hybrid structure. ©2014 OSA

Excitons of a cyanine dye (5,5',6,6'-tetrachloro-di-(4-sulfobutyl) benzimidazolocarbocyanine, TDBC, from Few Chemicals, the chemical structure of a TDBC molecule studied is shown in the inset) is used, forming self-assembled nanostructures at high concentration called J-aggregate, as a matter component because of its strong dipole moment [79] in contact with a thin film of silver supporting surface plasmons. Formation of self-assembled nanostructures of J-aggregate at high concentration can be identified by narrowing and red-shifting of the absorption spectrum. The measured absorption linewidth of excitons, γ_e, is approximately 51 meV and peaked at the exciton resonant energy of 2.09 eV. Polyvinylalcohol (PVA) was dissolved in water by heating the water-PVA suspension at 150 0C for half an hour [59, 79]. TDBC molecules were dissolved in water and then mixed with 1.5% PVA solution in 1:1(v/v) ratio to obtain 0.75% PVA and known concentration of TDBC molecules in water. The solution was then spin coated onto metal evaporated glass substrates to build optical-quality films. Wavelength dependent optical constants (n, k) of TDBC molecules as a function of TDBC concentration in PVA matrix were calculated from the experimental results obtained by ellipsometry. Details of the ellipsometry technique is discussed in Chapter 2. Thicknesses of the prepared films were found to be in the range of between 300 nm and 360 nm. Fig.3.1b and Fig.3.1c show the experimentally obtained optical constants of thin film of TDBC molecules dispersed in PVA polymeric matrix. In this case, TDBC molecules were dissolved in 5% PVA in water and spin coated at 3000 rpm onto a silicon substrate in order to measure optical constants of TDBC molecules in PVA matrix. Both absorption and emission peaks are very narrow and very close to each other; emission peak is only a few nanometers redshifted with respect to the absorption peak.

Plasmon-exciton coupling is monitored through the polarization dependent reflectivity measurements from the silver surface in the Kretschmann configuration (KC) (Fig.3.1a) by varying incidence angle, θ, and recording how the reflectivity of the sample changes with the wavelength of the incident light, which is p-polarized (TM polarized) to excite SPs at the Ag/J-aggregate interface. The samples are mounted on a prism with index matching liquid to maintain the optical index continuity between the prism and the glass substrate [26, 78]. The reflectivity goes to a minimum where the phase matching condition between the incident light and surface plasmon is satisfied (See Fig.3.1d which shows the reflection spectrum of a flat Ag surface through a prism for various thicknesses.) The excitation of a SP on a flat metal surface through a prism can be captured in the reflectivity spectrum with a Lorentzian line shape, $R(\infty) \propto \frac{\gamma_p}{(\omega-\omega_0)^2-\gamma_p^2}$. The damping term, γ_p, determines the linewidth of the reflection spectrum. The linewidth of SP varies, γ_p, from 330 meV to 85 meV as the thickness is changed from 30 nm to 70 nm (Fig.3.1d).

3.2 Strong Coupling and Rabi Splitting

The study of strong coupling regime is done by varying the plasmonic layer thickness and hence the linewidth of the surface plasmon resonance in a controlled manner. Measuring the polarization dependent reflectivity (in KC) of PVA (doped with TDBC) coated Ag surface with various thicknesses, allows one to probe plasmon-exciton coupling. The evolution of plasmon-exciton reflection curves with the thickness of the plasmonic layer is shown in Fig.3.2a. The separation between the polaritonic branches representing the Rabi splitting energy increases with the thickness of the plasmonic layer (Fig.3.2b and Fig.3.2c). As the thickness of plasmonic layer increases, the lifetime of SPs increases indicating that the damping of the plasmonic mode decreases, which results in an increase in surface plasmon-exciton interaction hence large Rabi splitting energies. At around 30 nm Ag film thickness a transition to weak coupling regime is observed. Relative change in the Rabi splitting energy is monitored, and the Rabi splitting energies are calculated from the wavelength versus angle polariton reflection curves. In order to understand why the Rabi splitting energy increases with the plasmonic layer thickness, surface plasmon resonance reflection spectra of bare plasmonic layers are obtained and the linewidth of the surface plasmon resonance reflection spectra are calculated (Fig.3.2d), which indicated a decrease in the linewidth of SP peak with the plasmonic layer thickness.

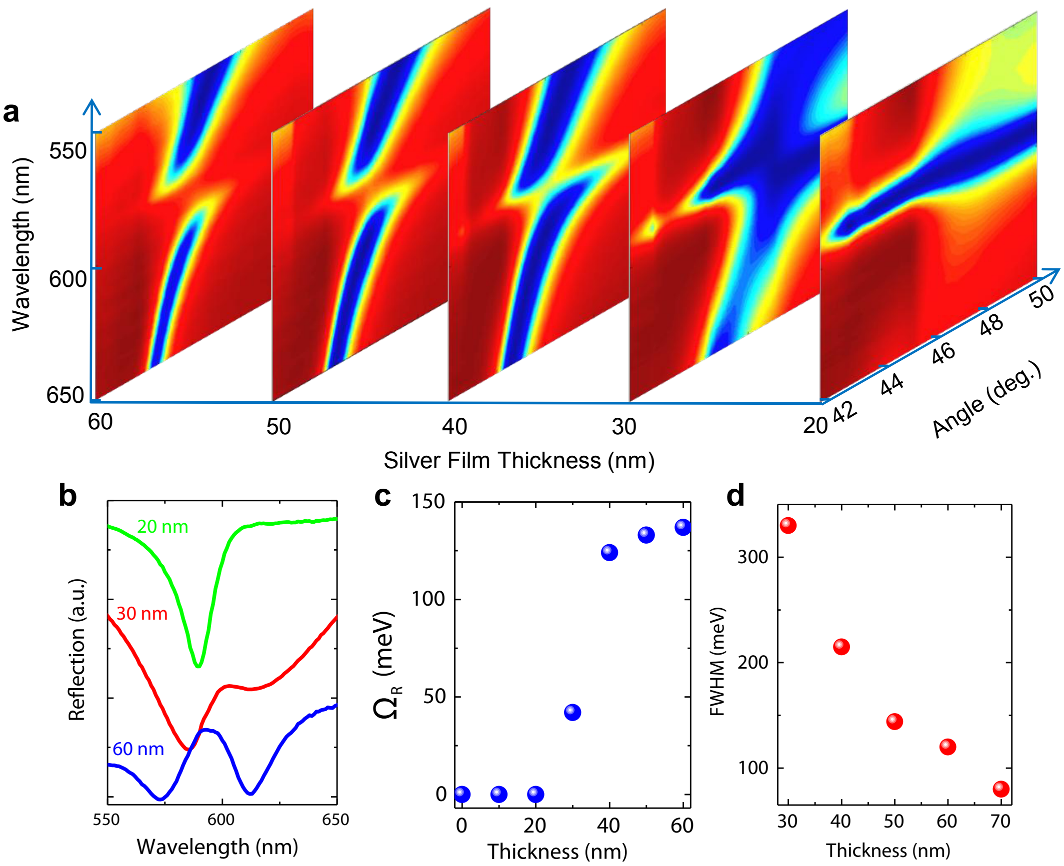

Figure 3.2: Plasmon-exciton coupling as a function of plasmonic layer thickness. ©2012 APS

The dipole moment of TDBC molecules on the silver surface interacts with the electric field of SPs. The coupling energy between the SP and the TDBC molecules is governed by the formula, $E = \boldsymbol{\mu} \cdot \mathbf{E}$, where $\boldsymbol{\mu}$ is the dipole moment of the material, and $\mathbf{E}$ is the electric field generated by the plasmons [32]. Rate of energy transfer between the surface plasmon and the exciton can be expressed as $g = E/\hbar$. At resonance, the two normal modes of the coupled oscillator, in the absence of damping, are given as $s_{\pm} = A\cos(\omega_{ex} \pm g)t$ in which $g = V_0/\hbar$ is the rate of energy transfer and ω_{ex} is the excitonic transition frequency [32]. Given the plasmon mode damping, γ_p, and the exciton damping, γ_e, the two normal modes become damped oscillations in time expressed as

$$S_{\pm} = Ae^{-(\kappa+\gamma)t/2}\cos(\omega_{ex} + g')t \tag{3.2}$$

where

$$g' = \sqrt{\left(\frac{V_0}{\hbar}\right)\frac{1}{4}(\gamma_p - \gamma_e)^2}. \tag{3.3}$$

It is obvious that matching γ_p and γ_e maximizes the coupling and therefore, the Rabi splitting energy [32]. Damping of SPs, γ_p, and damping of the excitons, γ_e, are measured using reflectivity (Fig.3.1b,c) and ellipsometric measurements (Fig.3.1d), respectively. Since the linewidth of the plasmon resonance is proportional to the plasmon mode damping and inversely proportional to the SP lifetime, change in the linewidth affects the energy transfer rate and hence the Rabi splitting energy. Using coupled oscillator model, the energies of the polaritonic branches of the coupled oscillator system can be defined as

$$E_{1,2} = \left[E_{sp}(k) + E_{ex}\right]/2 \pm \frac{1}{2}\sqrt{(\hbar\Omega_R)^2 + (E_{sp}(k) - E_{ex})^2} \tag{3.4}$$

where k is the in plane wave vector, E_1 and E_2 are the energies of the upper and lower polaritonic states, E_{ex} is the energy of the bare excitons, E_{sp} is the energy of noninteracting or bare plasmon mode, $\hbar\Omega_R$ is the Rabi splitting energy ($\hbar\Omega_R = 2V_0$ in which V_0 is the plasmon-exciton interaction energy occurring at the momentum at which energy splitting between the polaritonic states reaches a minimum [32]).

In order to monitor evolution of the polariton reflection curves with the optical density of the TDBC molecules, reflection dips as a function of the light incidence

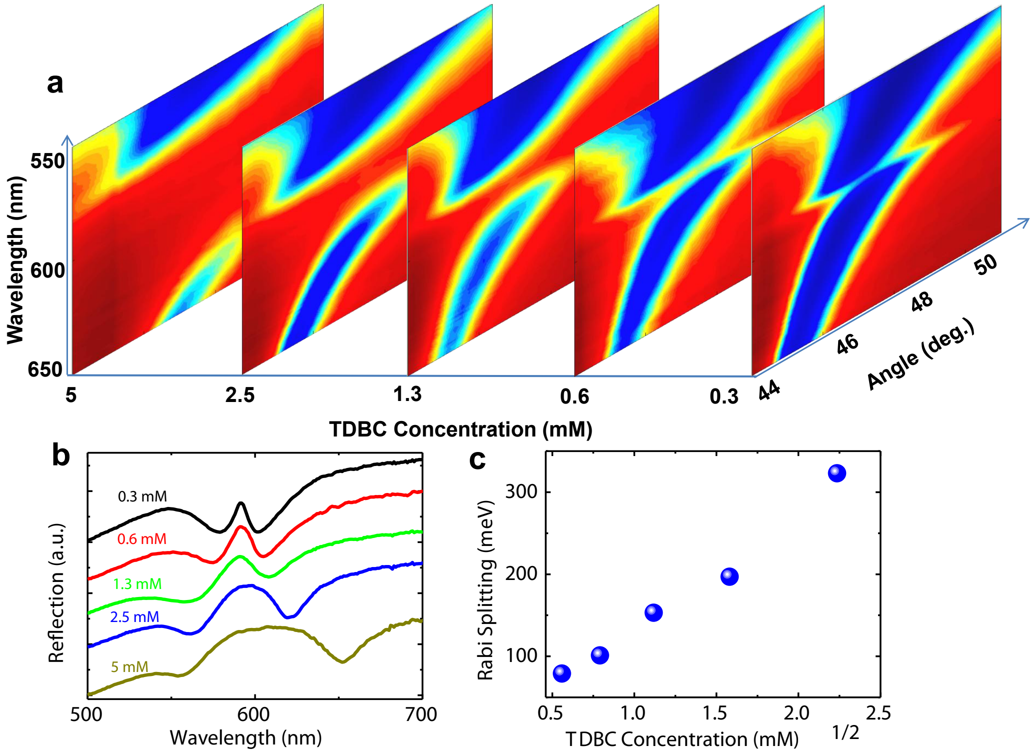

Figure 3.3: Plasmon-Exciton coupling as a function of TDBC concentration. (a) Evolution of polariton reflection curves with varying concentration of TDBC molecules in the PVA matrix. As the concentration of the TDBC molecules increases in the PVA matrix, plasmon-exciton coupling energy or Rabi splitting energy increases. (b) Polariton reflection curves of thin Ag films containing active layer of varying concentration of TDBC molecules in the PVA matrix. (c) Rabi splitting increases linearly with the square root of the TDBC concentration in the PVA matrix. ©2012 APS

angle was acquired (Fig.3.3). At the Rabi splitting angle, where bare exciton and bare plasmon energies overlap, their reflection spectra demonstrate an increase in the separation between the lower and upper polariton branches as a function of J-aggregate concentration. Plotting the square root of TDBC molecule concentration in PVA matrix versus Rabi splitting energy confirms the expected linear dependence [62, 67]. It is obvious that Rabi splitting energy increases linearly with the square root of TDBC concentration [67]. Enhancement of Rabi splitting with the concentration of TDBC molecules is due to the increase in the optical density of J-aggregate film and hence the increase in the total oscillator strength. For a specific absorbing material, Rabi splitting between the plasmonic state and the excitonic state is expected to vary as $\sqrt{\alpha_0 L}$ [62], where α_0 is the peak absorption coefficient and L is the absorbing material film thickness. The data shown in Fig.3.3 represent a clear anti-crossing of the two hybrid peaks, which is characteristic of the strong coupling when the bare SP mode and the bare TDBC exciton resonance mode overlap [68]. The blue and red regions show reflectivity minima and maxima, respectively [26, 78]. It is worth mentioning here that without the TDBC molecules placed on the plasmonic layer, the SP reflection curve does not show any anti-crossing peaks, which are characteristic of surface plasmon-exciton coupling.

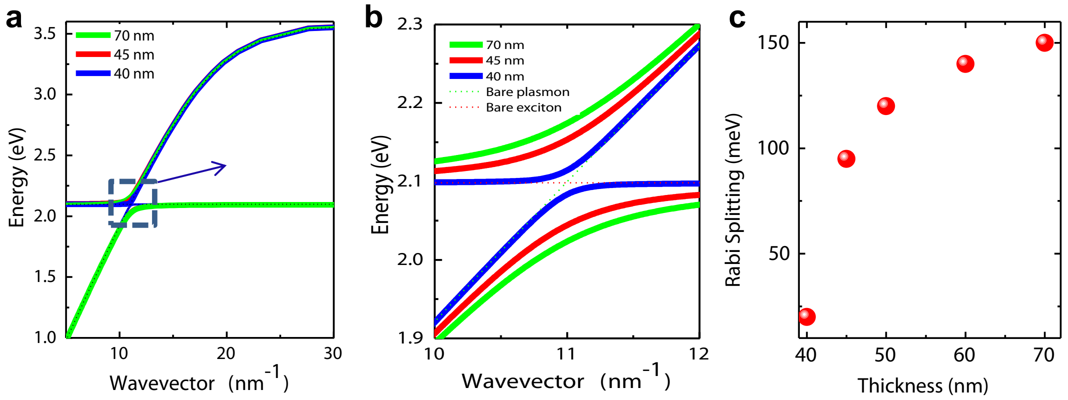

Figure 3.4: Analytically calculated plasmon-exciton coupling. ©2012 APS

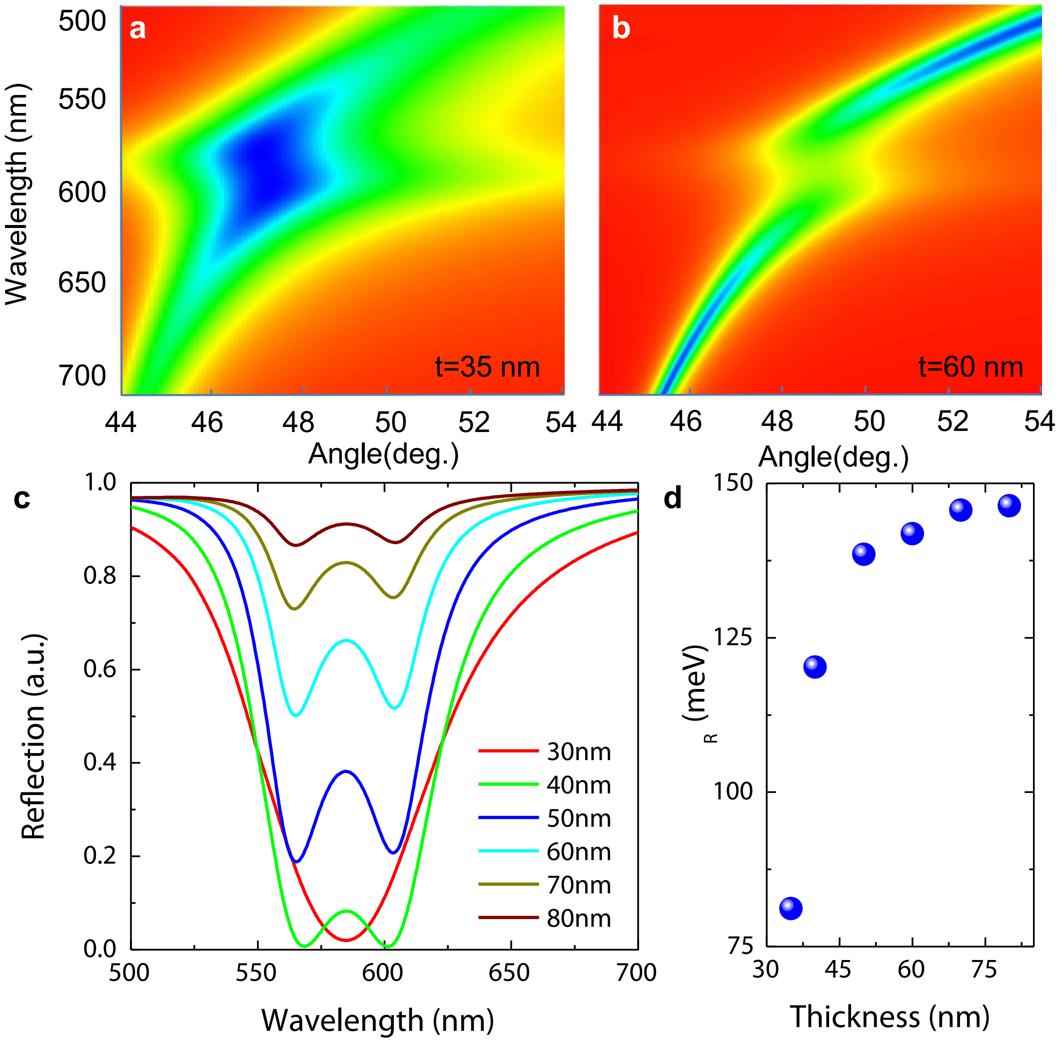

Figure 3.5: Transfer matrix method calculated polariton reflection curves and reflection spectra for varying plasmonic layer thickness. ©2012 APS

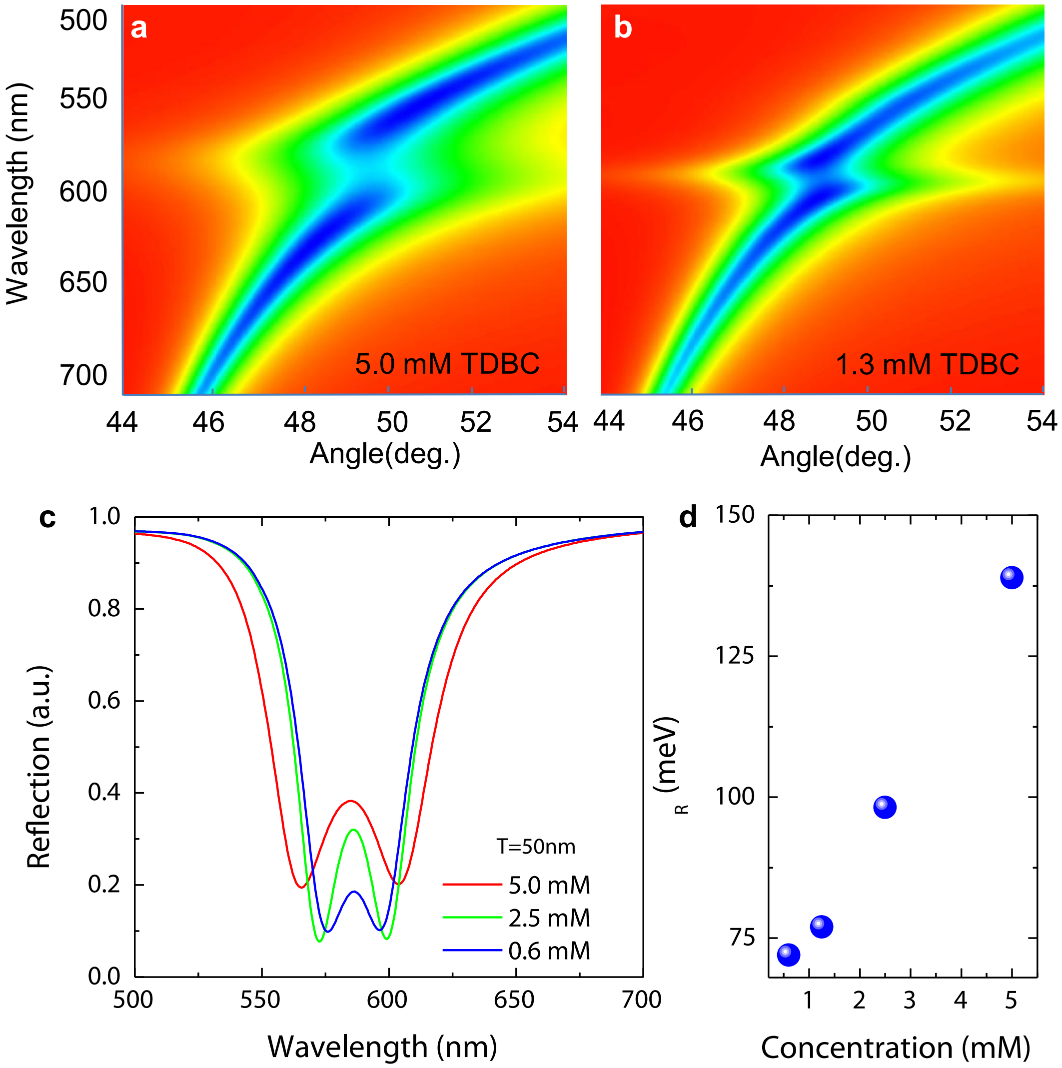

Figure 3.6: Using transfer matrix method, calculated polariton reflection curves and reflection spectra for varying optical density of TDBC molecules and a fixed plasmonic layer thickness. ©2012 APS

3.3 Simulation of Exciton-Plasmon Coupling

Using experimentally obtained optical constants of J-aggregate-polymer layer (Fig.3.1b) and plasmon mode damping for various metal film thicknesses (Fig.3.1c), the polariton dispersion curves of the coupled state were analytically calculated using Eq.(3.4) and presented in Fig.3.4a and Fig.3.4b. Fig.3.4c shows Rabi splitting energies as a function of plasmonic layer thickness. Since, in this case, exciton damping is constant; Rabi splitting can be tuned by only varying the plasmon mode damping. In addition, SP-exciton coupling can be understood within the framework of classical electromagnetic theory. The dispersion relation of SP-exciton system is calculated by solving Maxwells equations for each layer using the transfer matrix method [32, 59, 77]. Such a model with experimentally obtained optical constants of J-aggregate film and plasmonic layer provides a classical explanation of the SP-exciton coupling. Fig.3.5a and Fig.3.5b show the calculated reflectivity maps for J-aggregate film fabricated from a 5 mM TDBC in PVA solution onto 35 nm and 60 nm thick Ag layers, respectively. Optical constants of 5 mM TDBC in PVA were experimentally measured in spectroscopic ellipsometer (Fig.3.1b) and inserted in these calculations. Fig.3.5c shows the reflection spectrum at an angle of 43° for various metal film thicknesses. The small difference between the reflection curves in Fig.3.5c and the experimental reflection curves shown in Fig.3.2b may be due to (i) the small difference between the surface plasmon resonance data in Ref. [80] and the experimental surface plasmon resonance data in this work or (ii) possible small deviations in metal film thicknesses measurements. The calculated Rabi splitting as a function of the metal film thickness is given in Fig.3.5d. The Rabi spitting increases when the thickness of the plasmonic layer increases. The Rabi splitting values we obtain using transfer matrix method are in excellent agreement with the analytical calculations described above in Fig.3.4 and experimental observations shown in Fig.3.4. Furthermore, using transfer matrix method, polariton reflection curves and reflection spectra for varying optical density of TDBC molecules and a fixed plasmonic layer thickness are calculated and shown in Fig.3.6. The calculated polariton reflection curves for 5.0 mM and 1.3 mM TDBC molecules in the PVA matrix are shown in Fig.3.6a and Fig.3.6b, respectively. Polariton reflection curves as a function of the

TDBC concentration on 50 nm thick plasmonic layer clearly shows the increase in Rabi splitting energies with the increase in the TDBC concentration [62, 67]. Fig.3.6c shows the polariton reflection curves as a function of the TDBC concentration on 50 nm thick plasmonic layer and Fig.3.6d shows calculated Rabi splitting energies as a function of the TDBC concentration. The theoretical results shown in Fig.3.4, Fig.3.5, and Fig.3.6 are in excellent agreement with the experimental results demonstrated in Fig.3.2 and Fig.3.3.

3.4 Absorption Enhancement of Excitons Through Weak Coupling

Propagating plasmons on thinner than 30 nm Ag films, in contact with the excitonic medium shows no amount of anticrossing behavior, which directly indicates that they are not strongly coupled to each other. However, in this regime, optical properties of the excitonic medium are still affected with the nearby plasmonic states. While there is no emergence of a hybrid state of plexcitons, there is still a perturbation to the excitonic states which is manifested as absorption enhancement of the excitons.

By performing polarization dependent spectroscopic reflection measurements of J-aggregate nanostructures embedded in the PVA matrix on Ag coated surfaces of various thicknesses in KC, the absorption enhancement of J-aggregates can be probed. Fig.3.7a shows evolution of the polariton reflection curves as a function of Ag film thickness. TDBC concentration (1.3 mM) is kept constant in all the samples. Fig.3.7b displays the reflection curves for each plasmonic layer thickness obtained from the dispersion curves shown in Fig.3.7a at the incidence angle of ∼46°. The resonance at around 590 nm in the reflection curve indicates the absorbance of the self-assembled TDBC molecules. It is clear here that absorption of the J-aggregates is enhanced with the increase in the Ag film thickness, Fig.3.7c. When the plasmonic layer thickness reaches to ∼30 nm, an anticrossing behavior emerges at the energy corresponding to a measured absorption maximum of J-aggregate as a sign of the strong coupling regime. As argued in the previous section, in this regime, new optical modes are formed in the polariton dispersion curve. By increasing the plasmonic layer thickness to higher values, the quality factor of the plasmon resonance increases (Fig.3.1d and Fig.3.1e) or damping of the plasmonic mode decreases and thus the Rabi splitting energy widens in the dispersion curve due to the increase in the coupling strength. At the exciton resonance energy, in the weak coupling regime, plasmonic field is greatly enhanced whereas in the strong coupling regime plasmonic field is strongly quenched.

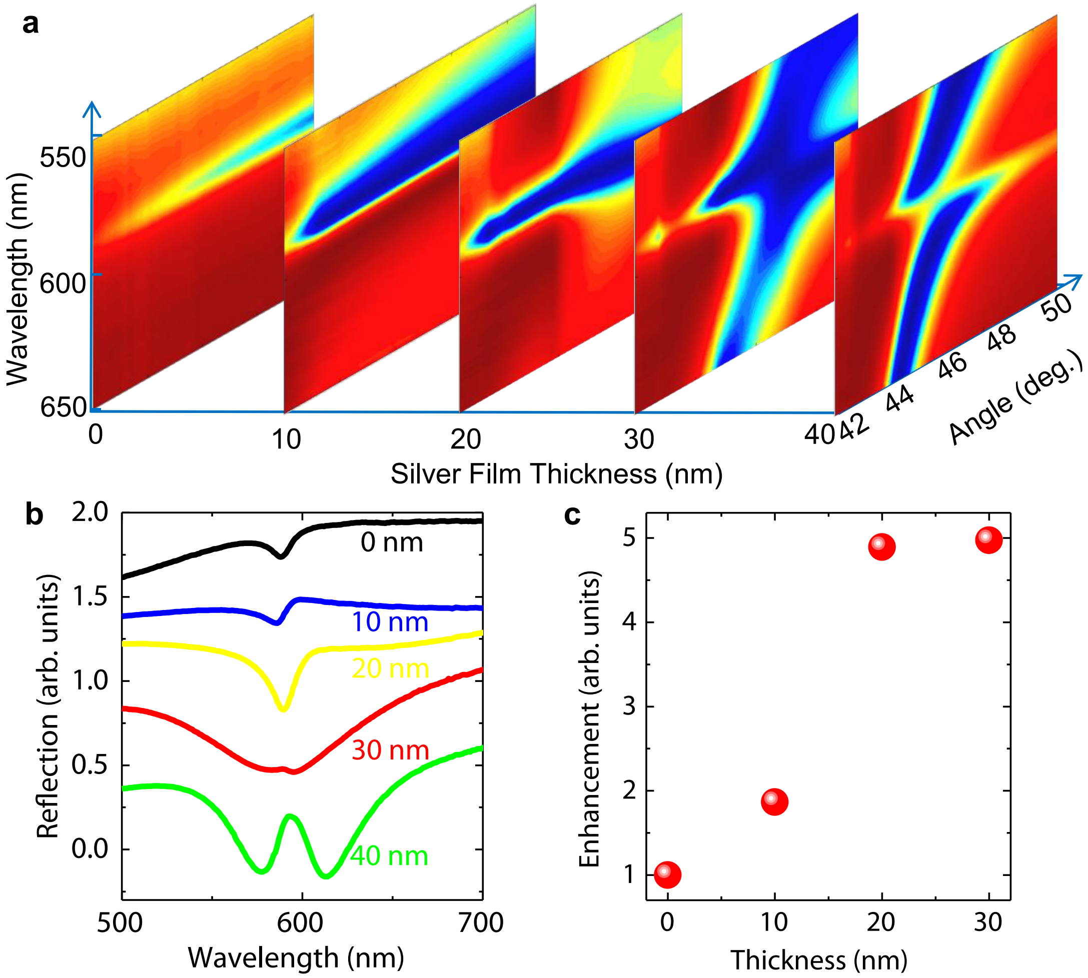

Figure 3.7: Experimental data showing the absorption enhancement of the J-aggregates, operating in the weak plasmon-exciton coupling regime. ©2014 OSA

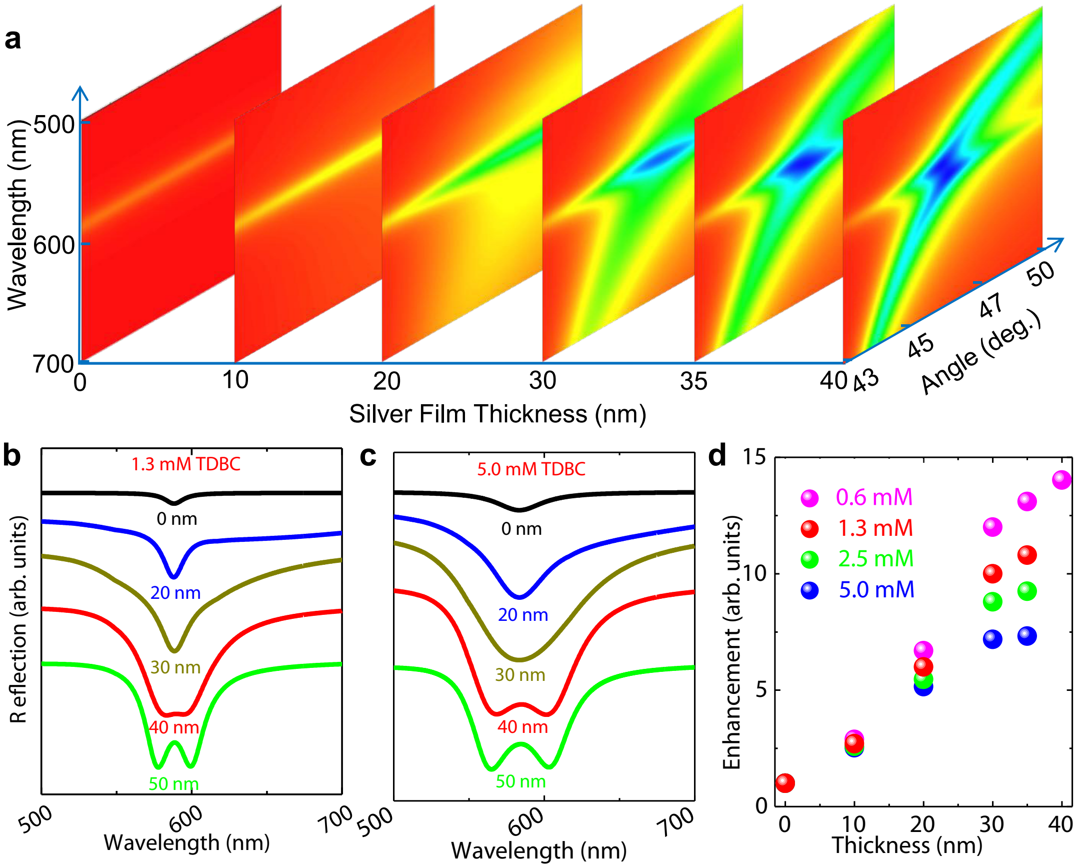

Figure 3.8: Results of transfer matrix method calculations for 1.3 mM TDBC in the PVA matrix and with varying plasmonic layer thickness. ©2014 OSA

Fig.3.8a shows the theoretically calculated reflectivity maps for J-aggregate film fabricated from a 1.3 mM TDBC in PVA solution coated onto the varying thickness of the Ag film. Fig.3.8b shows the reflection spectra for various thicknesses. The enhancement calculated using transfer matrix method for 1.3 mM TDBC is qualitatively in very good agreement with the experimental data shown in Fig.3.7. Furthermore, the effect of the TDBC concentration on the absorption enhancement has been studied. Dispersion curves have been calculated for 0.6 mM, 2.5 mM and 5.0 mM TDBC. Fig.3.8c shows the reflection spectra obtained from the dispersion curve of 5.0 mM TDBC on various metal thicknesses. Absorption of the J-aggregate is enhanced when the plasmonic layer thickness increases (Fig.3.8d). Absorption enhancement of ∼15 times for 0.6 mM TDBC can be observed in the weak plasmon-exciton coupling regime. When the concentration of the TDBC dye in the PVA matrix has been decreased from 5.0 mM to 0.6 mM, it is very clear in the figure that the transition point from weak to strong coupling is shifted from 35 nm to 40 nm Ag film thickness (Fig.3.8d). This is an expected result because, in the strong coupling regime, the coupling energy increases linearly with the square root of the number of dye molecules and, quality factor of the plasmonic mode increases with the commensurate increase in metal film thickness. After decreasing the concentration of the dye molecules from 5 mM to 0.6 mM, to reach the strong coupling level, higher quality factor plasmonic mode (thick Ag film) is needed (Fig.3.1d and Fig.3.1e). Even higher absorption enhancement of the dye molecules could be achieved by decreasing the concentration of the J-aggregate to ∼0.01 mM, the lowest concentration of the TDBC dye in the polymer matrix where J-aggregation can be observed. It is obvious in this case that transition from weak to strong-coupling point (i.e., metal film thickness) will be shifted to the higher metal film thickness values.

The absorption enhancement observed in the weak-coupling regime has been applied in enhancing the absorption of a laser dye, Rhodamine 6G having two separate excitonic broad bands (i.e., weak oscillator strength). Reflection of the incident light from the TDBC molecules is shown in Fig.3.7b where the black and dark yellow curves indicate the reflection from the glass surface containing only TDBC molecules in the PVA matrix and TDBC molecules in a ∼30 nm thick

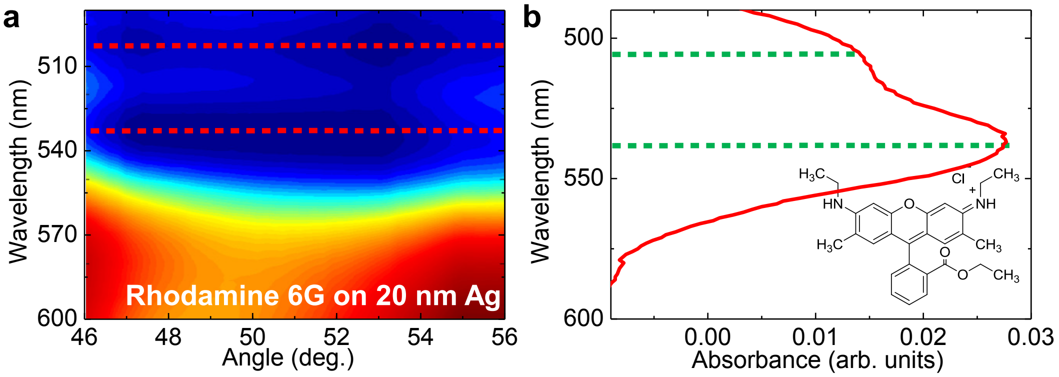

Figure 3.9: Enhancing absorption of Rhodamine 6G molecules. (a) Polariton reflection curve from 20 nm Ag film coated with the Rhodamine 6G molecules in the PVA matrix. (b) Absorption spectrum of the Rhodamine 6G molecules in the PVA matrix. The inset shows the chemical structure of a Rhodamine 6G molecule. The green dotted lines show the position of the exciton transition energy levels in the absorption spectrum of the molecule. ©2014 OSA

PVA film located on a 20 nm thick Ag film. Polariton reflection curve from the sample containing 20 nm Ag film coated with the TDBC molecules in the PVA matrix is demonstrated in Fig.3.7a. The result shows that the absorption of the aggregated TDBC molecules is enhanced and there is no anticrossing - that is, the indication of the weak plasmon-exciton coupling - in the dispersion curve, Fig.3.7a for 20 nm. In a similar way, polariton reflection curve from the sample containing 20 nm Ag film coated with the Rhodamine 6G molecules in the PVA matrix is demonstrated in Fig.3.9a. The dotted red lines indicate the exciton transition energy levels in the Rhodamine 6G molecule. Absorption spectrum of the dye in the PVA matrix is also given (Fig.3.9b). The broad exciton transition energy levels of Rhodamine 6G can be easily located and mapped out in the polariton reflection curve as shown in Fig.3.9a.

In conclusion, the tunability of plasmon-exciton coupling on J-aggregate-metal surfaces is studied experimentally and theoretically. Polarization dependent spectroscopic reflection measurements were used to probe surface plasmon-exciton coupling. In the strong coupling regime, the results demonstrate the formation of plasmon-exciton hybrid states, characterized by large Rabi splitting energies, which can be tuned either by varying the optical density of the TDBC molecules or by varying the damping of the surface plasmon. In the weak plasmon-exciton coupling regime, it is observed that absorption of the dye molecules is greatly enhanced while it is strongly quenched in the strong coupling regime. Transition from weak coupling regime to strong coupling regime has been observed at a critical plasmonic layer thickness.

Transition point from weak regime to strong regime depends on both the number of dye molecules (concentration) present in the polymer matrix and the metal film thickness. The magnitude of the coupling depends on both the exciton oscillator strength and the plasmon mode damping.

Optical constants of thin films of J-aggregated TDBC molecules dispersed in PVA polymeric matrix were measured using a spectroscopic ellipsometer. The broad excitonic bands of the laser dye Rhodamine 6G molecules have been mapped out.

The detailed experimental and theoretical results presented in this study open the way for efficient energy transfer and coherent coupling in plasmonic devices at nanoscale dimensions and it will help in understanding the fundamental aspects of surface plasmon-exciton coupling and designing hybrid plasmonic devices with superior performances. Another demonstration of controlling plasmon loss via temperature [81] or tuning the crystallinity of the plasmonic layer [82] or by optical pumping [81,82] can also be applied to tune plasmon-exciton coupling. The results might further open new detection and analysis techniques of fluorophores used in biochemical and biophysical investigations by enhancing absorption of the fluorophores.

Chapter 4

Plasmonic Band Gap Engineering

Copyright Disclaimer: Contents of this chapter are published in *Optics Letters* as "Plasmonic band gap engineering of plasmonexciton coupling" **Ertugrul Karademir,** Sinan Balci, Coskun Kocabas, Atilla Aydinli, Optics Letters **39**(19), 5697 (2014) and reproduced here with permission of The Optical Society (OSA). Systematic or multiple reproduction or distribution to multiple locations via electronic or other means is prohibited and is subject to penalties under law.

A flat metallic surface allows SPPs to propagate in both forwards and backwards direction. Degeneracy of forward and backward propagating SPP modes at a given frequency can be lifted by patterning the planar surface with a periodic relief structure, such as a sinusoidal uniform grating pattern [83]. Under resonance, this pattern satisfies the conditions of plasmonic band gap formation and slows down [84–86] the SPPs at the two band edges [47, 48, 83]. These band edges are known for decades [12, 87] and have been studied theoretically and experimentally for their dependence on the grating surface profile [47, 83, 84, 87–89], enhancement of Raman scattering [90], availability for signal feedback [91], role on photo luminescence [92], and interactions with excitonic sources [22]. In addition, group velocity of SPPs has been greatly decreased through plasmonic band gap engineering of coupled plasmonic cavities [78].

A model system for investigating light matter interactions is the coupled plasmon-exciton states, which are named plexcitons [32]. Mark of the strong coupling is the observation of Rabi splitting [21, 32, 59, 60, 65, 68, 93] due to the newly emerged in-phase and out-of-phase eigenmodes [32]. The energy difference between these modes is defined as Eq.(3.1) where $V \propto \mathbf{E} \cdot \boldsymbol{\mu}$ defines the energy transfer term between plasmons and excitons [21]. Electric field in the energy transfer term is directly related to the amplitude or the number of plasmonic modes. At the band edges, due to the decreased group velocity and standing wave formation of SPP modes, number of plasmonic modes also increases, causing a further enhancement compared to propagating modes. Recently, plexitonic states have been investigated on a variety of plasmonic structures such as flat metals, spherical nanoparticles, metal disks, metal nanowires, and metal prisms [21, 22, 32, 59, 60, 65, 68, 93]. However, plasmon-exciton coupling has not been studied using plasmonic band gap materials. Studies in this direction might significantly improve the performance of the plasmonic devices and enable understanding the mechanism of the coherent energy transfer between metallic nanostructures and semiconductor nanostructures.

4.1 Experimental

Incident light is coupled to SPPs via prism coupling technique. Sinusoidal gratings have been fabricated using laser interference lithography. Glass substrates (3 mm thick) are first coated with an antireflection coating BARLi (AZ Chemicals) and then with a photosensitive polymer, S 1800-4 (MicroChem). Total thickness of the polymer layer is around 250 nm. The sample is exposed in the lithography set up using the He-Cd laser operating at a wavelength of 325 nm. Finally, a thin film of silver (∼40 nm) is thermally evaporated on the fabricated sinusoidal grating to support propagation of SPPs. Depth of the grating groove is adjusted by only varying the exposure time of the photopolymer. The surface profile and the groove depth of the gratings have been confirmed using atomic force microscope.

A cyanine dye, TDBC, from *Few Chemicals*, forms J-aggregates in aqueous solutions at high concentrations. After dissolving the dye in water, it is mixed with a 1.5% Poly vinyl alcohol (PVA) solution in a 1:1 ratio to prepare 0.75% PVA. At high concentrations, individual dye molecules self-assemble in a head-to-tail fashion to form J-aggregates. J-aggregates have narrower absorption band shifted to the red region of the electromagnetic spectrum with respect to their monomer form. Ultrathin films of 1.25 mM of J-aggregates ($\sim$30 nm) are spin-coated on the metal covered grating structures. SPPs are excited through a triangular BK7 glass prism in the Kretschmann Configuration (KC).

A tunable *p*-polarized monochromatic light source is used to probe the coupling. Reflection spectra are obtained by varying the wavelength of the incoming light and recording the reflected light intensity with a silicon photo-detector at each incidence angle. Finite-difference-time-domain (FDTD) simulations have been performed using *Lumerical FDTD Solutions.* Sinusoidal grating structure of SiO_2 glass substrate covered with a thin layer of silver is uniformly coated with a thin Ag film. Bloch boundary conditions are applied along the lateral direction of the simulation window with one period width in order to simulate the infinite array of repeating patterns forming the plasmonic crystal. Optical constants of the used materials are taken from Palik [94].

J-aggregate dye is modeled as a Lorentz absorber whose resonance frequency is set at absorption line of TDBC dye. Strength of the Lorentz absorber is obtained by fitting the optical parameter data acquired with an ellipsometer [21]. A light source is used for generating white light and a monitor is used for collection of the reflected light. The source and the monitor are positioned inside the glass substrate to mimic the KC. The spectrum obtained from the monitor is normalized with respect to the source. In this way, reflectivity spectra as a function of wavelength for each incidence angle that are similar to the experimental reflectivity spectra are constructed.

Periodic corrugation along the metal dielectric interface introduces a band gap in the dispersion curve of the SPPs. Grating groove depth enables controlling of the E_g manifested in the dispersion curve of the SPPs (Fig.4.1b and Fig.4.1c).

The width of the band gap, E_g, depends on the grating groove depth and increases with it. The narrow absorption band of the aggregated TDBC dye is shown as a red line in the dispersion curve. Since energy of the molecular resonance of the J-aggregate is constant, the E_g can be engineered to study plasmon-exciton interaction on different regions of the band gap. This kind of manipulation of energy levels requires the preparation of plasmonic crystals with varying groove depths.

4.2 Engineering the Band Gap

Interaction between plasmons and excitons is studied through band gap engineering of 1D metallic grating in Γ direction, which has been achieved by varying the groove contrast of the metallic grating in the visible spectrum. This is a simple, yet effective, tool to engineer the band gap of the periodic plasmonic structures, altering the distribution of the plasmonic states. Using this passive tuning approach, one can adjust the distribution of plasmonic states and manipulate the coupling between SPPs and excitons. The plasmonic band gap engineering is schematically summarized in Fig.4.1. Fig.4.1a shows the schematic representation of the experimental setup used for obtaining the reflectivity data recorded as a function of the photon wavelength and the incidence angle. Depth of the grating groove determines the width of the plasmonic band gap energy, E_g. Deeper grooves results in larger E_g. The molecular resonance of the dye remains at the same wavelength while, the E_g of the gratings is varied. Therefore, plasmon-exciton coupling can be studied at different parts (inside and outside) of the band gap. It should be added that spectral position of the band gap can also be altered by varying the periodicity of the grating structure however the periodicity of the grating is fixed for all the gratings studied here. For directions other than the grating direction (Γ direction), 1D grating may not show a band gap. If the crystal is rotated $\pi/2$ degrees with respect to the Γ direction, then the dispersion behavior of the crystal becomes identical to that of the flat metal, because the incident light does not experience a periodic corrugation; in between, the band gap will shift towards blue wavelengths. Hence, the results presented here are for 1D grating along Γ direction and not for a full photonic band gap [95].

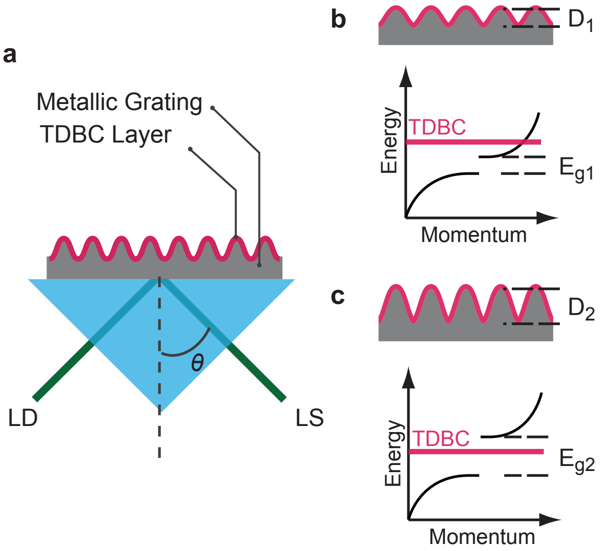

Figure 4.1: Schematic representation of bandgap engineering. ©2014 OSA

4.3 Numerical Modelling

A sample of the resulting reflection map is shown in Fig.4.2a, which is obtained in a simulated KC. Fig.4.2b,c,d are the spatial profiles of electric field intensity averaged over time and recorded for critical regions on the reflection map. White lines mark the boundaries of the metal film. Lower part of the film is SiO_2, and upper part is vacuum. Fig.4.2b,d are the profiles for the upper (grating trough) and lower (grating peaks) band edges, respectively, and Fig.4.2c is the electric field profile inside the band gap region, which doesnt show any field, hence at this configuration interaction between surface plasmons and excitons is expected to be effectively minimized. The separation between high and low frequency components are directly dependent on the groove depth of the grating and are marked as upper and lower band edges in Fig.4.2e. The E_g for shallow grooves (up to 60 nm in depth) has been calculated in Ref. [48] and Ref. [47] with non-Hermitian and Hermitian eigenvalue problems set up with classical Maxwell equations. The calculations have shown that the E_g is approximately linearly proportional to the depth of the grooves.

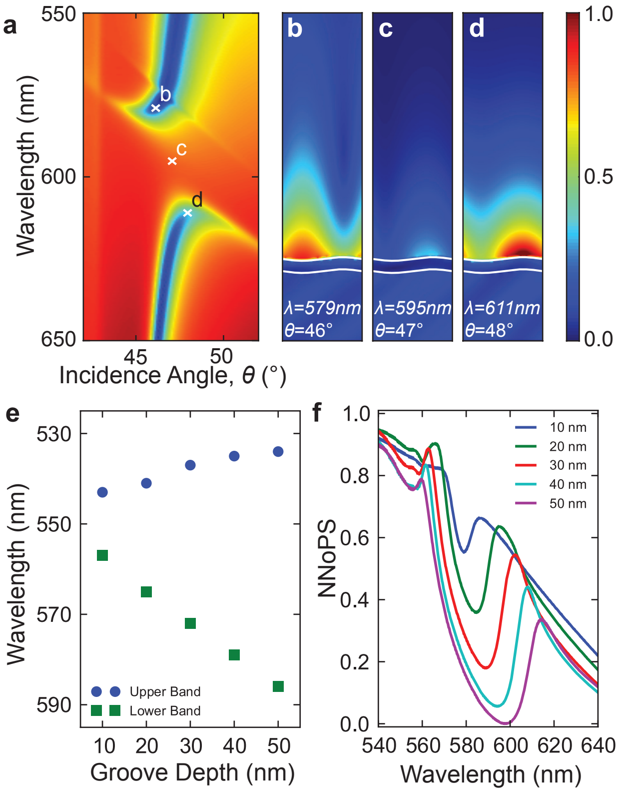

Figure 4.2: Simulation of plasmonic band gap engineering. ©2014 OSA

Normalized number of plasmonic states (NNoPS) is a way to represent distribution of plasmonic states. Energy and the momentum of a plasmonic state can be deducted from the dispersion curve. Experimentally, dispersion curves are recorded with reflectivity measurements. Recording the reflection spectrum at various incidence angles gives the reflection maps. The reflection map exemplified in Fig.4.2a, for instance, can be interpolated to the momentum space by using the relation $k_{SPP} = k_0 n_{\mathrm{PRISM}} \sin\theta$ to obtain the dispersion curve. After interpolation, NNoPS for each wavelength or frequency is calculated with

$$\mathrm{NNoPS}(\omega) = \int_{k_{\mathrm{MIN}}}^{k_{\mathrm{MAX}}} dk[1 - R(\omega, k)]/R_{\mathrm{MAX}} \tag{4.1}$$

where $R(\omega, k)$ is the reflectivity of the incident light for a given frequency and momentum. Both in the experiment and in the simulations, convention is to adjust the momentum of light by varying the incidence angle. k_{MAX} and k_{MIN} are maximum and minimum spatial frequencies that can be obtained using the wavelength and incidence angles. Whenever there is a dip in the dispersion curve, it is an indication of a plasmonic mode. Hence a distribution of plasmonic states can be obtained by subtracting the reflectivity value from unity. Normalization, on the other hand, makes the comparison of different structures more reliable. In Fig.4.2f, normalized distribution of plasmonic states is shown for the bare gratings of varying groove depths with the same periodicity (260 nm). It should be noted that, there are still available plasmonic states inside the band gap. However, increasing the groove depth effectively deepens the minima in NNoPS. This makes effective control of the plasmon exciton coupling possible together with the coupling term introduced in Eq.(3.1). Flat band dispersion at the band edges that are due to the standing wave formation at the grating peaks and troughs can be observed as peaks in NNoPS. Hence NNoPS becomes a reliable tool for plasmonic band gap engineering showing the accumulation of edge states and plasmonic states inside the band gap. Finally, it should be noted that apparent negative group index at the branches (Fig.4.2a) is due to the small fraction of plasmons that are scattered back and propagating in the opposite direction.

4.4 Results

Loading the samples with the J-aggregate layer introduces an anti-crossing at the molecular resonance wavelength (∼590 nm). Band gap has been engineered by varying the grating groove depth from 5 nm to 15 nm. The anti-crossing behavior at the upper branch of the band gap is clearly seen for the grating with the groove depth of 5±2 nm (Fig.4.3a). For the grating with the groove depth of 10±2 nm, lower branch of the anti-crossing is attenuated and diminished further when the grating groove depth is 15±2 nm. This trend can also be observed in the FDTD simulations of the gratings as demonstrated in (Fig.4.3b). There is a qualitative agreement between the simulation results and the experimental results. Because of the discrepancies in such as optical constants and grating profiles used in simulations and actual samples, there is a small difference in the dispersion curve of the coupled system. Upper band edge shifts from 583.4 nm to 584.8 nm and finally to 578.4 nm toward the blue as the groove depth increases from 5 nm to 10 nm and then to 15 nm. Lower band edge shifts from 606.7 nm to 608.6 nm and then to 615.7 nm toward the red. In all cases, j-Aggregate absorption line lies between the band edges, however, there is still considerable amount of SPP modes inside the band gap (Fig.4.2), hence SPP-Exciton interaction is still possible for 5 nm and 10 nm cases. Shifting of upper and lower band edges increases the band gap energy from 81.6 meV to 83.3 meV and finally to 129.9 meV. The increase of E_g is confirmed by simulations. For the grating groove depth of 5 nm, the value of the gap energy is 63.7 meV and increases from 81.3 meV to 125.8 meV when the groove depths are 10 nm and 15 nm, respectively. Anti-crossing in 5 nm and 10 nm cases are 40 meV and 50 meV, respectively.

Attenuation of the lower branch of the anti-crossing is more clearly observed in the NNoPS data presented in (Fig.4.3c) and (Fig.4.3d). Fig.4.3c shows the experimentally obtained data and Fig.4.3d shows the simulation results with the inset showing the NNoPS data of the same system loaded with PVA minus J-aggregate. Anti-crossing is observed as two peaks on both sides of the J-aggregate resonance wavelength marked with a solid line at 590 nm. A peak related to the lower branch of the anti-crossing is located at around 600 nm. As the groove depth varies from 5 nm to 15 nm, this peak attenuates since the number of the available plasmonic states in the band gap region decreases. The peak at around 580 nm belonging to the grating with the groove depth of 15 nm is actually the upper band edge and can also be seen in the inset. On the other hand, the peaks at around 585 nm belonging to gratings with the groove depths of 5 nm and 10 nm are the upper branches of the anti-crossing; they are not present in the case of the bare grating. Near the band edges, where the group velocity of the SPP modes are slowing down, NNoPS values rise, hence the effective amplitude of the electric field increases. Dye molecules have more probability to interact with the SPP modes [21]. Attenuation of the lower branch of the anti-crossing is a clear signal showing effectively suppression of the plasmon-exciton coupling inside the band gap region.

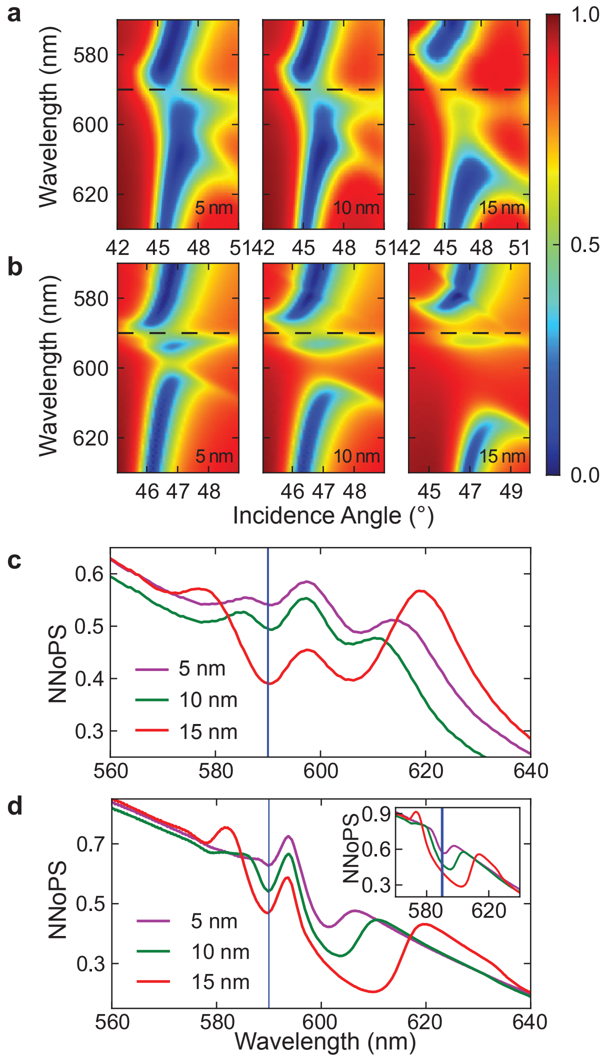

Figure 4.3: (a) Experimentally obtained reflection maps for gratings with 280 nm pitch. J-aggregate molecular resonance is marked with a dashed line at around 590 nm. ©2014 OSA

In conclusion, control of plasmon-exciton coupling by engineering the band gap of the plasmonic crystal is demonstrated experimentally and theoretically. This leads to the observation that coupling is suppressed when the molecular resonance energy level is inside the band gap region along Γ direction and it is observed outside the band gap region, hence a directional suppression of SPP-exciton interaction is achieved. Molecular resonance of the J-aggregate dye has been kept constant during all the experiments while the E_g has been effectively controlled by the grating groove depth. This approach allows the study of plasmon-exciton coupling at different regions of the band gap. The strength of the coupling inside and outside of the band gap has been measured through the strength of Rabi splitting. The results indicate that the strength of the coupling between plasmons and excitons can be effectively controlled by plasmonic band gap engineering and therefore the coupled system can be used in plasmonic devices and in understanding light-matter interaction on plasmonic crystals.

Chapter 5

Directionality of Plasmon-Exciton Coupling: Plexcitonic Crystals

Copyright Disclaimer: Contents of this chapter are published in *Optics Express* as "Plexcitonic crystals: a tunable platform for light-matter interactions" **Ertugrul Karademir,** Sinan Balci, Coskun Kocabas, Atilla Aydinli, Optics Express **22**(18), 21912 (2014) and reproduced here with permission of The Optical Society (OSA). Systematic or multiple reproduction or distribution to multiple locations via electronic or other means is prohibited and is subject to penalties under law.

Plexcitonics is an emerging field that involves light-matter interaction in nanometer scale. Its namesake particles, plexcitons, are defined as coupled plasmon-exciton pairs [22]. Plexcitons are useful in nanophotonics and quantum optics applications [32, 68, 96–98]. A plexcitonic crystal [25] is a platform that shows variable plasmon-exciton coupling characteristics depending on the direction of plasmon excitation.

If two harmonic oscillators are coupled, they exchange energy between modes. Their coupling can be weak or strong. When two oscillators are weakly coupled, one's effect on the other is a small perturbation; if two are strongly coupled, new eigenstates emerge. Anti-crossing is observed in several coupled oscillators, such as quantum dots in photonic crystals [99], sound waves coupled to tranducers [100], microwave photons coupled to superconductor circuits [101]. In plasmon-exciton coupling case, a finger print of the strong coupling is manifestation of anti-crossing in SPP dispersion curve [21]. Coupling strength or separation of anti-crossing is controlled with modification of intrinsic properties of plexcitons. One such property is their lifetime [21, 67, 70, 102–104]. In this chapter, one and two dimensional plexcitonic crystals and their directional properties will be presented.

5.1 Simulation

For simulations, Finite Difference Time Domain (FDTD) method is employed. Grating period is set to be either 260 nm or 280 nm. If the crystal is a two dimensional crystal, the pitch is the same for both dimensions. Grating depth is fixed at 40 nm. For each crystal, one unit cell of the grating is confined inside Bloch boundaries in lateral dimensions (x and y). In the stacking direction (z), a SiO_2 substrate coated with a 40 nm Ag film is used and in this direction perfectly matching layers (PML) are used for boundaries. Optical parameters of both materials are taken from Palik [94]. For each incidence angle, reflection maps are recorded by sending white light from the substrate to the silver film, then collecting the reflection by a power monitor. Results are then corrected for the momenta of different wavelengths of light at each incidence angle. Azimuthal angle is defined by the phi parameter ($y = 0$ plane being $\phi = 0°$) of the light source whereas incidence angle is defined by theta parameter (z+ axis being $\theta°$), polarization angle is adjusted so that the electric field is in the plane of incidence. In order to introduce the J-aggregate film into the calculations, we have used a Lorentz absorber model with base permittivity matching that of the PVA film ($\epsilon = 2.22$, $n = 1.49$). Line-width of the oscillator is set 8.1e±12 rad/s with resonance frequency of 3.19263×10^{15} rad/s ($\lambda = 590$ nm). Oscillator strength is tuned to match the splitting that is recorded in the experiments. The software package uses a custom, adaptive, non-linear meshing algorithm. Density of the mesh grid is parametrized with a mesh accuracy parameter. We have set this parameter to 3 which sets 14 mesh points per effective wavelength and added a further refinement to set the maximum mesh step in every direction as 5 nm. Convergence tests showed that further refinement does not change the results but costs additional computation time.

5.2 Experimental

Experiments have been done with a variable angle ellipsometer that can control the wavelength of the incidence light within 0.1 nm variation and the incidence angle within 0.01°. Samples are mounted on a BK7 half sphere with index matching fluid that has identical optical parameters as BK7 glass. In order to change the azimuthal orientation, we simply rotated the half sphere. For each wavelength and incidence angle, we have recorded the reflectivity of the sample from the prism side.

Samples are prepared by following the methods explained in Chapter 2.1. One dimensional crystal samples have been obtained with single exposure, whereas two dimensional crystals are obtained with two exposures, where the second exposure is applied after rotating the sample. Rotation angle of the second exposure is determined by the intended symmetry of the crystal. Square lattice is obtained by 90° rotation of the sample with respect to the first exposure, hexagonal crystal is obtained by 60° rotation. In all exposures, pitch of the grating is set to yield either 260 nm or 280 nm. Exposure time determines the depth of the grating. Resulting grating depth is characterized with an atomic force microscope.

TDBC (5,5’, 6,6’-tetrachloro-di-(4-sulfobutyl) benzimidazole-carbocyanine) dye is used as J-aggregate, which has its absorption peak at 590 nm wavelength. TDBC is dissolved in poly vinyl alcohol (PVA) polymer, which is water soluble and suitable for proper thin film fabrication of aggregated TDBC dye. Dye embedded polymer layer is then spin coated on the silver plated sample. Concentration of TDBC is set 2 mM in 0.75% PVA.

5.3 One Dimensional Plexcitonic Crystals

Plexcitonic crystals provide a continuous and reversible tuning of plexciton coupling strength. The method relies on the directional dependence of plasmonic band gap center. In Fig.5.1a and Fig.5.1b schematic representation of 1D plexitonic crystals and the surface plasmons propagating in directions with the azimuthal angle, θ are shown. For a metallic one dimensional grating, the plasmonic band gap is introduced at the point where wave vector of SPP intersects with the Brillouin zone boundary,$k_{SPP} = \frac{\pi}{\Lambda \cos\theta}$, where Λ is the period of the grating and θ is the azimuthal rotation. The effective periodicity, $\Lambda \cos\theta$, decreases as the azimuthal rotation is increased. Fig.5.1c shows simulated reflection maps of a sinusoidal metallic grating (280 nm pitch) pattern without the excitonic load for three different azimuthal angles, whereas Fig. 1d shows simulated reflection maps with excitonic load for azimuthal angles of 0°, 30° and 90°, respectively. If the azimuthal rotation is 90°, effective periodicity limits to 0, or the grating effectively becomes a flat metal , which is expected, because the surface does not have a modulation along this direction. Loading the surface with an excitonic source, like TDBC dye whose absorption peak is at 590 nm, we see anticrossing behavior at the absorption line of the dye.

Anti crossing behavior is better seen in Fig.5.1f, where reflection spectra at different azimuthal angles are presented. The simulated grating has its band gap center at around 590 nm when the grating is oriented at 0° azimuthal angle. At this angle, absorption line is completely inside the SPP forbidden zone. Hence, we only see a small absorption dip of the dye. As we rotate the grating, the band gap center shift towards blue wavelengths. At 30° azimuth angle, anticsrossing is more apparent. Increasing the azimuth angle to 90°, results in complete disappearance of the band gap. Detailed tomography of the directional behavior can be understood by a directional map, as presented in Fig.5.1e, where polar plot shows the variation of the upper energy branch (green dots), lower energy branch (blue dots), and exciton energy (purple line) as a function of the propagation direction. Since the absorption of the dye molecules is direction independent, it

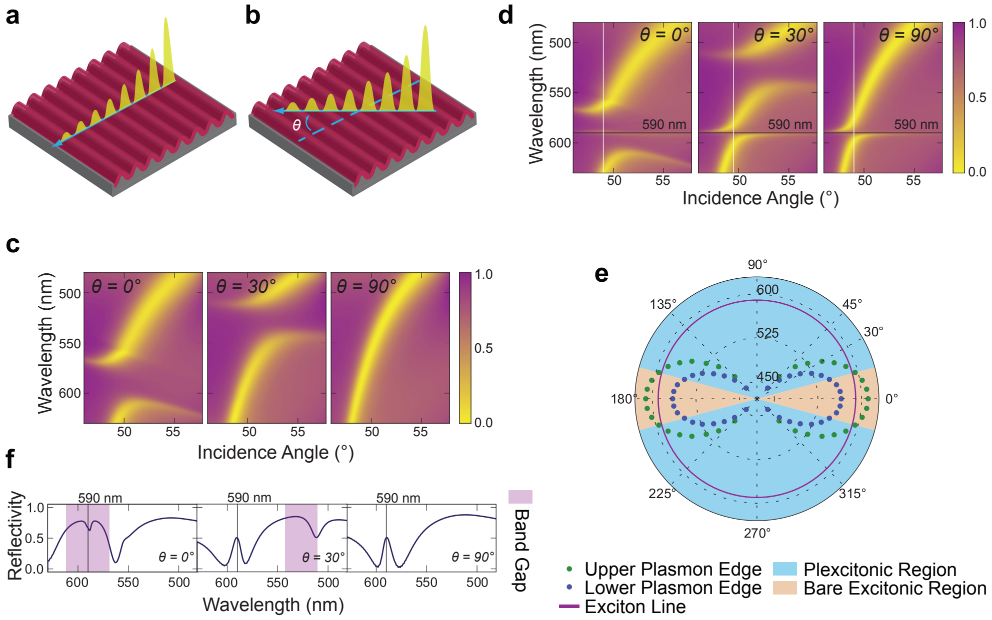

Figure 5.1: 1D plexcitonic crystal. ©2014 OSA

is manifested as a circle. However, band edges of the one dimensional plexcitonic crystal shows a dipole like directional dependence, resembling the far field projection of dipole nano antennas.

Fig.5.2 shows the experimental demonstration of one dimensional plexcitonic crystal with 280 nm pitch. At 0° azimuth angle, band gap of the crystal is at around 670 nm. As the crystal is rotated, we see perfect match of the band gap and the absorption state of the TDBC dye at 32.5° azimuth. At 45° azimuth, band gap is shifted to 530 nm wavelength (Fig.5.2a). At 90° azimuth it completely disappears (data not shown). At 32.5° azimuth angle, SPP-TDBC interaction is forced to weak coupling. SPP-TDBC interaction is more visible in reflection spectra (Fig.5.2c). At 32.5° anticrossing at 590 nm is completely inside the band gap. Dipole antenna like rotational behavior is also apparent in Fig.5.2b. Fig.5.2c shows the reflection spectra for different azimuth angles, where shift of the bad gap is more clear and the anticrossing is also seen.

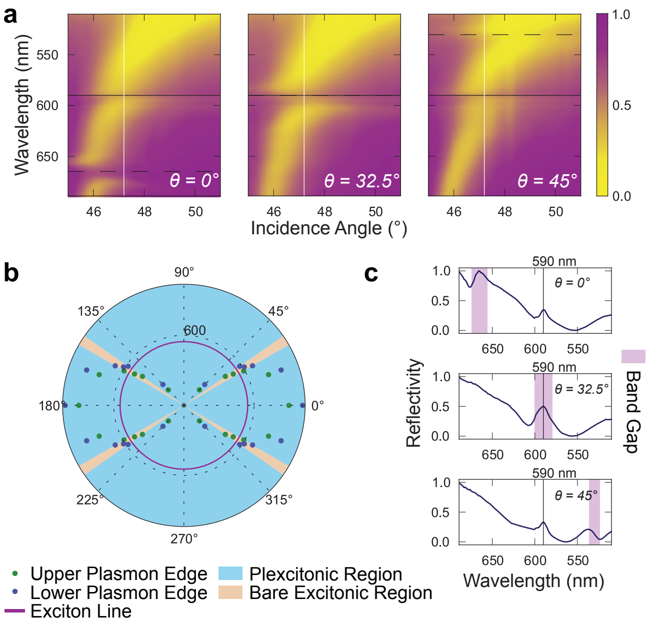

Figure 5.2: Experimental demonstration of a one dimensional plexcitonic crystal. ©2014 OSA

5.4 Two Dimensional Plexcitonic Crystals

Adding another periodic corrugation along a different direction to the first one results in the two dimensional crystal pattern. Here, the direction of the second periodic pattern determines the rotational symmetry of the crystal. Two types of lattice symmetries are tested, square and triangular. A square lattice is obtained when the second grating is rotated 90° with respect to the first one, whereas triangular lattice is formed when the rotation is 60°. The square lattice has four-fold rotational symmetry and the the triangular lattice has six-fold rotational symmetry.

In Fig.5.3a, SEM micrograph of the square lattice obtained by super position of two 280 nm pitched gratings is presented, overlayed with a theoretical model. A complete correspondence with the numerical model is presented in the inset together with the unit vectors that build up the crystal. Grating pitch in both directions is 280 nm whereas depth of the grating is 41 nm ±2 nm. Fig.5.3b shows the rotational diagram of the metallic lattice without excitonic load. It is a clear

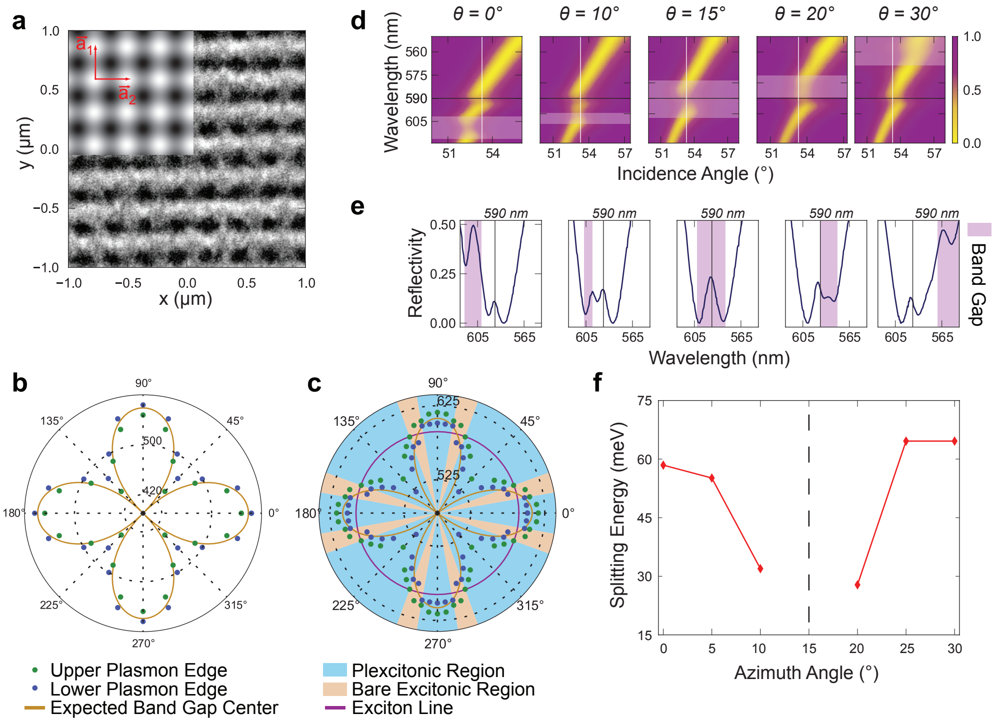

Figure 5.3: 2D plexcitonic crystal with square lattice symmetry. ©2014 OSA

combination of two one dimensional lattices, one rotated 90° with respect to the other. Band gap shifts from 540 nm to 430 nm (500 meV shift) as we rotate the sample from 0° to 45° azimuth. Then, it shifts back to 540 nm as we continue to rotate the sample to 90°, and repeats this pattern for each 90° rotation. After the excitonic film is loaded on the sample, all band gaps shift to red (Fig.5.3c). SPP-TDBC interaction is summarized in Fig.5.3d. At 15° azimuth, absorption of TDBC dye is completely inside the band gap. at 10° and 20° azimuth, SPP-TDBC interaction is weakened which results in smaller anti crossing. Fig.5.3e shows reflection spectra along several different azimuth angles marked in Fig.5.3d. At 0° and 30° azimuth angles, a strong anti-crossing behavior is observed. Starting from 10° azimuth angle, coupling of SPPs and excitons weakens resulting in appearance of completely bare excitons at 15° azimuth angle. At 20° azimuth angle, we see the interaction regaining strength and at 30° azimuth interaction strength is completely recovered. Fig.5.3f Rabi splitting energy as a function of azimuthal rotation is presented. At 10° and 20°, splitting energy is nearly halved and recovered. The decoupling behaviour manifests uncoupled bare excitonic regions in the far-field as can be seen in Fig.5.3c. Width of the bare excitonic regions strongly depends on the depth of the gratings, because SPP band gap separation increases with the depth [24].

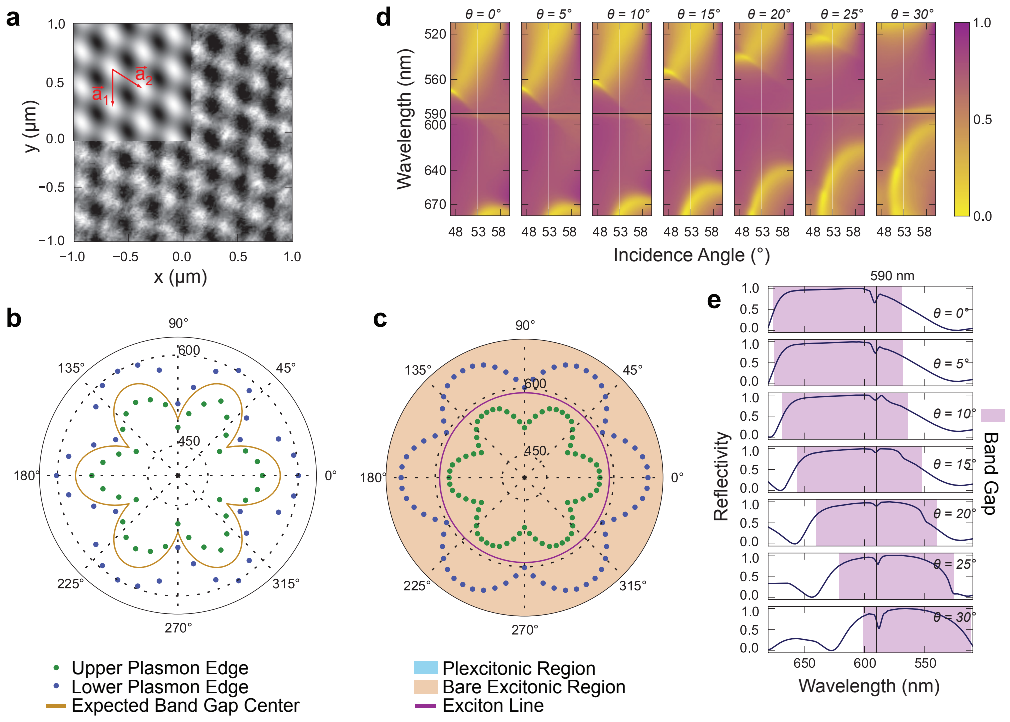

Figure 5.4: 2D plexcitonic crystal with triangular lattice symmetry. ©2014 OSA

In Fig.5.4a, SEM micrograph of a triangular lattice is shown. This 2D plexcitonic crystal is obtained with two super-imposed 1D crystals rotated 60° with respect to each other. Rotational map of this lattice gives a hexagonal symmetry (Fig.5.4b) which repeats itself for each 60°s. Grating pitch is 280 nm in both directions whereas grating depth is 60 nm ±2nm. However, band gap shift due to azimuthal rotation is 300 meV (from 570 nm to 500 nm). Here, one thing to notice is that the hexagonal symmetry is the closest symmetry one can get to circular symmetry. So, tuning the grating depth, one can confine the absorption line completely inside the band gap in every direction, as it is simulated in Fig.5.4c. For the simulations, grating pitch is set 280 nm with depth of 80 nm in order to fully enclose the exciton line. As it can be seen in Fig.5.4d and Fig.5.4e, when the band edges are near to the absorption line, we see an increased absorption, compared to other directions, even though absorption line is still inside the band gap. This is due to the fact that, inside the band gap, there still are plasmonic modes, since number of plasmonic states does not drop to zero once the band edge is reached.[17]. This point is covered in Chapter 4.

In conclusion, plexcitonic crystals show directional SPP-Exciton coupling dependence, with rotational and translational symmetries. These crystals are obtained with simple holographic lithography method. Although only square and triangular lattice have been shown, one can vary the symmetry of the crystal by varying the rotation angle at the second exposure. Also adding another exposure in a different angle can result in quasi-periodic crystals [105–107] with richer geometry. The geometric dependence can be exploited to reversibly tune the SPP-Exciton coupling strength. We propose that a metallic Moiré cavity can be used to enhance and amplify plasmon-exciton interaction with the slow plasmon mode inside the cavity. This new platform will be useful in future SPP-matter interaction research.

Chapter 6

Moiré Cavities for Plasmonic Amplification

The ultimate goal of this thesis is to achieve amplification of plasmon-exciton interaction. Classically, this requires feedback through a cavity. Moiré cavities can provide feedback to achieve lasing.

In this chapter, we characterize Moiré caivties by dark field imaging of localized surface plasmon polaritons (SPPs) in plasmonic waveguiding bands formed by plasmonic coupled cavities is presented. The light scattered from SPPs in the plasmonic cavities excited by a tunable light source is imaged. Tuning the excitation wavelength, the localization and dispersion of the plasmonic cavity mode is measured. Dark field imaging has been achieved in the Kretschmann configuration using a supercontinuum white light laser equipped with an acoustooptic tunable filter. Polarization dependent spectroscopic reflection and dark field imaging measurements are correlated and found to be in agreement with finite-difference time-domain (FDTD) simulations.

Imaging of surface plasmon polaritons (SPPs), coupled electromagnetic field-charge density oscillation at a metal-dielectric interface, has attracted great interest in recent years due to the possibility of obtaining subwavelength plasmonic optics [42,108–116]. Plasmonic imaging with subwavelength resolution is another interesting application of plasmonics.

The SPP waves around the metallic nanostructures can be imaged, for example, using a scanning near field optical microscope (SNOM) or a photon scanning tunneling microscope (PSTM) by raster scanning the sharpened fiber tip in the near field over a metallic surface to obtain an optical image with subwavelength resolution [108–111]. In this way, plasmonic properties of individual metallic nanoparticles has been measured different from the nanoparticle ensemble. Using PSTM, P. Dawson et al. have shown the first direct imaging of propagating SPP waves and directly calculated the propagation length of SPPs [108]. PSTM imaging of sampled Bragg mirrors containing coupled SPP cavities has been also achieved [109]. However, SNOM or PSTM imaging entail significant experimental effort and the interaction between the sample and the tip may affect the experimental results.

An alternative way of imaging SPPs is using total internal reflection or dark field microscopy [112–116]. Different from conventional bright field optical microscopy; dark field imaging involves suppression of specular reflection and detection of the scattered light from the sample. Performing dark field imaging of nanowires and nanoparticles, C. Sönnichsen et al. have determined the plasmon resonance of individual gold nanoparticles [114]. Moreover, using dark field imaging of SPP waves, it has been shown that a drastic reduction of the plasmon dephasing rate in metallic nanowires occurs when compared with small metallic nanoparticles [114]. In contrast with previous studies, here, dark field microscopy is used to directly image localized SPPs in plasmonic coupled cavities [46,73,78,86,117–119].

Here, spectroscopic reflection and dark field imaging measurements are correlated to shed light on the spatial distribution of SPPs in the cavity region. By tuning the coupling coefficient between the cavities the group velocity and dispersion of SPPs are controlled. By directly imaging SPP waves in the cavity region, it is shown that as the coupling coefficient between the cavities goes to zero localization of SPPs increases.

6.1 Moiré Cavities

Moiré patterns are infamous phenomena that occur when two periodic patterns are crossed each other. It is basically an aliasing artefact due to the superposition of two repetitive patterns that are slightly different in spatial or temporal frequency. In acoustics, Moiré pattern is also called a beat pattern. In plasmonics Moiré cavities have been introduced for confinement of surface plasmons in the propagation direction with Kretschmann setup [16] [86]. Formation of this pattern is summarized in Fig.6.1 (also see Fig.7.2b). Using holography, the Moiré cavity is obtained by sequentially exposing the photoresist coated sample twice, while slightly changing the incidence angle after each exposure.

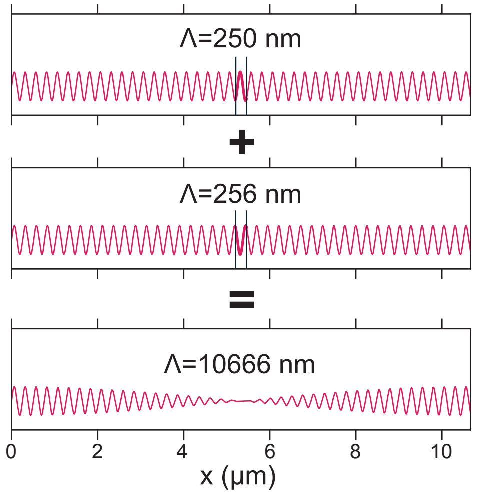

Figure 6.1: Formation of Moiré pattern.

Two superposed gratings result in two periodicities. One is a fast modulating scattering period and the other is a slow modulating envelope period. Envelope period determines the confinement of the cavity mode [120]. One can calculate envelope and scattering periods with simple trigonometric identities. Basically, we are superposing two sine functions,

$$\sin(2\pi x/\lambda_1) + \sin(2\pi x/\lambda_2) = 2\sin\left[\pi x\left(\frac{1}{\lambda_1} + \frac{1}{\lambda_2}\right)\right]\cos\left[\pi x\left(\frac{1}{\lambda_1} - \frac{1}{\lambda_2}\right)\right]$$

where λ_1 and λ_2 are periods of the two superposed gratings. Here,

$$\left(\frac{1}{\lambda_1} + \frac{1}{\lambda_2}\right) = \frac{\lambda_1 + \lambda_2}{\lambda_1\lambda_2} = \frac{2}{\lambda} \tag{6.1}$$

determines the fast varying scattering periodicity and

$$\left(\frac{1}{\lambda_1} - \frac{1}{\lambda_2}\right) = \frac{|\lambda_1 - \lambda_2|}{\lambda_1\lambda_2} = \frac{2}{\Lambda} \tag{6.2}$$

determines the slow varying envelope periodicity. One thing to note is that at the position Λ, there is 180° phase rotation, however, the cavity state is confined for every $\Lambda/2$; hence cavity length is often taken as $\Lambda/2$ instead of the full period. The Moiré cavity obtained by super position of two uniform gratings with pitches of 250 nm and 256 nm is hereafter referred to as Moiré 250+256 nm.

6.2 Experimental

Fabrication of plasmonic cavities on Moiré surfaces has been achieved using a holographic technique called laser interference lithography (IL) details of which is discussed in Chapter 2. Fig.6.2a and Fig.6.2b show scanning electron microscope (SEM) and atomic force microscope (AFM) images of one dimensional SPP cavities, respectively. The micrograph in Fig.6.2a shows an array of coupled cavities whereas the one in Fig.6.2b shows a single cavity. It is obvious that amplitude of the Moiré surface approaches zero in the vicinity of the nodes where the cavity is located. In reflection measurements, the depth of the grating has to be properly adjusted to observe the dispersion of SPPs since the dispersion of SPPs strongly depends on the grating groove depth [78]. In order to tune the groove depth, exposure time of the photopolymer is varied. A thin layer of Ag film (∼35 nm) was evaporated on the patterned surface to support the propagation of SPPs. Kretschmann configuration was established by attaching the glass sample onto a prism using index matching fluid.

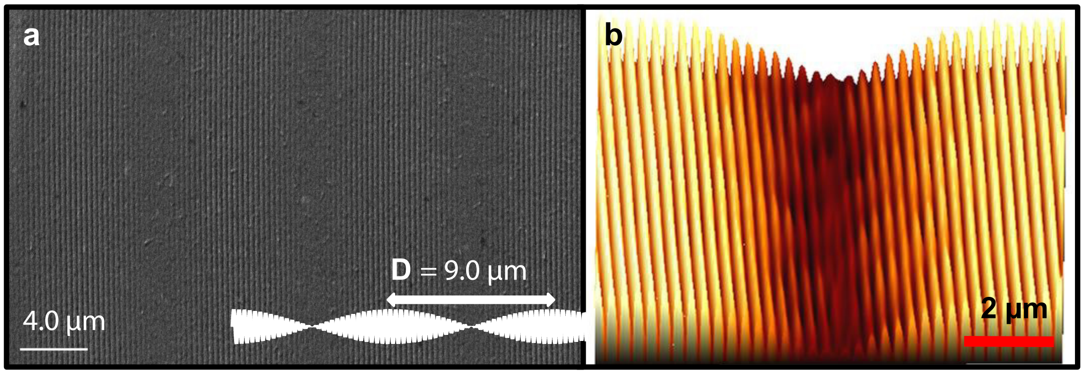

Figure 6.2: (a) SEM image of 9.0 μm long plasmonic coupled cavities. Three coupled cavities can be observed in the image. (b) AFM image of a single cavity. The cavity is located where the amplitude of the Moiré surface approaches zero. ©2011 OSA

Reflectivity measurements were performed by varying the incidence angle and monitoring the reflected light as a function of wavelength using a spectroscopic ellipsometer [46, 73, 78, 86]. Dark field plasmon microscopy (DFPM) imaging was performed using a supercontinuum white light laser as an excitation source (Fig.6.3) [112–116]. The supercontinuum light source is a spatially coherent broad band source (500 nm-1800 nm) with very high spectral power density (2.5 μW at 615 nm during imaging). An acousto optic tunable filter (AOTF) can select the desired wavelength from the broad range of available wavelengths. The excitation light is introduced into the sample at an incidence angle larger than the critical angle, which prevents the exciting light from entering the detection optics.

Scanning along the vertical axis of the dispersion curve, SPP cavity modes are excited when the incident light is in resonance with the mode. The SPP field confined to the cavity region is scattered to the far field by the rough metal surface of a few nanometers [119, 121]. The scattered SPPs from the cavity mode can be imaged using DFPM giving spatial distribution of SPP waves in the cavity region. A 40× objective is used to collect the light scattered to the far field. The

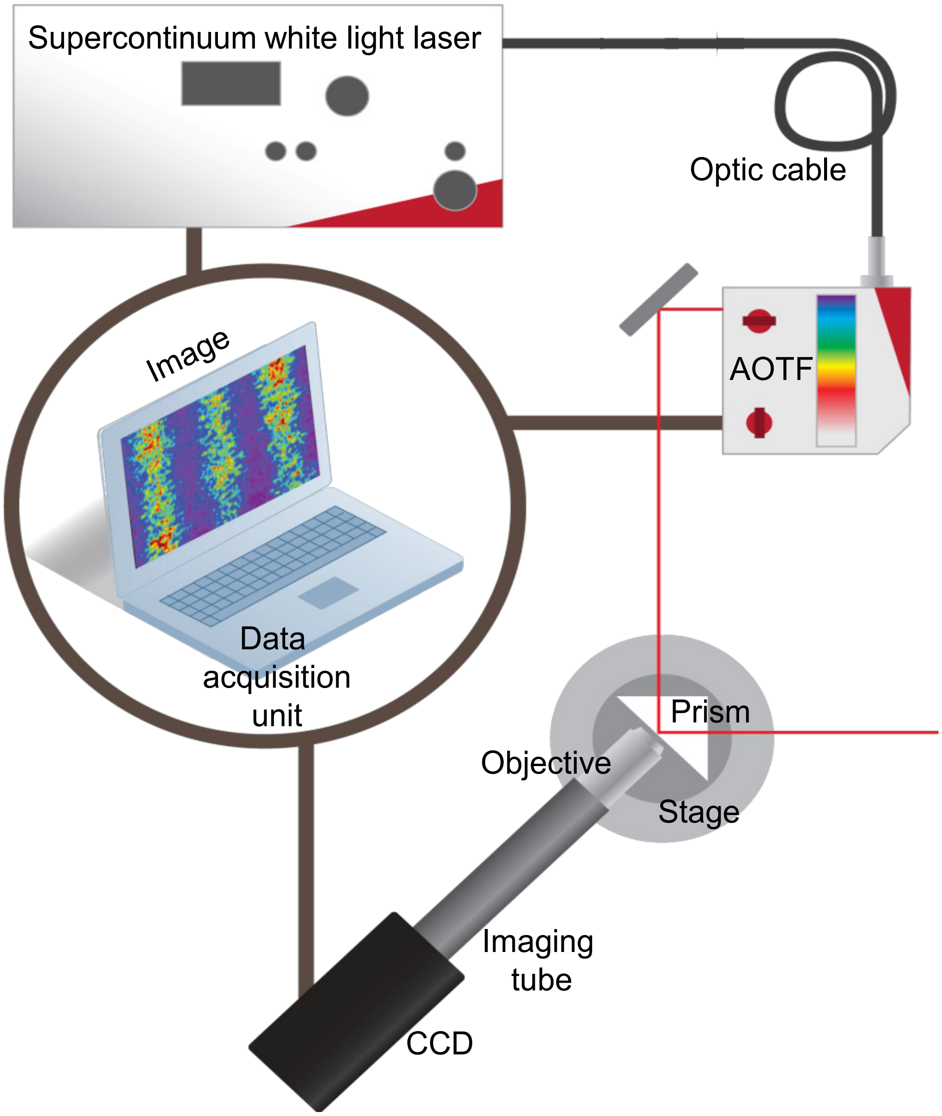

Figure 6.3: Detailed schematic representation of the experimental apparatus used to image SPP waves on Moiré surfaces. A supercontinuum white light laser with attached AOTF has been used as an excitation laser. Cavity mode can be selectively illuminated to observe the spatial distribution of SPP waves in the cavity region. The scattered SPP waves from the cavity region are collected by an objective and directly imaged using digital CCD camera. ©2011 OSA

bandwidth of the excitation light is less than 5 nm while the incident power is 2.5 μW (at 615 nm) before it hits the sample.

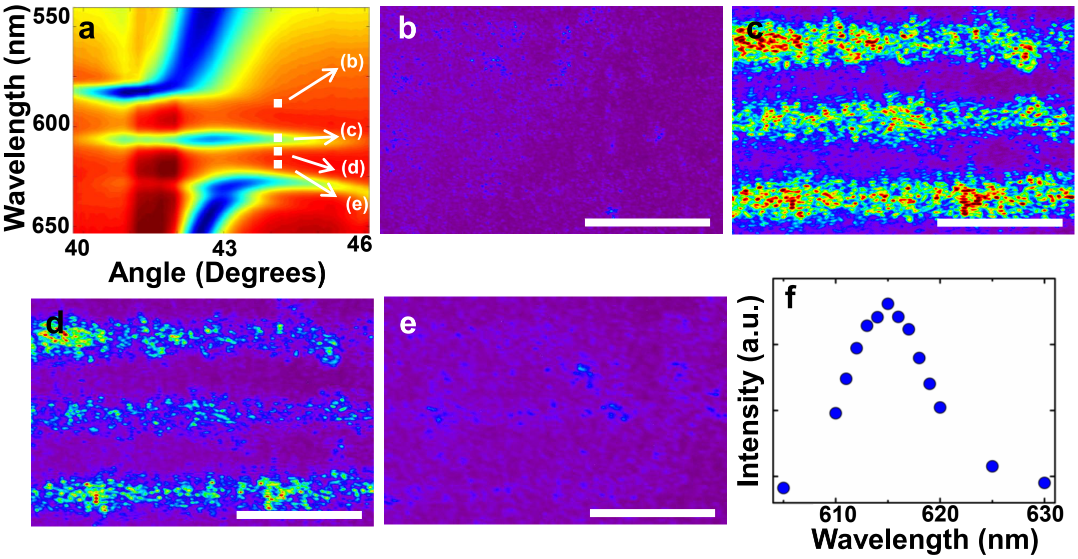

Figure 6.4: (a) Experimental dispersion curve of 15.0 μm long SPP cavities showing a bandgap and a cavity state. DFPM image of 15.0 μm long three SPP cavities imaged with the laser wavelengths of (b) 580 nm, (c) 615 nm, (d) 620 nm, and (e) 630 nm. The white colored bar indicates 15.0 μm long distance. (h) Calculated intensity of the cavity mode from DFPM images. The intensity of the scattered light maximizes at ∼615 nm, which is the cavity mode in (a). ©2011 OSA

6.3 Imaging Plasmonic Modes

Fig.6.4a shows a dispersion curve of 15.0 μm long SPP cavities. The curve indicates a band gap where a band of wavelengths are forbidden and a well localized cavity mode of ∼615 nm inside the band gap region. It has previously been shown that this cavity mode band can be modeled using tight binding approach as it was also applied to coupled resonator optical waveguides [78, 86]. Dispersion of the cavity mode can be described as

$$\omega(k) = \Omega[1 + \kappa \cos(kD)] \tag{6.3}$$

where Ω, κ, and D are the resonance frequency of the individual cavity, cavity to cavity coupling coefficient, and the size of the cavity, respectively. It should be noted that κ is a function of both the proximity of the cavities as well as confinement characteristics of each cavity, namely of the groove depth. The group velocity of the SPP waves can be found as

$$v_g(k) \equiv \frac{d\omega}{dk} = -\Omega D \kappa \sin(kD) \tag{6.4}$$

which can be quite small when the cavities are weakly coupled. The slope of the dispersion curve gives the group velocity of the cavity modes (Fig.6.4a). It is clear that the group velocity and the dispersion of SPPs are a function of the coupling coefficient of the cavities. Thus, in order to significantly slow SPPs, the coupling coefficient has to be very small. The dispersion curve in Fig.6.4a clearly reveals that SPPs are almost completely stopped at the plasmonic cavity mode since the slope of the cavity mode is almost zero. The same sample has been imaged using DFPM by varying the incident laser wavelength as pointed in Fig.6.4. Fig.6.4b-e show DFPM images of three cavities with varying incident laser wavelength. The scattered light from the SPPs are collected in the far field by a CCD camera and images are formed with exposure time of 1 second. It should be noted that SPPs remain nonradiating as long as they propagate on a surface which is translationally invariant in the propagation direction where SPPs decay only by ohmic losses in the metal [121, 122]. However, surface roughness will cause scattering of SPP waves due to the breakdown of translational invariance and therefore, scattered SPPs can be detected in the near or far fields using a suitable optical detection system [121, 122]. When SPPs scatter from the surface, the SPP wave can transfer part of its momentum to the defect and decay into a photon. Each line in Fig.6.4b-d represents the light scattered from one cavity. Fig.6.4f shows intensity of the scattered SPPs as a function of the laser wavelength. The DFPM images with high contrast show that spatial localization of cavity mode occurs at 615 nm, which is the cavity mode in the dispersion curve (Fig.6.4a). It is noteworthy to mention here that DFPM imaging experiments with cavity sizes smaller than 15.0 μm have also been performed and substantially decreased contrasts in the images have been observed, which is due to the fact that localization of SPPs decreases when the cavity size decreases for a fixed grating groove depth.

Furthermore, the coupling coefficient between the 15.0 μm long cavities was varied by tuning the grating groove depth resulting in the modification of group velocity and dispersion of SPPs. Fig.6.5a-c show dispersion curves of cavities with the groove depths of 15 nm, 30 nm, and 50 nm, respectively. High-order Bragg reflections appear as the grating groove depth increases [109].

Group velocity of SPPs can be significantly decreased ($\sim 0c$) when the groove depth increases since the slope of the cavity mode in the dispersion curve decreases as the depth increases. The experimental dispersion curves shown in Fig.6.5a-c have been reproduced using FDTD calculations for the depths of 15 nm, 30 nm, and 50 nm. Fig.6.5d-f indicate DFPM images of 15.0 μm long cavities at 615 nm cavity resonance wavelength with grating groove depths of 15 nm, 30 nm, and 50 nm, respectively. Fig.6.5g, demonstrating the line scans from the DFPM images perpendicular to the long axis of the cavities, indicates that spatial full width at half maximum (FWHM) of the intensity peaks in Fig.6.5g decreases with the increase in grating depth. FDTD calculated field distribution around the cavity region is shown for grating groove depth of 15 nm in Fig.6.5h, and 50 nm in Fig.6.5i. The DFPM images and corresponding line scans reveal that as the depth of the grating groove increases, the confinement of SPPs in the cavity region increases showing transition from collective modes (delocalized) to isolated modes (localized). Both reflection measurements and DFPM imaging indicated spatial localization of SPPs in cavities in agreement with the FDTD calculations.

In conclusion, direct imaging of localized SPP waves in plasmonic cavities by DFPM is shown. Tuning the excitation wavelength, the spatial distribution and dispersion of SPP waves in the cavities have been directly measured. When the size of the SPP cavities is very large, coupling coefficient between the cavities approaches zero and hence each cavity behaves like an isolated cavity separated from the ensemble. Transition from collective cavity modes to isolated cavity modes, observable using DFPM, can be achieved by tuning the Bragg grating groove depth. Spectroscopic reflection and DFPM measurements are correlated and found to be in agreement with FDTD calculations. Small group velocities ($\sim 0\ c$) and localized behavior of SPPs on coupled plasmonic cavities suggest that Moiré cavities with slow plasmons can support enhancement and amplification of plasmon-exciton interaction. This point is explained in the next chapter.

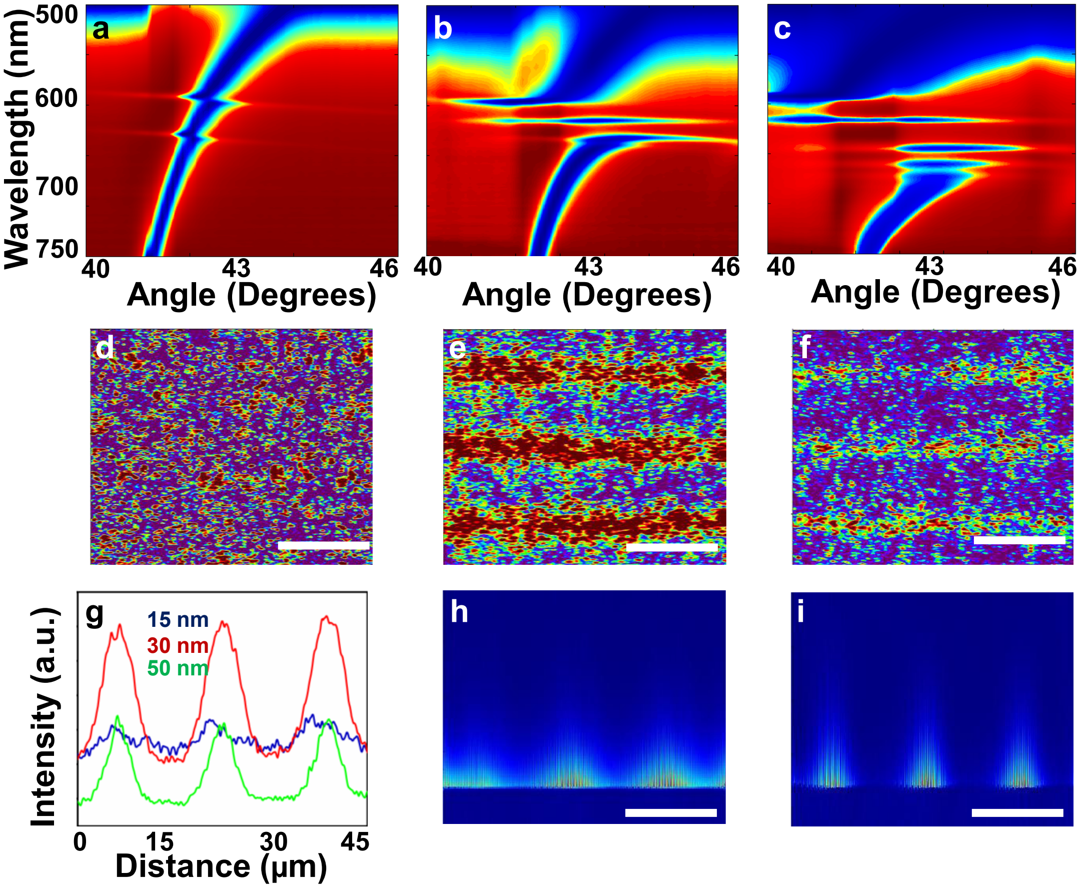

Figure 6.5: (a) Experimental dispersion curves showing band gap and cavity state for 15.0 μm long cavities with grating groove depths of (a) 15 nm, (b) 30 nm, and (c) 50 nm. DFPM images of three cavities with grating groove depths of (d) 15 nm, (e) 30 nm, and (f) 50 nm. DFPM imaging is performed at an incidence angle of ∼42.50 and the wavelength of the incident light is ∼615 nm. (g) Line profiles perpendicular to the long axis of the cavities indicate the intensity of the scattered SPP waves from the cavity region. FDTD calculated two-dimensional electric field distribution at the cavity wavelength for 15.0 μm long three plasmonic cavities with grating groove depth of (h) 15 nm, and (i) 50 nm. As the depth of the grating groove increases localization of SPPs in the cavities increases as well. The white colored bars indicate 15.0 μm long distance. The vertical length of the images in (h) and (i) is ∼2 μm long. ©2011 OSA

Chapter 7

Lasing in a Slow Plasmon Moiré Cavity

Slowing down group velocity, v_g, of light increases interaction time between light and matter. This provides an additional advantage to reduce device size and operating power of photonic devices [123, 124]. Slow light is obtained using quantum interference effects [125, 126] as well as photonic crystals [123] and fibers [127]. Stimulated Brillouin [127] and Raman [128] scattering use the rapid variation of index in the vicinity of Brillouin or Raman gain to obtain slow light modes. Slow light modes in optical buffers and delay lines require a lot of chip real estate due to the wavelength of light [124]. SPPs, instead of confined light can reduce the device size [129].

In this chapter, experimental demonstration of SPP amplification with slow plasmon mode inside the Moiré cavity [86] is demonstrated. SPPs inside the cavity have been slowed down to maximum group velocity of $0.2c$. Also by chancing the periodicity of the Moiré cavity structures, output wavelength of the plasmonic laser is tuned.

The standing wave modes at the band edges of the simple plasmonic grating structures have been studied for enhancing photo emission [47, 56, 85, 91, 130]. Plasmonic Bragg cavity structures [131], on the other hand have been shown to be useful for investigation of various planar SPP physics [132]. More sophisticated grating structures such as dielectric loaded biharmonic [85] and Moiré cavities [86, 120] accommodate a slow propagating cavity mode inside the band gap [26] just like coupled resonator optical waveguides (CROWs) [133]. The cavity mode inside the Moiré cavity is confined between amplitude modulated Bragg mirrors [131]. In this chapter, such Moiré cavities with slow plasmon modes will be discussed. These modes amplify surface plasmon polariton (SPP) signal beyond spontaneous emission [134] and these cavities exhibit plasmonic lasing action [18–20, 91, 135–137].

Lasing action in plasmonic cavities needs three important components to amplify the SPP signal: an optical gain medium interacting with surface plasmons, which helps to compensate for signal loss; a feedback mechanism which is provided by the metallic grating at the band edges or the cavity state, where some of the signal is fed back into the gain medium; and, a pump source, to excite the gain medium. In a Moiré cavity, the slow plasmon mode is expected to further accelerate the lasing action due to increased interaction time between the surface plasmon polariton and the excitonic matter.

Similar to a photonic laser, a plasmonic laser establishes a population inversion in the gain medium, when, the number of excited electrons exceeds the number of lower state electrons. Population inversion is manifested as a threshold in the pump vs. output light signal diagram. Lasing is also accompanied with a spectral narrowing at the emission wavelength. In addition to the formation of threshold and spectral narrowing, signatures of lasing specific to SPP amplification are related to the plasmon polaritonic nature of the interaction as indicated by a high TM/TE contrast in the output signal. The polaritonic effect can also be tested through the replacement of the metallic film. Field enhancements due to the surface plasmon modes are sensitive to the optical properties of the metal film used, hence replacing the metal film will dramatically alter the enhancement and lasing properties of the structure. Due to the evanescent nature of the SPP modes, gain medium is located just above the metallic surface where the feedback occurs. This helps to suppress contributions from the optical modes [138]. The emission enhancement due to plasmonic modes at this proximity is comparably larger than the free space emission [8, 139], due to the increased decay rates of the fluorophores involved [8]. SPP amplification in a slow plasmon Moiré cavity provides a further degree of freedom for future studies on controlled plasmon-matter interaction dynamics.

7.1 Reflection Map Modelling and Eigenfrequency Analysis

Two types of simulation analysis is employed. Reflection maps are simulated by setting up the simulation almost identical to the experimental setup with plane wave source and power monitor or Fourier analysis can be done to obtain eigenfrequencies by exciting SPP modes with random dipole distribution and recording the power distribution with time monitors. Simulation of the reflection maps and eigenvalue decomposition are done with *Lumerical FDTD Solutions* software. For the simulation of the gratings, Bloch boundary conditions are employed along the grating direction. Refractive indices of BK7 (*SCHOTT N-BK7*) and ZF13 (*SCHOTT SF11*) prism are taken from *SCHOTT*s technical documents. Refractive indices of water, laser dye solutions, and ethylene glycol are characterized with ellipsometer (Sec.2.4).

Reflection map simulations give almost identical results with the experiments. However, eigenvalue analysis gives richer information about the system. For flat metal, for instance, we can obtain SPP dispersion with reflection simulation. However, eigenvalue analysis also takes into account the free space photons. In the uniform grating case, one can investigate backwards scattered SPP modes in eigenvalue analysis, but reflection simulation lacks this information. It should also be noted that eigenfrequency analysis gives direct dispersion curve characteristics, i.e. frequency vs. wavenumber/momentum. The point where the eigenfrequency analysis comes short is investigation of doubly periodic structures. In these cases, Bloch boundary condition sometimes cause unobservable SPP modes to appear in eigenvalue analysis as in Fig.7.1b, where Moiré cavities exhibit unnecessarily rich band structure due to band folding effect. Band folding effect occurs when two periods of the periodic structure are included in a unit cell of the structure. For instance, in the uniform grating structures, if one were to take twice the periodicity of the grating as the total unit cell, in the reciprocal space, the Brillouin zone would be reduced to half. Since the main periodicity cannot fit in halved Brillouin zone, band would fold into two with artificial reflections off the zone edges. This is a well known artefact in band structure calculations of semiconductor lattices or in any calculation involving Bloch boundary conditions.

In Fig.7.1, results of eigenvalue simulations are presented. Fig.7.1a, is the band structure of a uniform grating with 250 nm pitch calculated with eigen frequency analysis. M indicates Brillouin zone edge along grating direction. Solid curves are analytically calculated SPP dispersion curves of flat metal surfaces in contact with dielectrics and dashed lines are light lines in those dielectric media (air or laser dye solution). *1* is the SPP curve with laser dye solution, *2* is that with AZ5214 photoresist, and *3* is with vacuum (Daggered numbers are backward propagating SPP modes). If the surface is patterned with a grating structure, we see reflected SPP modes at the zone edge. Right at the point where zone edge crosses an SPP mode, a band gap is introduced. Width of this band gap is related to several parameters, such as grating depth [48]. Highlighted area is the zone that is probed with reflection map measurements. Fig.7.1b, expands about the same k range as that is shown in a (1.1×10^{-7} m^{-1} to 1.4×10^{-7} m^{-1}). We see a lot of band crossing due to the mathematics of Bloch boundary conditions. In Moiré cavities, unit cell is several orders of magnitude bigger than that of uniform gratings. In k space this manifests as several orders of magnitude smaller k-span. In Fig.7.1c, marked area in Fig.7.1a is expanded. It is very difficult to extract useful information from this diagram, so for Moiré structures, only reflection simulations are taken into account.

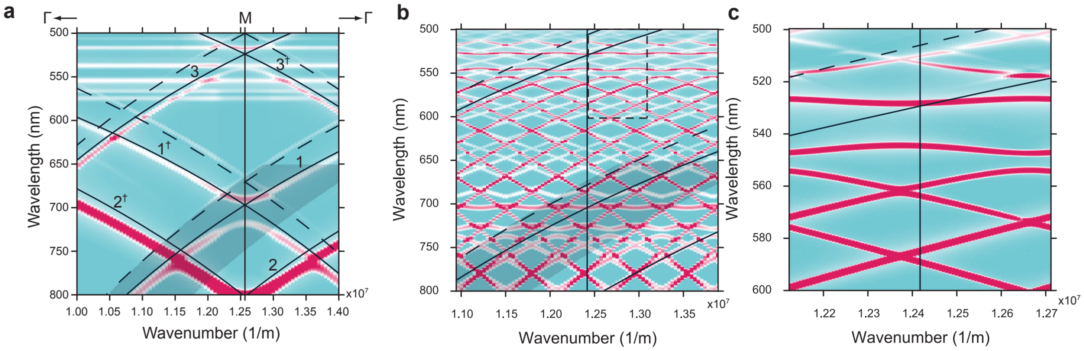

Figure 7.1: Simulated band structures. ©2015 APS

7.2 Experimental

The designed experiment setup consists of a Moiré 250+256 nm cavity in contact with a laser dye solution (Fig.7.2a). The Moiré cavity has a fast modulation amplitude [Eq.(6.1), with a period of 253 nm, and a slow varying envelope [Eq.(6.2)] whose period is 10.7 μm. Cavity states are localized at the node of the Moiré cavity where the amplitude of the fast modulation reaches to its minimum (Fig.7.2f). SPP characteristics of the Moiré cavity can be understood by constructing polarization dependent spectroscopic reflection maps. These maps are obtained by recording the reflection spectrum of the sample in Kretschmann configuration at various incidence angles (see Sec.7.4) at p-polarization. A simulated reflection map is shown in Fig.7.2c, which is calculated with the finite difference time domain (FDTD) method. The forbidden region in the dispersion relation of the SPPs formed by lifting the degeneracy of the forward and the backward propagating SPP modes [47] gives way to a new state in the Moiré cavity [86] due to the amplitude modulation of the Moiré cavity. The cavity state lies between the two band edges where lower band edge with higher frequency is at around 525 nm and the upper band edge with lower frequency is at around 550 nm. The same structure in contact with the dye solution (Fig.7.2d) has similar SPP features with 170 nm shift to the red of the spectrum. Fig.7.2e shows the group velocity values along the cavity state shown in Fig.7.2d. The v_g has its maximum at the centre of the cavity as $0.16c$ where c is the speed of light, and at the edges of the cavity state, it approaches to zero. Fig.7.2f and Fig.7.2g show the electric field profiles of the cavity mode marked in Fig.7.2c and Fig.7.2d, respectively. The cavity mode in Fig.7.2g moves slightly towards the dielectric medium above the cavity structure due to the increase in the effective index. Both modes are localized around the node of the Moiré cavity.

The measurement setup is discussed in detail in Sec.2.5. Pump power is controlled with neutral density (ND) filters and combination of Glan-Thompson (GT) polarizer and polarization splitter. In Fig.7.3, total power response of ND and GT for several combinations is presented. In order to scan the power range of 0.12 mW to 25.1 mW suitable ones are selected, which are marked on the graph. It should be noted here that, response of GT is not linear but is a function of $\cos^2$, so it is crucial to analyze the final data by using power output of ND and GT combinations in order to eliminate false threshold results.

In some cases, lasing peak saturates OSA CCD. In order to avoid that another ND at the output arm of the setup is added. The aim is to record at least three spectrum curves with lasing peaks after the threshold value is reached. Since data analysis is done *ex situ*, sometimes ended up unintended saturated peaks are recorded. These experiments are discarded to be done properly.

Due to the local heating, and poor adhesion of metal film to the PR layer, samples become useless after several hours of experiment (Fig.7.5). Hence all measurements are done in one setting. Confirmation measurements are done on identical samples.

Power output of the *Spectra Physics QuantaRay Lab 150* Nd:YAG laser is measured with *Melles Griot 13PEM001* Broadband Power/Energy Meter. Each pulse is 6-8 ns long and the laser is triggered 10 times at each second. Beam

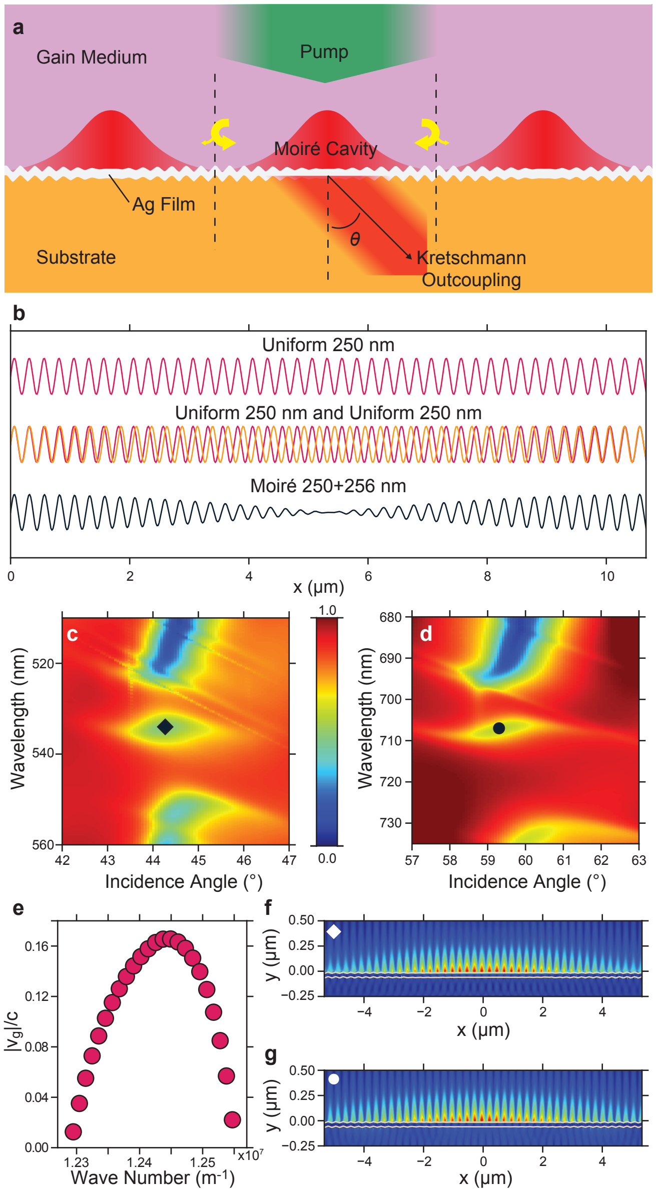

Figure 7.2: Designed experiment schema and simulation results. ©2015 APS

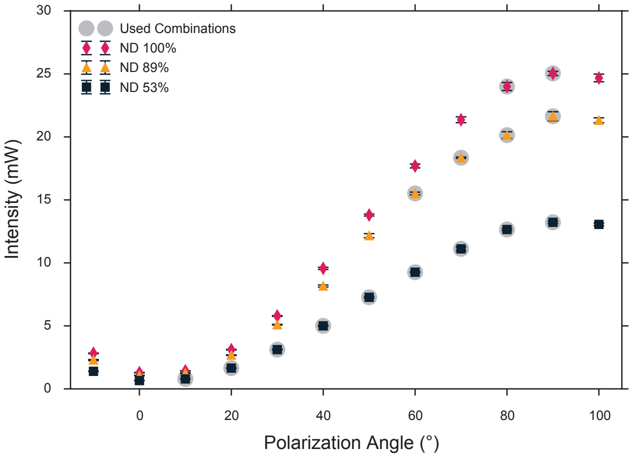

Figure 7.3: Pump power control. ©2015 APS

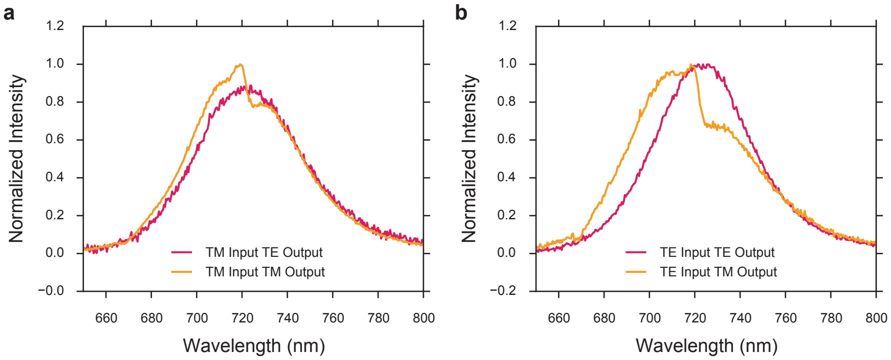

Figure 7.4: Input polarization test. Sample is a 240 nm pitched uniform grating coated with 45 nm Ag film. ©2015 APS

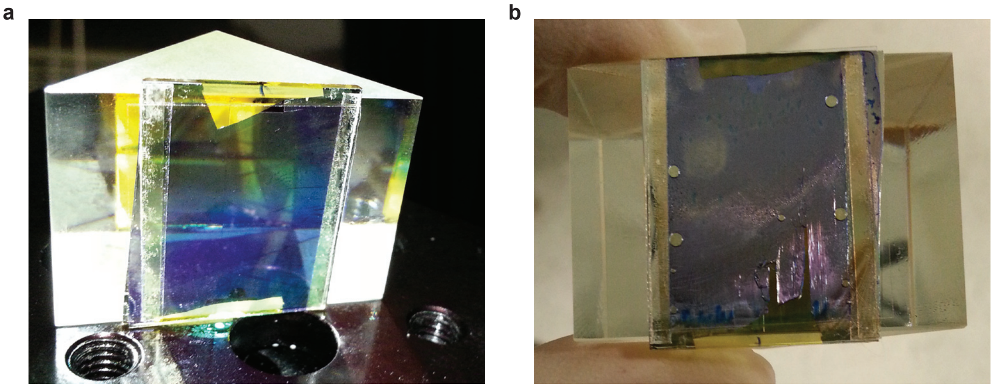

Figure 7.5: Photographs of the microfluidic cell. (a) before the experiment and (b) afterseveral hours of experiment. ©2015 APS

diameter at the output is 10 mm, which is reduced to 6 mm and collimated with a Galilean beam shrinker (Fig.2.6). Energy per pulse per unit area is calculated with the following formula,

$$E_a = \frac{P_{\mathrm{avg}}}{fA}$$

where P_{avg} is the average power that is measured with power meter, f is the trigger frequency (10 Hz), and A is the beam area. Peak power can also be calculated by dividing $E_a \cdot A$ to pulse duration (6-8 ns). Maximum power used for excitation of dye solution is around 25 mW, corresponding to 357 kW of the peak power.

7.3 Experimental Reflection Maps

Reflection maps in Fig.7.10a,b are obtained by using *J.A. Woolam V-VASE* Ellipsometer. The ellipsometer is used in the reflection mode with Kretschmann setup mounted on the sample plane. The equipment has the ability to monochromatize the white light from Xe lamp with <1 nm resolution. In addition, it has motorized stage that controls the incidence angle of the incoming beam with $< 0.05°$ resolution. By recording the reflection spectrum for each incidence angle, the full reflection map of a sample is obtained. The reflection map is not a dispersion curve, because momentum is not constant for the given incidence angle with different wavelengths of light. However, one can convert the reflection map to a dispersion curve by a simple coordinate transformation for the incidence angle axis. Wavelength axis is not affected from this transformation, thus one can interpret almost all of the information that a dispersion curve can give, with the reflection map.

Reflection maps of Moiré 260+266 nm cavity in contact with several different dielectrics is presented in Fig.7.6. In Fig.7.6a, the cavity is in contact with air ($n \simeq 1.0$); in Fig. 6b, it is in contact with DI water ($n \simeq 1.33$); in Fig.7.6c, cavity is in contact with pure ethylene glycol($n \simeq 1.6$). Solid curves are analytical calculations for propagating SPP modes in corresponding media. Wavelength of SPP features shifts to red as the refractive index of the medium increases.

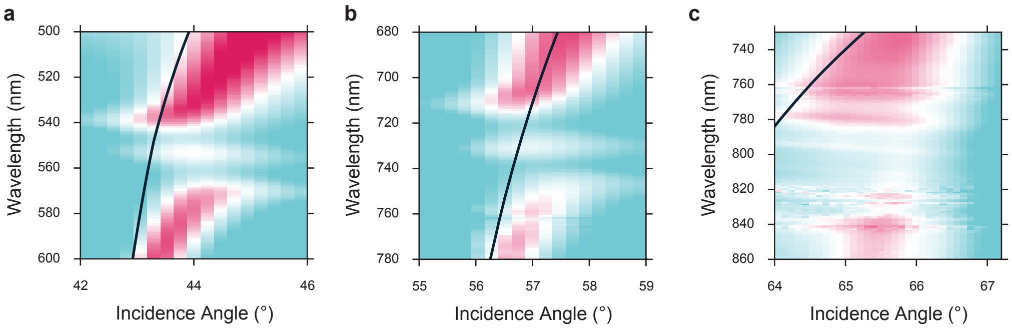

Figure 7.6: Reflection maps of Moiré (260+266 nm) cavity with different dielectrics. ©2015 APS

Transformation from reflection maps (wavelength vs. incidence angle) to dispersion curves (wavelength/frequency/energy vs. wavenumber/momentum) is done via the following formula,

$$k = k_0 n_p \sin\theta,$$

where θ is the incidence angle, n_p is the refractive index of the prism, k_0 is free space wavenumber of the light ($k_0 = 2\pi/\lambda_0$), and k is the wavenumber. In order to transform experimentally obtained reflection data into momentum space, we have first determined the maximum span of the k axis. Then, for each wavelength, we have determined the maximum and minimum values of ks for given incidence angle values. Then reflectivity measurements are interpolated, for that wavelength, to k axis between the minimum and maximum of the k values. Conversion of the reflection map in Fig.7.10a can be seen in Fig.7.7a. As a result of the coordinate transformation, the reflection map becomes highly distorted.

Since a reflection map can give almost all of the information that a dispersion curve can give, and, a reflection map is more suitable for experiments, this coordinate transformation is seldom needed.

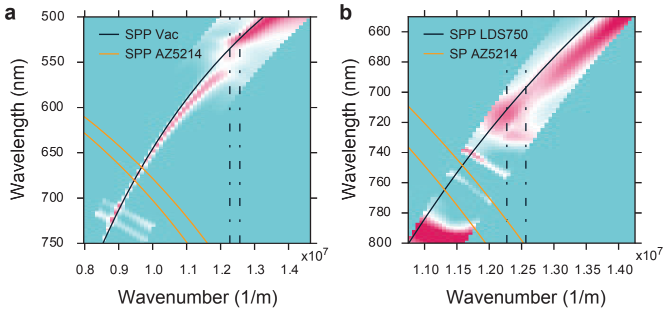

Figure 7.7: Mapping of reflection maps to dispersion curves. ©2015 APS

7.4 Plasmonic Enhancement and Lasing

A SEM micrograph of the cavity is shown in Fig.7.8a. The cavity is obtained by exposing a photoresist (PR) coated soda lime substrate under a laser interference lithography setup (see Sec.2.2). Two sequential exposures are made with different incidence angles to generate large Moiré pattern. PR pattern is then coated with 45 nm Ag film by thermal evaporation to support SPPs. As a gain medium Styryl 7 is used, which is an organic laser dye which is commercially available from *Exciton* (commercial name *LDS750*). Styryl 7 is dissolved in extra pure ethylene glycol solvent from *J.T. Baker* as a 10 mM batch and then diluted to 5 mM, 2.5 mM, and 0.65 mM solutions (Fig.7.12). Afterwards, diluted solutions are injected into a microfluidic channel constructed using two sided adhesive tapes and soda lime cover glass (Fig.7.5). Neither the incidence angle nor the size of the liquid chamber changes the spectral output of the experiments. Surface plasmon coupled emission (SPCE) is demonstrated in planar metal films [134] and gratings [140] on similar setups. The expected SPCE on planar metal films, uniform gratings, and Moiré cavities are observed (Fig.7.14) at low power densities. When the threshold value is exceeded, lasing is obtained with samples that have slow light modes. In Fig.7.8b, absorption and luminescence characteristics of the gain medium are shown. Photoluminescence (PL) of the dye under 532 nm illumination shows a broad peak centred around 715 nm having 60 nm FWHM (145 meV). Under lasing conditions, this peak becomes centred at 718 nm with FWHM of 2.7 nm (6.5 meV). Hence, a dramatic spectral narrowing is observed. The intensity vs. pump energy density plots are obtained by integrating the total area under the lasing peaks and integrating the rest of the luminescence curves and then plotting them as a function of pump energy density. Above the threshold, the integrated area of the lasing peak is much larger than the integrated area of the rest of the luminescence spectrum. Fig.7.8c shows the intensity vs. pump energy density curve measurements for Moiré 250+256 nm cavity. Threshold energy density is around 1.5 mJ/cm^2. Below the threshold value, both integrations give approximately the same results; beyond the 1.5 mJ/cm^2 mark, there is a linear increase in the lasing peak intensity.

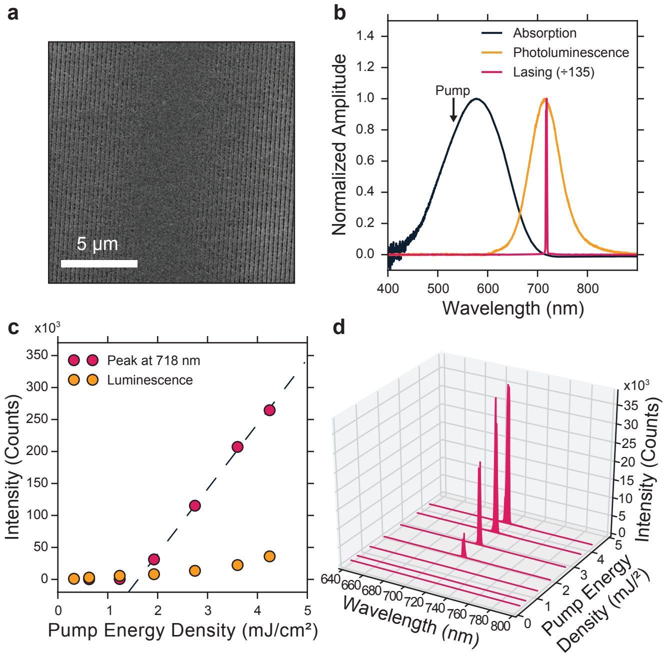

Figure 7.8: Demonstration of plasmonic lasing. ©2015 APS

Components of the Moiré 250+256 nm i.e: uniform gratings with pitches of 250 nm and 256 nm also lases (Fig.7.9). Fig.7.9a, shows the lasing spectrum. Fig.7.9b and Fig.7.9c show the thresholds. The grating with 250 nm pitch exhibits lasing with threshold energy of 2.8 mJ/cm^2 and FWHM of 1.9 nm (4.5 meV), while the grating with 256 nm pitch exhibits threshold energy of 4.4 mJ/cm^2 and FWHM of 1.0 nm (2.2 meV).

Fig.7.10a and Fig.7.10b show the experimentally obtained reflection maps for the Moiré 250+256 nm cavity in the air and in the dye solution, respectively. *1*

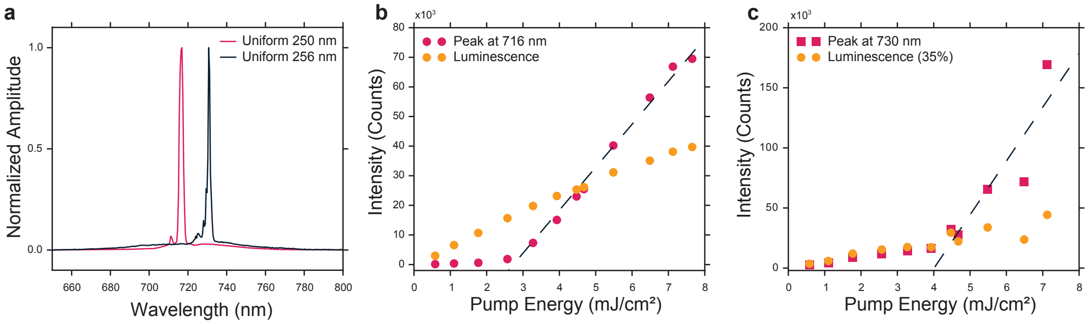

Figure 7.9: Lasing characteristics of Uniform 250 nm and Uniform 256 nm gratings.

marks the cavity state which is supporting the lasing action, whereas *2* and *3* mark the upper and the lower plasmonic band edges, respectively. In Fig.7.10b, modes marked with *4* are SPP modes on the opposite sides of the metallic film, in this case metal-PR interface. Considering both sides of the metallic grating, there are two modes: one is created along the metal-upper dielectric interface and the other at the metal-lower dielectric interface. Modes on the opposite side can be excited via the grating structure [54, 56, 130]. These modes are isolated from the interaction on the upper face of the metal film. The spectral position of the cavity state in Fig.7.10a is around 545 nm in air, and because the sample is in the dye solution, all SPP modes are shifted to the red of the electromagnetic spectrum in Fig.7.10b. Fig.7.10e and Fig.7.10f show the group velocity for the cavity modes shown in Fig.7.10a and Fig.7.10b, respectively. In both cases v_g does not exceed about $0.35c$; in the dye solution v_g is $0.25c$ at the centre of the mode, approaching the calculated value. As expected, v_g approaches to zero at the edges of the cavity state. The lasing is observed at the falling edge of v_g at Fig.7.10f. The experimental results confirm the calculated results. Cavity states are located at the expected k values ($1.24 \times 10^7 m^{-1}$) and the cavity centres are close to the same wavelengths. Small differences can be attributed to oxidation of the Ag film (around 2 nm), imperfect grating profiles, and the experimental errors while extracting optical parameters of the dielectric films (see Sec.2.2).

In order to vary the central frequency of the cavity mode, three different Moiré cavities labelled 242+248 nm, 250+256 nm, and 260+266 nm are fabricated and

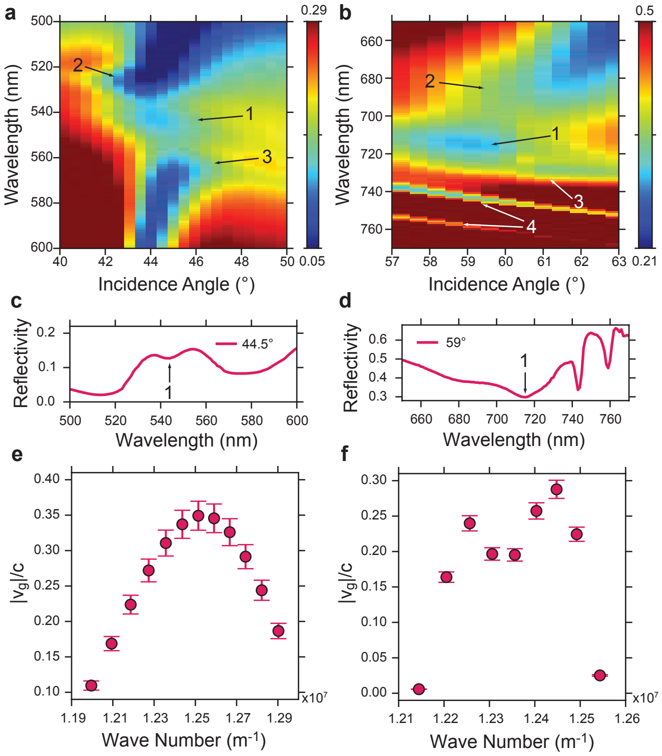

Figure 7.10: Role of the Moiré cavity in plasmonic lasing. ©2015 APS

compared to the plasmonic lasing performance of the Moiré cavities in Fig.7.11a. The 242+248 nm Moiré cavity has its lasing peak at 713 nm with FWHM of 1.34 nm (3.3 meV) and the 250+256 nm Moiré cavity has its lasing peak at 718 nm with FWHM of 2.7 nm (6.5 meV), while the 260+266 nm Moiré cavity has its lasing peak at 726 nm with FWHM of 2.8 nm (6.5 meV). As the cavity states of these gratings shift, a proportional shift in the lasing peak wavelength is observed (Fig.7.11b), which validates that the plasmonic lasing action is indeed due to the cavity modes. It also expected that replacing the material of the metal film should alter the lasing behaviour. Au and Ag are well known for their SPP properties in the visible spectrum whereas Ti does not support SPP modes in this part of the spectrum. In the visible spectrum, it has been expected that Au has a lower SPP resonance frequency compared to Ag, and the SPPs on Ag has longer lifetimes compared to the SPPs on Au [141]. Fig.7.11c shows PL spectra obtained with the 242+248 nm Moiré cavities coated with different metals. Au coated samples exhibit SPP features but no lasing peak is observed, while Ti coated samples exhibit only PL spectrum of the dye solution. Ag coated samples, on the other hand, exhibit lasing peaks, and these peaks are highly TM polarized, which is another finger print of SPP based amplification. Since SPP modes are excited with the near field coupling, rotating the polarization of the source to TE direction and probing the output for TM/TE contrast (Fig.7.4), the same TM/TE distinction (no SPP features in TE, SPP features in TM) is observed at the output under both TE and TM excitation.

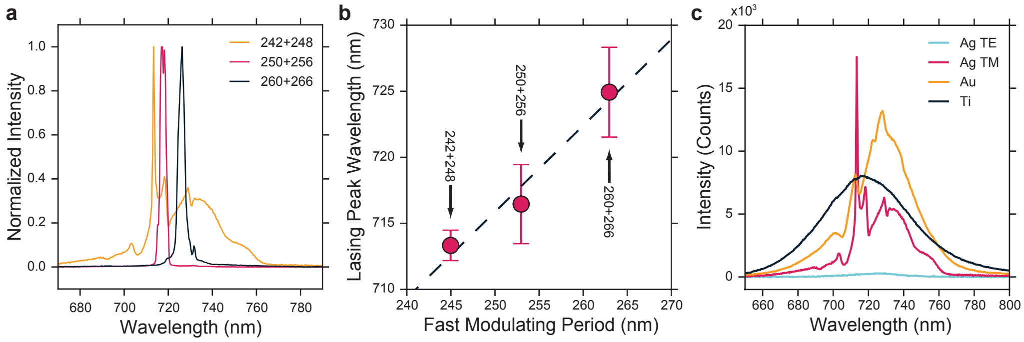

Figure 7.11: Plasmonic lasing confirmation tests. ©2015 APS

Effect of dye concentration on lasing is shown in Fig.7.12. Fig.7.12a, shows the intensity output as a function of pump power for various dye solution concentrations with same type of Moiré cavity (242+248 nm). Fig.7.12b, is the spectrum of these samples at maximum pump power. As the dye concentration increases threshold power decreases, however slope of the curves differs. Decrease of the threshold value with increased concentration is expected, since the probability of the dye solution to interact with the SPP modes increases. The slope change may be due to the efficiency reduction due to increased number of dye molecules which absorbs incident photon and emits outside of the vicinity of the metal film, hence without excitation of an SPP mode. For the case of 0.65 mM solution, there may be a threshold of lasing at higher pump powers, but powers higher than 25 mW destroys the metal film due to heat build up.

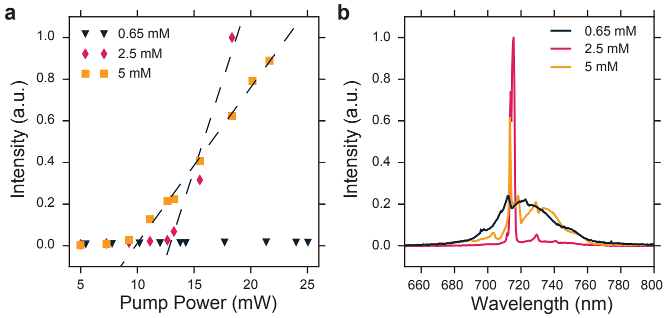

Figure 7.12: Effect of dye concentration. ©2015 APS

Quality factor along the cavity states of Moiré 252+256 nm cavity in contact with air (Fig.7.10a) and dye solution (Fig.7.10b) is presented in Fig.7.13a and Fig.7.13b respectively. A slight 5 point increase in quality factor in solution compared to air is observed.

The setup in Fig.2.6 is optimized to observe SPCE. In Fig.7.14a, SPCE from a flat metal surface is presented together with reflection spectrum at corresponding angles. *LDS750* solution concentration is 0.65 mM. In Fig.7.14b, Reflection spectra and SPCE for Moiré cavity (242+248 nm) is presented. Two sharp dips due to the opposite side plasmons are manifested as shoulders in SPCE curves which indicates that opposite side plasmon interaction with the dye is minimal compared to the SPPs in solution side. *LDS750* solution concentration is 2.5 mM. In

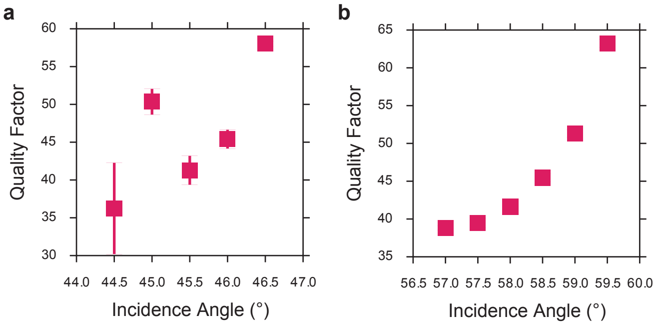

Figure 7.13: Quality factor along cavity states. ©2015 APS

Fig.7.14c and Fig.7.14d, SPCE curves for uniform gratings of 242 nm and 250 nm pitches are presented respectively. For 242 nm pitch uniform grating, resist side SPPs dominate the emission because their frequency does not coincide well with the gain curve of the solution. A similar situation is observed in 250 nm case, however at this pitch, solution side SPPs are further into the gain curve and we see a more enhanced emission compared to the 242 nm case. Both in Fig.7.14c and Fig.7.14d concentration of the solution is 5 mM.

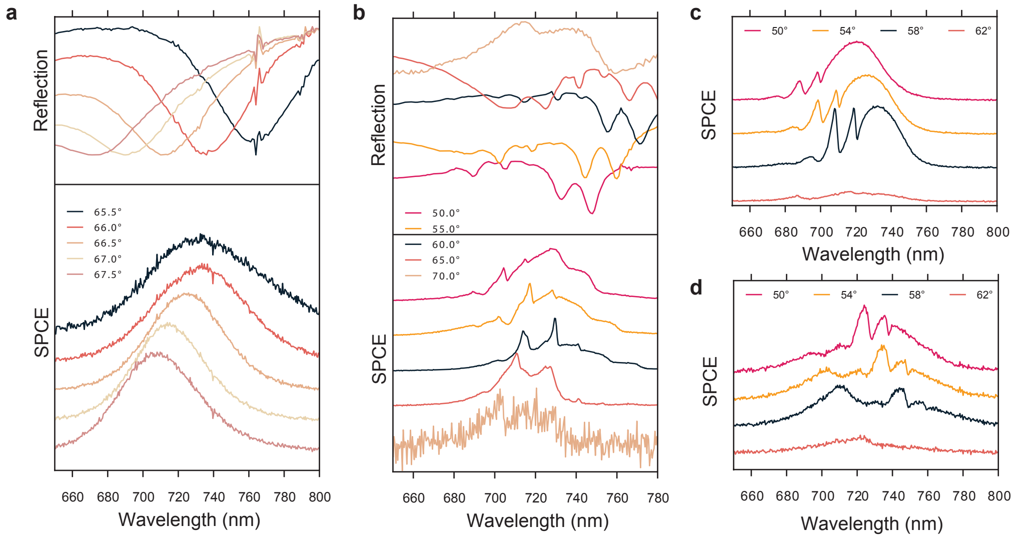

Figure 7.14: Surface plasmon coupled emission. ©2015 APS

Out coupling of the light from the amplified SPP mode is highly directional. The spectrum is measured at different collection angles both from the prism side and from the grating side (See Fig.2.6). Collection angle on the grating side is defined as the angle between the incident excitation beam and collection arm. The angle on the prism side is defined as the angle between apex of the prism and the collection arm. In Fig.7.15a, peak intensity of the spectrum at different collection angles is presented. Since there are two superposed gratings on the surface, we see several out coupling peaks intertwined. In In Fig.7.15b, peak intensity vs. the collection angle is presented for the prism side. Unfortunately, even though no lasing peak between 55° and 60° is observed, the results haven't been recorded. There are two out coupling angles, one with 1° directionality and the other with 2° directionality. The peak at 60° is expected due to the reflection map results, however the second peak at 66° indicates that the out coupling of the lasing photons are mediated through resist side SPPs. In Fig.7.15c, total emission spectra at angles in In Fig.7.15b are presented.

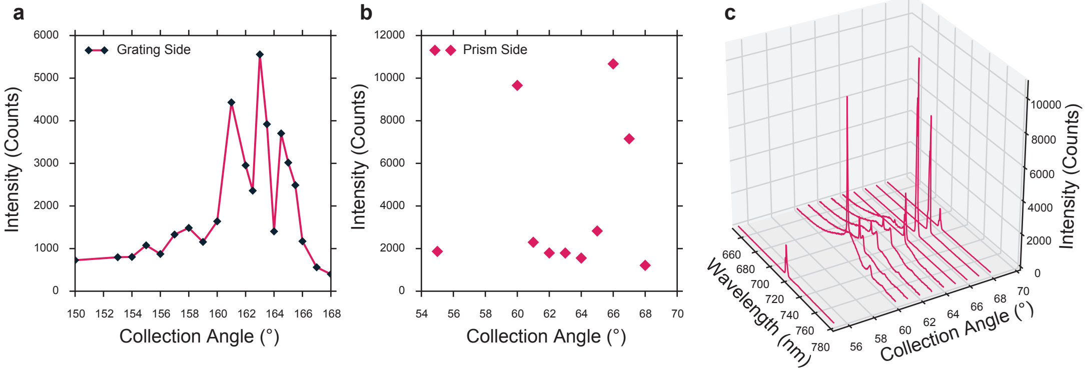

Figure 7.15: Directionality of out coupling in Moiré cavity (250+256 nm). ©2015 APS

In conclusion, a plasmonic laser based on the slow plasmon modes of the Moiré cavity structures is demonstrated. The flexible platform of the plasmonic superstructures generated by Moiré pattern allows us to control the group velocity of SPPs and then greatly amplify the emission of the organic dyes in the visible part of the electromagnetic spectrum. Here the lasing action of the Moiré cavity structures is enabled by the slow SPPs at the edges of the cavity modes. Furthermore, the output of the lasing is tuneable since the periodicity of the Moiré cavity determines the resonance frequency of the cavity mode. This demonstration, to our knowledge, is the first one that shows a slow plasmonic mode of a grating cavity structure, interacting with an exciton medium, can amplify the

SPP signal. Further studies may include working on structures that amplify SPPs in different parts of the spectrum. In order, for example, to amplify visible wavelengths, gratings with smaller pitches have to be fabricated, and/or lower refractive index dye solutions have to be prepared. A further improvement on SPP mode efficiency could be achieved by loading an epitaxially grown metallic film instead of one with the thermal evaporation. This would further reduce the ohmic and scattering losses of SPP modes and would bring the lasing threshold energy down.

Chapter 8

Conclusions and Future Work

Throughout this thesis, physics and engineering of plasmon-matter interaction is discussed with experimental and theoretical demonstrations. Control of light-matter interaction in the nanoscale is done with SPPs which propagate to the metal-dielectric interface. In lateral directions, SPP modes can further confined with Moiré cavities. Localized to such a small volume, SPPs interacting with excitons are suitable for interaction amplification.

In order to understand SPP-Matter interaction, plasmon-exciton coupling is studied in Chapter 3. Coupling dynamics are demonstrated both in strong and weak coupling regimes. Rate of energy transfer is function of the damping of plasmons and excitons (Eq.(3.3)). Hence coupling strength can be controlled via plasmonic damping which is controlled with the thichness of the metal film. Very thin metal layer results in increased ohmic loss and scattering loss. It is shown that, after a critical metal layer thickness, surface plasmons and excitons form a hybrid state and slip into the strong coupling regime. At this state, anti-crossing in the dispersion curve due to Rabi splitting is observed. On the other hand, it is possible to affect optical properties of excitons via surface plasmons on ultra thin metal surfaces. At this case we are in the weak coupling regime. Instead of forming coupled SPP-Exciton pairs or plexcitons, wave functions of SPPs and excitons are slightly perturbed. The perturbation results in enhancement of optical absorption of excitons.

In Chapter 4, engineering of plasmon-exciton interaction is presented. Patterning the metal surface with a sine grating introduces a forbidden region for propagating surface plasmons in the dispersion curve. The band gap alters the SPP mode propagation and redistributes plasmonic states. At the edges of this gap, plasmons form standing waves which increase interaction possibility with excitons. Width of this gap can be adjusted by engineering the groove depth of the grating. Varying the depth of the grating distribution of plasmonic states (Eq.(4.1))

The work in Chapter 5 takes this approach further and introduces direction dependent control of plasmon-exciton coupling by proposing a new platform: plexcitonic crystals. Using one and two dimensional plexcitonic crystals, it is shown that plasmon-exciton interaction dynamics can be controlled in a reversible fashion. Two dimensional plexcitonic crystals have different symmetry depending on the geometry of the the crystal. Although square lattice plexcitonic crystals offer a wider tunability of the band gap energy, triangular lattices offer better omnidirectional uniformity. Having built several tools to understand and control the plasmon-exciton interaction. We move on to confinement of SPP modes for interaction amplification.

Patterning the surface with specially constructed doubly modulated gratings which are called Moiré gratings, introduce a confine mode inside the band gap of the crystal. This confined cavity mode can be directly imaged as shown in Chapter 6. Throughout this mode SPPs are slowed down to fraction of the speed of light. This slow plasmon mode increases the interaction time of plexcitons, which makes Moiré cavities good candidates for feedback for use in plasmonic lasing.

In Chapter 7, slow plasmon behavior is put to use for surface plasmon amplification and a plasmonic laser is demonstrated. Moiré cavities in contact with a suitable excitonic medium with matched gain curve are shown to overcome ohmic and scattering losses of surface plasmons. This result, to author's knowledge is the first demonstration of plasmonic lasing based on holographic gratings. Wavelength of the plasmonic lasing can be controlled by varying the periodicity of the grating. With the ability to fabricate such nanostructures in very large areas, this scheme becomes a promising platform for future plasmon-matter interaction research.

There are many interesting experiments that need to be done to investigate plasmon-matter interaction within the framework that is laid down by this dissertation. Quantum dots, for instance, are quite efficient emitters of light at the nanoscale. Interaction dynamics of quantum dots with localized modes supported by Moiré cavities could be interesting to investigate. In this scheme, single-plasmon support inside the cavity can be achieved. Directional response of plexcitonic crystals in connection to plasmon amplification is another interesting topic to develop. Upon everything else, multi layer plasmonic structures also known as long-range plasmons is another direction that the ideas presented in this thesis can be pursued. Long range plasmons offer less loss and mode propagation length which may dramatically affect plasmon-exciton coupling physics.

To conclude, this thesis constructs several frameworks and ideas that are new to the field of plasmonics. It is hoped that these ideas will trigger new frontiers of research on the topic of dynamics of light-matter interaction.

Bibliography

[1] R. H. Ritchie, “Plasma losses by fast electrons in thin films,” *Phys. Rev.*, vol. 106, pp. 874–881, June 1957.

[2] R. A. Ferrell and E. A. Stern, “Plasma resonance in the electrodynamics of metal films,” *American Journal of Physics*, vol. 30, pp. 810–812, Nov. 1962.

[3] W. L. Barnes, A. Dereux, and T. W. Ebbesen, “Surface plasmon subwavelength optics,” *Nature*, vol. 424, pp. 824–830, Aug. 2003.

[4] K. A. Willets and R. P. Van Duyne, “Localized surface plasmon resonance spectroscopy and sensing,” *Annual Review of Physical Chemistry*, vol. 58, no. 1, pp. 267–297, 2007.

[5] M. Fleischmann, P. Hendra, and A. McQuillan, “Raman spectra of pyridine adsorbed at a silver electrode,” *Chemical Physics Letters*, vol. 26, pp. 163–166, May 1974.

[6] S. Nie and S. R. Emory, “Probing single molecules and single nanoparticles by surface-enhanced raman scattering,” *Science*, vol. 275, pp. 1102–1106, Feb. 1997.

[7] H. Kano and S. Kawata, “Surface-plasmon sensor for absorption-sensitivity enhancement,” *Appl. Opt.*, vol. 33, pp. 5166–5170, Aug. 1994.

[8] J. R. Lakowicz, “Radiative decay engineering: Biophysical and biomedical applications,” *Analytical Biochemistry*, vol. 298, pp. 1–24, Nov. 2001.

[9] Y.-J. Hung, I. I. Smolyaninov, C. C. Davis, and H.-C. Wu, "Fluorescence enhancement by surface gratings," *Opt. Express*, vol. 14, pp. 10825–10830, Oct. 2006.

[10] F. Tam, G. P. Goodrich, B. R. Johnson, and N. J. Halas, "Plasmonic enhancement of molecular fluorescence," *Nano Lett.*, vol. 7, no. 2, pp. 496–501, 2007.

[11] I. Freestone, N. Meeks, M. Sax, and C. Higgitt, "The lycurgus cup a roman nanotechnology," *Gold Bull*, vol. 40, pp. 270–277, Dec. 2007.

[12] R. H. Ritchie, E. T. Arakawa, J. J. Cowan, and R. N. Hamm, "Surface-plasmon resonance effect in grating diffraction," *Phys. Rev. Lett.*, vol. 21, pp. 1530–1533, Nov. 1968.

[13] R. H. Ritchie, "Photon excitation of surface plasmons," *Surface Science*, vol. 3, pp. 497–499, Dec. 1965.

[14] H. Raether, "Surface plasma oscillations as a tool for surface examinations," *Surface Science*, vol. 8, pp. 233–246, July 1967.

[15] E. N. Economou, "Surface plasmons in thin films," *Phys. Rev.*, vol. 182, pp. 539–554, June 1969.

[16] E. Kretschmann, "Die bestimmung optischer konstanten von metallen durch anregung von oberflächenplasmaschwingungen," *Z. Physik*, vol. 241, pp. 313–324, Aug. 1971.

[17] T. W. Ebbesen, H. J. Lezec, H. F. Ghaemi, T. Thio, and P. A. Wolff, "Extraordinary optical transmission through sub-wavelength hole arrays," *Nature*, vol. 391, pp. 667–669, Feb. 1998.

[18] R. F. Oulton, V. J. Sorger, T. Zentgraf, R.-M. Ma, C. Gladden, L. Dai, G. Bartal, and X. Zhang, "Plasmon lasers at deep subwavelength scale," *Nature*, vol. 461, pp. 629–632, Oct. 2009.

[19] M. A. Noginov, G. Zhu, A. M. Belgrave, R. Bakker, V. M. Shalaev, E. E. Narimanov, S. Stout, E. Herz, T. Suteewong, and U. Wiesner, "Demonstration of a spaser-based nanolaser," *Nature*, vol. 460, pp. 1110–1112, Aug. 2009.

[20] D. J. Bergman and M. I. Stockman, "Surface plasmon amplification by stimulated emission of radiation: Quantum generation of coherent surface plasmons in nanosystems," *Phys. Rev. Lett.*, vol. 90, p. 027402, Jan. 2003.

[21] S. Balci, C. Kocabas, S. Ates, E. Karademir, O. Salihoglu, and A. Aydinli, "Tuning surface plasmon-exciton coupling via thickness dependent plasmon damping," *Phys. Rev. B*, vol. 86, p. 235402, Dec. 2012.

[22] N. T. Fofang, T.-H. Park, O. Neumann, N. A. Mirin, P. Nordlander, and N. J. Halas, "Plexcitonic nanoparticles: Plasmon exciton coupling in nanoshell j-aggregate complexes," *Nano letters*, vol. 8, no. 10, pp. 3481–3487, 2008.

[23] S. Balci, E. Karademir, C. Kocabas, and A. Aydinli, "Absorption enhancement of molecules in the weak plasmonexciton coupling regime," *Opt. Lett.*, vol. 39, pp. 4994–4997, Sept. 2014.

[24] E. Karademir, S. Balci, C. Kocabas, and A. Aydinli, "Plasmonic band gap engineering of plasmonexciton coupling," *Opt. Lett.*, vol. 39, pp. 5697–5700, Oct. 2014.

[25] E. Karademir, S. Balci, C. Kocabas, and A. Aydinli, "Plexcitonic crystals: a tunable platform for light-matter interactions," *Opt. Express*, vol. 22, pp. 21912–21920, Sept. 2014.

[26] S. Balci, E. Karademir, C. Kocabas, and A. Aydinli, "Direct imaging of localized surface plasmon polaritons," *Opt. Lett.*, vol. 36, pp. 3401–3403, Sept. 2011.

[27] C. Huygens, *Treatise on Light.* BiblioBazaar, Aug. 2008.

[28] M. O. Scully, *Quantum Optics.* Cambridge University Press, Sept. 1997.

[29] J. C. Maxwell, “A dynamical theory of the electromagnetic field,” *Phil. Trans. R. Soc. Lond.*, vol. 155, pp. 459–512, Jan. 1865.

[30] R. E. Collin, “Basic electromagnetic theory,” in *Field theory of guided waves*, pp. 1–54, IEEE Press, 1991.

[31] C. Kittel, “Dielectrics and ferroelectrics,” in *Introduction to Solid State Physics*, pp. 453–485, New Jersey: John Wiley & Sons, 8 ed., 2005.

[32] J. R. Tischler, M. Scott Bradley, Q. Zhang, T. Atay, A. Nurmikko, and V. Bulovi, “Solid state cavity QED: Strong coupling in organic thin films,” *Organic Electronics*, vol. 8, pp. 94–113, Apr. 2007.

[33] M. Fox, “Classical propagation,” in *Optical Properties of Solids*, pp. 25–48, OUP Oxford, Mar. 2010.

[34] J. D. Jackson, “Plane electromagnetic waves and wave propagation,” in *Classical Electrodynamics*, pp. 295–351, Wiley, Aug. 1998.

[35] K.-i. Murata and H. Tanaka, “Surface-wetting effects on the liquidliquid transition of a single-component molecular liquid,” *Nat Commun*, vol. 1, p. 16, May 2010.

[36] N. W. Ashcroft and N. D. Mermin, “The drude theory of metals,” in *Solid State Physics*, pp. 1–28, Cengage Learning, 2011.

[37] C. Kittel, “Plasmons, polaritons, and polarons,” in *Introduction to Solid State Physics*, pp. 393–426, New Jersey: John Wiley & Sons, 8 ed., 2005.

[38] M. Fox, “Free electrons,” in *Optical Properties of Solids*, pp. 143–164, OUP Oxford, Mar. 2010.

[39] P. Lewis and P. Lee, “Band structure and electronic properties of silver,” *Phys. Rev.*, vol. 175, pp. 795–804, Nov. 1968.

[40] D. Eastman and W. Grobman, “Photoemission energy distributions for au from 10 to 40 eV using synchrotron radiation,” *Phys. Rev. Lett.*, vol. 28, pp. 1327–1330, May 1972.

[41] H. Raether, “Appendix i,” in *Surface Plasmons on Smooth and Rough Surfaces and on Gratings*, no. 111 in Springer Tracts in Modern Physics, pp. 118–120, Springer Berlin Heidelberg, Jan. 1988.

[42] H. Raether, “Surface plasmons on smooth surfaces,” in *Surface Plasmons on Smooth and Rough Surfaces and on Gratings*, no. 111 in Springer Tracts in Modern Physics, pp. 4–39, Springer Berlin Heidelberg, Jan. 1988.

[43] P. B. Johnson and R. W. Christy, “Optical constants of the noble metals,” *Phys. Rev. B*, vol. 6, pp. 4370–4379, Dec. 1972.

[44] J. Dionne, L. Sweatlock, H. Atwater, and A. Polman, “Planar metal plasmon waveguides: frequency-dependent dispersion, propagation, localization, and loss beyond the free electron model,” *Phys. Rev. B*, vol. 72, p. 075405, Aug. 2005.

[45] W. L. Barnes, “Surface plasmonpolariton length scales: a route to subwavelength optics,” *J. Opt. A: Pure Appl. Opt.*, vol. 8, p. S87, Apr. 2006.

[46] S. Balci, C. Kocabas, and A. Aydinli, “Critical coupling in plasmonic resonator arrays,” *Opt. Lett.*, vol. 36, pp. 2770–2772, Aug. 2011.

[47] Y. Kitamura and S. Murakami, “Hermitian two-band model for one-dimensional plasmonic crystals,” *Phys. Rev. B*, vol. 88, p. 045406, July 2013.

[48] W. L. Barnes, T. W. Preist, S. C. Kitson, and J. R. Sambles, “Physical origin of photonic energy gaps in the propagation of surface plasmons on gratings,” *Phys. Rev. B*, vol. 54, pp. 6227–6244, Sept. 1996.

[49] R. D. Günther, “Holography,” in *Modern Optics*, John Wiley & Sons, 1990.

[50] Theodore C. Hennessy, “Laser interference lithography,” in *Lithography: Principles, Processes and Materials*, Nova Science Publishers.

[51] J. Humlíček, “Polarized light and ellipsometry,” in *Handbook of Ellipsometry* (H. G. Tompkins and E. A. Irene, eds.), pp. 3–91, Norwich, NY: William Andrew Publishing, 2005.

[52] G. E. Jellison Jr., "Data analysis for spectroscopic ellipsometry," in *Handbook of Ellipsometry* (H. G. Tompkins and E. A. Irene, eds.), pp. 237–296, Norwich, NY: William Andrew Publishing, 2005.

[53] K. Okamoto, I. Niki, A. Shvartser, Y. Narukawa, T. Mukai, and A. Scherer, "Surface-plasmon-enhanced light emitters based on InGaN quantum wells," *Nat Mater*, vol. 3, pp. 601–605, Sept. 2004.

[54] I. Pockrand, "Coupling of surface plasma oscillations in thin periodically corrugated silver films," *Optics Communications*, vol. 13, pp. 311–313, Mar. 1975.

[55] C. Bonnand, J. Bellessa, C. Symonds, and J. C. Plenet, "Polaritonic emission via surface plasmon cross coupling," *Applied Physics Letters*, vol. 89, p. 231119, Dec. 2006.

[56] R. W. Gruhlke, W. R. Holland, and D. G. Hall, "Surface plasmon cross coupling in molecular fluorescence near a corrugated thin metal film," *Phys. Rev. Lett.*, vol. 56, pp. 2838–2841, June 1986.

[57] M. Brune, F. Schmidt-Kaler, A. Maali, J. Dreyer, E. Hagley, J. Raimond, and S. Haroche, "Quantum rabi oscillation: A direct test of field quantization in a cavity," *Phys. Rev. Lett.*, vol. 76, pp. 1800–1803, Mar. 1996.

[58] T. Yoshie, A. Scherer, J. Hendrickson, G. Khitrova, H. M. Gibbs, G. Rupper, C. Ell, O. B. Shchekin, and D. G. Deppe, "Vacuum rabi splitting with a single quantum dot in a photonic crystal nanocavity," *Nature*, vol. 432, pp. 200–203, Nov. 2004.

[59] D. G. Lidzey, D. D. C. Bradley, A. Armitage, S. Walker, and M. S. Skolnick, "Photon-mediated hybridization of frenkel excitons in organic semiconductor microcavities," *Science*, vol. 288, pp. 1620–1623, June 2000.

[60] D. G. Lidzey, D. D. C. Bradley, T. Virgili, A. Armitage, M. S. Skolnick, and S. Walker, "Room temperature polariton emission from strongly coupled organic semiconductor microcavities," *Phys. Rev. Lett.*, vol. 82, pp. 3316–3319, Apr. 1999.

[61] Y. Zhu, D. Gauthier, S. Morin, Q. Wu, H. Carmichael, and T. Mossberg, "Vacuum rabi splitting as a feature of linear-dispersion theory: Analysis and experimental observations," *Phys. Rev. Lett.*, vol. 64, pp. 2499–2502, May 1990.

[62] D. E. Gómez, K. C. Vernon, P. Mulvaney, and T. J. Davis, "Surface plasmon mediated strong excitonphoton coupling in semiconductor nanocrystals," *Nano Lett.*, vol. 10, no. 1, pp. 274–278, 2009.

[63] T. K. Hakala, J. J. Toppari, A. Kuzyk, M. Pettersson, H. Tikkanen, H. Kunttu, and P. Trm, "Vacuum rabi splitting and strong-coupling dynamics for surface-plasmon polaritons and rhodamine 6g molecules," *Phys. Rev. Lett.*, vol. 103, p. 053602, July 2009.

[64] J. Dintinger, S. Klein, F. Bustos, W. Barnes, and T. Ebbesen, "Strong coupling between surface plasmon-polaritons and organic molecules in subwavelength hole arrays," *Phys. Rev. B*, vol. 71, p. 035424, Jan. 2005.

[65] Y. B. Zheng, B. K. Juluri, L. Lin Jensen, D. Ahmed, M. Lu, L. Jensen, and T. J. Huang, "Dynamic tuning of plasmonexciton coupling in arrays of nanodiskj-aggregate complexes," *Advanced Materials*, vol. 22, no. 32, pp. 3603–3607, 2010.

[66] G. A. Wurtz, P. R. Evans, W. Hendren, R. Atkinson, W. Dickson, R. J. Pollard, A. V. Zayats, W. Harrison, and C. Bower, "Molecular plasmonics with tunable excitonplasmon coupling strength in j-aggregate hybridized au nanorod assemblies," *Nano Lett.*, vol. 7, no. 5, pp. 1297–1303, 2007.

[67] C. Bonnand, J. Bellessa, and J. C. Plenet, "Properties of surface plasmons strongly coupled to excitons in an organic semiconductor near a metallic surface," *Phys. Rev. B*, vol. 73, p. 245330, June 2006.

[68] J. Bellessa, C. Bonnand, J. C. Plenet, and J. Mugnier, "Strong coupling between surface plasmons and excitons in an organic semiconductor," *Phys. Rev. Lett.*, vol. 93, p. 036404, July 2004.

[69] J. Vuckovic, M. Loncar, and A. Scherer, "Surface plasmon enhanced light-emitting diode," *IEEE Journal of Quantum Electronics*, vol. 36, pp. 1131–1144, Oct. 2000.

[70] T. Schwartz, J. A. Hutchison, C. Genet, and T. W. Ebbesen, "Reversible switching of ultrastrong light-molecule coupling," *Phys. Rev. Lett.*, vol. 106, p. 196405, May 2011.

[71] S. Balci, "Ultrastrong plasmonexciton coupling in metal nanoprisms with j-aggregates," *Opt. Lett.*, vol. 38, pp. 4498–4501, Nov. 2013.

[72] A. E. Schlather, N. Large, A. S. Urban, P. Nordlander, and N. J. Halas, "Near-field mediated plexcitonic coupling and giant rabi splitting in individual metallic dimers," *Nano Lett.*, vol. 13, no. 7, pp. 3281–3286, 2013.

[73] S. Balci, A. Kocabas, C. Kocabas, and A. Aydinli, "Localization of surface plasmon polaritons in hexagonal arrays of moir cavities," *Applied Physics Letters*, vol. 98, p. 031101, Jan. 2011.

[74] J. Braun, B. Gompf, G. Kobiela, and M. Dressel, "How holes can obscure the view: Suppressed transmission through an ultrathin metal film by a subwavelength hole array," *Phys. Rev. Lett.*, vol. 103, p. 203901, Nov. 2009.

[75] A. Ikehata, X. Li, T. Itoh, Y. Ozaki, and J.-H. Jiang, "High sensitive detection of near-infrared absorption by surface plasmon resonance," *Applied Physics Letters*, vol. 83, pp. 2232–2234, Sept. 2003.

[76] R. Adato, A. Artar, S. Erramilli, and H. Altug, "Engineered absorption enhancement and induced transparency in coupled molecular and plasmonic resonator systems," *Nano Lett.*, vol. 13, no. 6, pp. 2584–2591, 2013.

[77] J. Pendry and A. MacKinnon, "Calculation of photon dispersion relations," *Phys. Rev. Lett.*, vol. 69, pp. 2772–2775, Nov. 1992.

[78] S. Balci, A. Kocabas, C. Kocabas, and A. Aydinli, "Slowing surface plasmon polaritons on plasmonic coupled cavities by tuning grating grooves," *Applied Physics Letters*, vol. 97, no. 13, pp. –, 2010.

[79] E. E. Jelley, “Spectral absorption and fluorescence of dyes in the molecular state,” *Nature*, vol. 138, pp. 1009–1010, Dec. 1936.

[80] J.-S. G. Bouillard, W. Dickson, D. P. O’Connor, G. A. Wurtz, and A. V. Zayats, “Low-temperature plasmonics of metallic nanostructures,” *Nano Lett.*, vol. 12, no. 3, pp. 1561–1565, 2012.

[81] G. A. Wurtz, R. Pollard, W. Hendren, G. P. Wiederrecht, D. J. Gosztola, V. A. Podolskiy, and A. V. Zayats, “Designed ultrafast optical nonlinearity in a plasmonic nanorod metamaterial enhanced by nonlocality,” *Nat Nano*, vol. 6, pp. 107–111, Feb. 2011.

[82] M. Ren, B. Jia, J.-Y. Ou, E. Plum, J. Zhang, K. F. MacDonald, A. E. Nikolaenko, J. Xu, M. Gu, and N. I. Zheludev, “Nanostructured plasmonic medium for terahertz bandwidth all-optical switching,” *Adv. Mater.*, vol. 23, no. 46, pp. 5540–5544, 2011.

[83] W. L. Barnes, T. W. Preist, S. C. Kitson, J. R. Sambles, N. P. K. Cotter, and D. J. Nash, “Photonic gaps in the dispersion of surface plasmons on gratings,” *Phys. Rev. B*, vol. 51, pp. 11164–11167, Apr. 1995.

[84] I. Avrutsky, “Surface plasmons at nanoscale relief gratings between a metal and a dielectric medium with optical gain,” *Phys. Rev. B*, vol. 70, p. 155416, Oct. 2004.

[85] A. Kocabas, S. Seckin Senlik, and A. Aydinli, “Plasmonic band gap cavities on biharmonic gratings,” *Phys. Rev. B*, vol. 77, p. 195130, May 2008.

[86] A. Kocabas, S. S. Senlik, and A. Aydinli, “Slowing down surface plasmons on a moir surface,” *Phys. Rev. Lett.*, vol. 102, p. 063901, Feb. 2009.

[87] D. L. Mills, “Interaction of surface polaritons with periodic surface structures; rayleigh waves and gratings,” *Phys. Rev. B*, vol. 15, pp. 3097–3118, Mar. 1977.

[88] G. Granet and B. Guizal, “Efficient implementation of the coupled-wave method for metallic lamellar gratings in TM polarization,” *J. Opt. Soc. Am. A*, vol. 13, pp. 1019–1023, May 1996.

[89] J. Chandezon, M. T. Dupuis, G. Cornet, and D. Maystre, “Multicoated gratings: a differential formalism applicable in the entire optical region,” *J. Opt. Soc. Am.*, vol. 72, pp. 839–846, July 1982.

[90] A. Kocabas, G. Ertas, S. S. Senlik, and A. Aydinli, “Plasmonic band gap structures for surface-enhanced raman scattering,” *Opt. Express*, vol. 16, pp. 12469–12477, Aug. 2008.

[91] T. Okamoto, F. HDhili, and S. Kawata, “Towards plasmonic band gap laser,” *Applied Physics Letters*, vol. 85, no. 18, pp. 3968–3970, 2004.

[92] S. Kitson, W. Barnes, and J. Sambles, “Photoluminescence from dye molecules on silver gratings,” *Optics Communications*, vol. 122, pp. 147–154, Jan. 1996.

[93] C. Symonds, C. Bonnand, J. C. Plenet, A. Brhier, R. Parashkov, J. S. Lauret, E. Deleporte, and J. Bellessa, “Particularities of surface plasmonexciton strong coupling with large rabi splitting,” *New Journal of Physics*, vol. 10, no. 6, p. 065017, 2008.

[94] E. D. Palik, *Handbook of Optical Constants of Solids.* Boston: Academic Press, 1991.

[95] S. C. Kitson, W. L. Barnes, and J. R. Sambles, “Full photonic band gap for surface modes in the visible,” *Phys. Rev. Lett.*, vol. 77, pp. 2670–2673, Sept. 1996.

[96] R. Esteban, A. G. Borisov, P. Nordlander, and J. Aizpurua, “Bridging quantum and classical plasmonics with a quantum-corrected model,” *Nat Commun*, vol. 3, p. 825, May 2012.

[97] Y. Cao, Z. Wei, C. Wu, H. Li, H. Chen, and K. Cai, “Collimation effect inside complete bandgap of electromagnetic surface resonance states on a metal plate perforated with a triangular array of air holes,” *Opt. Express*, vol. 20, pp. 25520–25529, Nov. 2012.

[98] P. A. Kossyrev, A. Yin, S. G. Cloutier, D. A. Cardimona, D. Huang, P. M. Alsing, and J. M. Xu, "Electric field tuning of plasmonic response of nanodot array in liquid crystal matrix," *Nano Lett.*, vol. 5, pp. 1978–1981, Sept. 2005.

[99] J. P. Reithmaier, G. Sk, A. Lffler, C. Hofmann, S. Kuhn, S. Reitzenstein, L. V. Keldysh, V. D. Kulakovskii, T. L. Reinecke, and A. Forchel, "Strong coupling in a single quantum dotsemiconductor microcavity system," *Nature*, vol. 432, pp. 197–200, Nov. 2004.

[100] T. Bagci, A. Simonsen, S. Schmid, L. G. Villanueva, E. Zeuthen, J. Appel, J. M. Taylor, A. Sorensen, K. Usami, A. Schliesser, and E. S. Polzik, "Optical detection of radio waves through a nanomechanical transducer," *Nature*, vol. 507, pp. 81–85, Mar. 2014.

[101] A. Wallraff, D. I. Schuster, A. Blais, L. Frunzio, R.-S. Huang, J. Majer, S. Kumar, S. M. Girvin, and R. J. Schoelkopf, "Strong coupling of a single photon to a superconducting qubit using circuit quantum electrodynamics," *Nature*, vol. 431, pp. 162–167, Sept. 2004.

[102] A. Alú and N. Engheta, "Input impedance, nanocircuit loading, and radiation tuning of optical nanoantennas," *Phys. Rev. Lett.*, vol. 101, p. 043901, July 2008.

[103] A. Alú and N. Engheta, "Tuning the scattering response of optical nanoantennas with nanocircuit loads," *Nat Photon*, vol. 2, pp. 307–310, May 2008.

[104] Y. Cui, J. Zhou, V. A. Tamma, and W. Park, "Dynamic tuning and symmetry lowering of fano resonance in plasmonic nanostructure," *ACS Nano*, vol. 6, pp. 2385–2393, Feb. 2012.

[105] R. Dallapiccola, A. Gopinath, F. Stellacci, and L. Dal Negro, "Quasi-periodic distribution of plasmon modes in two-dimensional fibonacci arrays of metal nanoparticles," *Opt. Express*, vol. 16, pp. 5544–5555, Apr. 2008.

[106] A. Gopinath, S. V. Boriskina, N.-N. Feng, B. M. Reinhard, and L. D. Negro, "Photonic-plasmonic scattering resonances in deterministic aperiodic structures," *Nano Lett.*, vol. 8, no. 8, pp. 2423–2431, 2008.

[107] S. G. Romanov, A. V. Korovin, A. Regensburger, and U. Peschel, "Hybrid colloidal plasmonic-photonic crystals," *Adv. Mater.*, vol. 23, no. 22-23, pp. 2515–2533, 2011.

[108] P. Dawson, F. de Fornel, and J.-P. Goudonnet, "Imaging of surface plasmon propagation and edge interaction using a photon scanning tunneling microscope," *Phys. Rev. Lett.*, vol. 72, pp. 2927–2930, May 1994.

[109] J.-C. Weeber, A. Bouhelier, G. Colas des Francs, S. Massenot, J. Grandidier, L. Markey, and A. Dereux, "Surface-plasmon hopping along coupled coplanar cavities," *Phys. Rev. B*, vol. 76, p. 113405, Sept. 2007.

[110] D. W. Pohl, W. Denk, and M. Lanz, "Optical stethoscopy: Image recording with resolution /20," *Applied Physics Letters*, vol. 44, pp. 651–653, Apr. 1984.

[111] T. Klar, M. Perner, S. Grosse, G. von Plessen, W. Spirkl, and J. Feldmann, "Surface-plasmon resonances in single metallic nanoparticles," *Phys. Rev. Lett.*, vol. 80, pp. 4249–4252, May 1998.

[112] M. Hu, C. Novo, A. Funston, H. Wang, H. Staleva, S. Zou, P. Mulvaney, Y. Xia, and G. V. Hartland, "Dark-field microscopy studies of single metal nanoparticles: understanding the factors that influence the linewidth of the localized surface plasmon resonance," *J. Mater. Chem.*, vol. 18, pp. 1949–1960, Apr. 2008.

[113] L. Helden, E. Eremina, N. Riefler, C. Hertlein, C. Bechinger, Y. Eremin, and T. Wriedt, "Single-particle evanescent light scattering simulations for total internal reflection microscopy," *Appl. Opt.*, vol. 45, pp. 7299–7308, Oct. 2006.

[114] C. Sönnichsen, S. Geier, N. E. Hecker, G. v. Plessen, J. Feldmann, H. Ditlbacher, B. Lamprecht, J. R. Krenn, F. R. Aussenegg, V. Z.-H. Chan, J. P. Spatz, and M. Mller, "Spectroscopy of single metallic nanoparticles using total internal reflection microscopy," *Applied Physics Letters*, vol. 77, pp. 2949–2951, Nov. 2000.

[115] C. Snnichsen, T. Franzl, T. Wilk, G. von Plessen, J. Feldmann, O. Wilson, and P. Mulvaney, "Drastic reduction of plasmon damping in gold nanorods," *Phys. Rev. Lett.*, vol. 88, p. 077402, Jan. 2002.

[116] H. Ditlbacher, A. Hohenau, D. Wagner, U. Kreibig, M. Rogers, F. Hofer, F. Aussenegg, and J. Krenn, "Silver nanowires as surface plasmon resonators," *Phys. Rev. Lett.*, vol. 95, p. 257403, Dec. 2005.

[117] E. Cubukcu, E. A. Kort, K. B. Crozier, and F. Capasso, "Plasmonic laser antenna," *Applied Physics Letters*, vol. 89, p. 093120, Aug. 2006.

[118] Y. Gong and J. Vukovi, "Design of plasmon cavities for solid-state cavity quantum electrodynamics applications," *Applied Physics Letters*, vol. 90, p. 033113, Jan. 2007.

[119] M. Bayindir, B. Temelkuran, and E. Ozbay, "Tight-binding description of the coupled defect modes in three-dimensional photonic crystals," *Phys. Rev. Lett.*, vol. 84, pp. 2140–2143, Mar. 2000.

[120] S. Balci, M. Karabiyik, A. Kocabas, C. Kocabas, and A. Aydinli, "Coupled plasmonic cavities on moire surfaces," *Plasmonics*, vol. 5, pp. 429–436, Dec. 2010.

[121] I. Smolyaninov, D. Mazzoni, J. Mait, and C. Davis, "Experimental study of surface-plasmon scattering by individual surface defects," *Phys. Rev. B*, vol. 56, pp. 1601–1611, July 1997.

[122] F. Pincemin, A. Maradudin, A. Boardman, and J.-J. Greffet, "Scattering of a surface plasmon polariton by a surface defect," *Phys. Rev. B*, vol. 50, pp. 15261–15275, Nov. 1994.

[123] A. Goban, C.-L. Hung, S.-P. Yu, J. D. Hood, J. A. Muniz, J. H. Lee, M. J. Martin, A. C. McClung, K. S. Choi, D. E. Chang, O. Painter, and H. J. Kimble, "Atomlight interactions in photonic crystals," *Nat Commun*, vol. 5, May 2014.

[124] S. Mookherjea, J. S. Park, S.-H. Yang, and P. R. Bandaru, “Localization in silicon nanophotonic slow-light waveguides,” *Nat Photon*, vol. 2, pp. 90–93, Feb. 2008.

[125] L. V. Hau, S. E. Harris, Z. Dutton, and C. H. Behroozi, “Light speed reduction to 17 metres per second in an ultracold atomic gas,” *Nature*, vol. 397, pp. 594–598, Feb. 1999.

[126] M. D. Lukin and A. Imamoğlu, “Controlling photons using electromagnetically induced transparency,” *Nature*, vol. 413, pp. 273–276, Sept. 2001.

[127] Y. Okawachi, M. S. Bigelow, J. E. Sharping, Z. Zhu, A. Schweinsberg, D. J. Gauthier, R. W. Boyd, and A. L. Gaeta, “Tunable all-optical delays via brillouin slow light in an optical fiber,” *Phys. Rev. Lett.*, vol. 94, p. 153902, Apr. 2005.

[128] Y. Okawachi, M. Foster, J. Sharping, A. Gaeta, Q. Xu, and M. Lipson, “All-optical slow-light on a photonic chip,” *Opt. Express*, vol. 14, pp. 2317–2322, Mar. 2006.

[129] M. Sandtke and L. Kuipers, “Slow guided surface plasmons at telecom frequencies,” *Nat Photon*, vol. 1, pp. 573–576, Oct. 2007.

[130] S. Wedge, I. R. Hooper, I. Sage, and W. L. Barnes, “Light emission through a corrugated metal film:the role of cross-coupled surfaceplasmon polaritons,” *Phys. Rev. B*, vol. 69, p. 245418, June 2004.

[131] J.-C. Weeber, A. Bouhelier, G. Colas des Francs, L. Markey, and A. Dereux, “Submicrometer in-plane integrated surface plasmon cavities,” *Nano Lett.*, vol. 7, pp. 1352–1359, Apr. 2007.

[132] S. Derom, A. Bouhelier, A. Kumar, A. Leray, J.-C. Weeber, S. Buil, X. Quélin, J. P. Hermier, and G. C. d. Francs, “Single-molecule controlled emission in planar plasmonic cavities,” *Phys. Rev. B*, vol. 89, p. 035401, Jan. 2014.

[133] A. Yariv, Y. Xu, R. K. Lee, and A. Scherer, “Coupled-resonator optical waveguide: a proposal and analysis,” *Opt. Lett.*, vol. 24, pp. 711–713, June 1999.

[134] Y.-H. Chen, J. Li, M.-L. Ren, and Z.-Y. Li, “Amplified spontaneous emission of surface plasmon polaritons with unusual angle-dependent response,” *Small*, vol. 8, pp. 1355–1359, May 2012.

[135] J. Seidel, S. Grafström, and L. Eng, “Stimulated emission of surface plasmons at the interface between a silver film and an optically pumped dye solution,” *Phys. Rev. Lett.*, vol. 94, p. 177401, May 2005.

[136] N. I. Zheludev, S. L. Prosvirnin, N. Papasimakis, and V. A. Fedotov, “Lasing spaser,” *Nat Photon*, vol. 2, pp. 351–354, June 2008.

[137] W. Zhou, M. Dridi, J. Y. Suh, C. H. Kim, D. T. Co, M. R. Wasielewski, G. C. Schatz, and T. W. Odom, “Lasing action in strongly coupled plasmonic nanocavity arrays,” *Nat Nano*, vol. 8, pp. 506–511, July 2013.

[138] M. C. Gather, “A rocky road to plasmonic lasers,” *Nat Photon*, vol. 6, pp. 708–708, Nov. 2012.

[139] C. K. Carniglia, L. Mandel, and K. H. Drexhage, “Absorption and emission of evanescent photons,” *J. Opt. Soc. Am.*, vol. 62, pp. 479–486, Apr. 1972.

[140] F. H’Dhili, T. Okamoto, J. Simonen, and S. Kawata, “Improving the emission efficiency of periodic plasmonic structures for lasing applications,” *Optics Communications*, vol. 284, pp. 561–566, Jan. 2011.

[141] M. I. Stockman, “Nanoplasmonics: past, present, and glimpse into future,” *Opt. Express*, vol. 19, pp. 22029–22106, Oct. 2011.